Max-Planck-Institut für Metallforschung
Stuttgart

NANOSCALE ADHESION OF INDIVIDUAL GECKO SPATULAE EXPLORED BY ATOMIC FORCE MICROSCOPY

Gerrit Huber

Dissertation
an der
Universität Stuttgart

Bericht Nr. 183
Januar 2006

NANOSCALE ADHESION OF INDIVIDUAL GECKO SPATULAE EXPLORED BY ATOMIC FORCE MICROSCOPY

Von der Fakultät für Chemie der Universität Stuttgart
zur Erlangung der Würde eines Doktors der
Naturwissenschaften (Dr. rer. nat.) genehmigte Abhandlung

Vorgelegt von
Dipl.-Ing. Gerrit Huber
aus Saarbrücken

Hauptberichter:	Prof. Dr. phil. Eduard Arzt
Mitberichter:	Prof. Dr.-Ing. Frank Mücklich
Tag der mündlichen Prüfung:	23. Januar 2006

INSTITUT FÜR METALLKUNDE DER UNIVERSITÄT STUTTGART
und
MAX-PLANCK-INSTITUT FÜR METALLFORSCHUNG STUTTGART

Stuttgart, Januar 2006

Nil tam difficile est, quid quaerendo investigari non possit.

(Terenz, Heauton Timorumenos)

DANKSAGUNG

Diese Dissertation wurde von November 2002 bis November 2005 am Max-Planck-Institut für Metallforschung in Stuttgart angefertigt. Einige Ergebnisse der Arbeit wurden bereits in wissenschaftlichen Zeitschriften veröffentlicht. So wurden Teile des dritten Kapitels in *Biology Letters* 1, 2-4 (2005) publiziert. In den *Proceedings of the National Academy of Sciences of the USA* 102, 16293-16296 (2005) finden sich Ergebnisse des vierten Kapitels wieder. Ich möchte allen, die auf unterschiedlichste Weise zum Gelingen der Arbeit beitrugen, meinen herzlichen Dank aussprechen.

Zuallererst danke ich Herrn Prof. Arzt für die Möglichkeit in seiner großartigen Abteilung promovieren zu dürfen. Ich empfand die zahlreichen, mitunter durchaus sehr intensiven und manchmal auch emotionalen Diskussionen mit ihm durchweg als äußerst bereichernd und stimulierend.

Desweiteren gilt mein ganz besonderer Dank Dr. Stanislav Gorb und Prof. Ralph Spolenak, die mich während meiner Promotion auf wundervolle Weise betreut und begleitet haben. Ihre große Diskussions- und Hilfsbereitschaft verbunden mit wohltuender menschlicher Nähe waren mir eine beständige und starke Stütze.

Herrn Prof. Mücklich verdanke ich sehr frühzeitige wissenschaftliche Förderung und damit sozusagen die Grundsteinlegung für diese Dissertation, bei der er sich freundlicherweise für die Übernahme des Mitberichts bereit erklärte.

Außerdem ist es mir eine große Freude Hubert Mantz (insbesondre für seine Ellipsometrie-messung), Prof. Karin Jacobs, Prof. Klaus Mecke sowie Prof. Jacob Israelachvili für die zahlreichen Diskussionen und die Zusammenarbeit bei der Klärung der Frage über die Rolle der Kapillarkräfte zu danken. Diese Hilfe schlug sich insbesondere in Kapitel 4 nieder.

Die gemeinsame Realisierung verschiedener *in situ* Versuche verdanke ich meinem Kollegen Steffen Orso, der mit seiner geschickten Mikromanipulator Steuerung so manche Gecko Seta in „Zugzwang“ brachte. Außerdem danke ich Dr. Susan Enders, die es verstand diese Haare mit Hilfe ihres Nanoindenters gehörig unter Druck zu setzen. Die erkenntnisreichen Ergebnisse beider Torturen lassen sich in Kapitel 6 nachlesen.

Herrn Dr. Detlef Knebel und Christian Löbbe von der JPK instruments AG danke ich für den guten Support und ihre prompte Hilfe bei Soft- oder Hardwareproblemen insbesondere aber für das Programmieren des Java Skriptes.

Allen Kolleginnen und Kollegen am Institut und insbesondere der Abteilung Arzt möchte ich für fruchtbare Diskussionen und die besonders angenehme Arbeitsatmosphäre danken.

Einen besonderen Dank möchte ich an dieser Stelle auch an Frau Hess richten, die mit ihrem unermüdlichen Einsatz mir so manch bürokratisches Hindernis aus dem Weg räumte, bevor ich überhaupt eine Chance hatte darüber zu stolpern.

Bei Nicole, Astrid, Nato, Laura, Natascha und natürlich meinem Lieblingsbüronachbarn Guillaume möchte ich mich für ihre Freundschaft und Hilfe in herzlicher Verbundenheit bedanken. Unvergessen werden mir die aufmunternden Kaffeerunden in der Mittagspause bleiben, sowie die humorvolle, intensive Pflege deutsch-französischer Nachbarschaftsbeziehungen in 4N18. Insbesondere „Cordialement merci beaucoup“ für die nützlichen Anmerkungen bei der kritischen Durchsicht meiner Dissertation!

Herrn Dr. Heinz Paulus danke ich in freundschaftlicher Verbundenheit für seine hilfreichen Hinweise bezüglich der englischen Sprache.

Amicus certus in re incerta cernitur (Cicero, De Amicitia). Ich hoffe nicht allzu oft unsichere Situationen durchleben zu müssen, aber zwei sehr gute Freunde an meiner Seite wissen zu dürfen, ist für mich eine unerschöpfliche Quelle großer Freude und tiefen Vertrauens- Kai, Claus- ich bin sehr froh, dass es Euch gibt!

„**F**ür die Welt bist du irgendjemand. Für irgendjemanden bist du die Welt.” (Aristoteles) Liebe Eva - Du bist meine Welt!

„**O**n ne voit bien qu'avec le coeur. L'essentiel est invisible pour les yeux. ” (Antoine de Saint-Exupéry) Meiner Mutter Gisela und meinem Vater Hans-Georg möchte ich sehr danken, dass sie mich nicht nur diese Weisheit lehrten, sondern mir beständig und in reichstem Überfluss Mut, Kraft und Vertrauen schenkten, so wie es nur wundervolle Eltern können.

Index

Symbols and Abbreviations

Symbols:

a	Contact radius	[m]
α	Angle between force and loaded object	[°]
β	Proportionality factor	[]
c	Cantilever stiffness	[N/m]
c_s	Setal bending stiffness	[N/m]
c_c	Combined stiffness	[N/m]
d, D	Distance	[m]
δ	Penetration depth	[m]
e	Permittivity	[C/(Vm)]
E	Young's modulus	[Pa]
E_a	Adsorption energy	[J]
E_r	Reduced elastic modulus	[Pa]
E^*	Effective modulus	[Pa]
ε	Strain	[%]
f	Area or volume fraction	[]
F	Force	[N]
g	Geometrical factor	[]
h	Planck constant	[Js]
γ_L	Liquid/ vapor surface tension	[J/m^2] or [N/m]

γ	Thermodynamic work of adhesion	[J/m^2] or [N/m]
γ_i	Surface energy of substrate *i*	[J/m^2] or [N/m]
γ_{12}	Interfacial energy between surface *1* and *2*	[J/m^2] or [N/m]
h	Humidity	[%]
H	Hamaker constant	[J]
I	Moment of inertia	[m^4]
j	Lennard-Jones parameter	[m]
k_B	Boltzmann constant	[~1.38·10^{-23} J/K]
L	Length	[m]
n	Index of refraction	[]
N	Number	[]
v	Frequency	[1/s]
p	Pressure	[Pa]
P	Lennard-Jones Potential	[J] or [Nm]
q	Electric charge	[V]
r, R	Radius	[m]
R^*	Effective radius	[m]
ρ	Relative water coverage	[]
S	Sensitivity	[V/m]
σ	Stress	[Pa]
T	Temperature	[°C]
θ	Water droplet contact angle	[°]
u	Lennard-Jones parameter	[J] or [Nm]
v	Poisson ratio	[]
w	Band width	[m]

Abbreviations:

Atomic force microscopy/microscope	(AFM)
Derjaguin, Muller and Toporov	(DMT)
Digital pulsed force mode™	(DPFM)
Focused ion beam	(FIB)
Johnson, Kendall and Roberts	(JKR)
Micro-electromechanical system	(MEMS)
Position-sensitive detector	(PSD)
Root-mean-square	(RMS)
Scanning electron microscopy	(SEM)
Scanning probe microscopy	(SPM)
Scanning tunneling microscopy	(STM)
Transmission electron microscopy	(TEM)
Ultra high vacuum	(UHV)
Van der Waals	(vdW)

GERRIT HUBER:

NANOSCALE ADHESION OF INDIVIDUAL GECKO SPATULAE BY ATOMIC FORCE MICROSCOPY

Institute of Physical Metallurgy, University of Stuttgart and
Max Planck Institute for Metals Research, Stuttgart, 2005
132 pages, 37 figures, 2 tables

ABSTRACT: Attachment mechanisms of animals that can cling to walls and even walk on ceilings have drawn a significant amount of scientific and public attention. The gecko is one of the heaviest and best clinging animals and it has developed intricate hierarchical structures consisting of toes (millimeter dimensions), lamellae (400-600 µm size), setae (micron dimensions) and spatulae (~ 200 nm size). At first this work gives the reader a theoretical background of the techniques used and the underlying physical principles. By means of these techniques the adhesion force for individual spatulae on glass at ambient conditions could be measured and was found to be about 10 nN. This became only possible using the milling facility of a focused ion beam microscope for specimen preparation. The pull-off force was additionally measured as a function of various parameters (air humidity, surface chemistry and surface roughness) and it turned out that the gecko adhesion was remarkably influenced by the presence of water. The pull-off forces were proportional to the relative humidity varied inside an air tight container and increased with decreasing water droplet contact angle of the wafer used. The data obtained were modeled theoretically to explain the observed adhesion phenomena. Two physical theories were presented which are based on concepts of macrocapillarity and the effect of water monolayers on the van der Waals interaction. Both theories showed good agreement with the experimental data. The pull-off forces were also sensitive to the substrate topography. In cases where the surface roughness was in the critical range of the spatula size, presumably imprecise contact formation led to a distinct minimum of the measured adhesion values compared to smoother or rougher surfaces. Furthermore the mechanical properties of single setae could be determined for the first time. The hairs were mechanically tested by three methods: (a) *in situ* tensile tests using a focused ion beam microscope, (b) three-point bending tests using atomic force microscopy (AFM) and (c) nanoindentation. The results presented in this work shed new light on the nanomechanisms of gecko's attachment and will help in the rational design of artificial bio inspired attachment systems.

GERRIT HUBER:

NANOSCALE ADHESION OF INDIVIDUAL GECKO SPATULAE BY ATOMIC FORCE MICROSCOPY

Institut für Metallkunde, Universität Stuttgart und
Max-Planck-Institut für Metallforschung Stuttgart, 2005
132 Seiten, 37 Abbildungen, 2 Tabellen

KURZZUSAMMENFASSUNG: Das Haftvermögen von Tieren, welche an Wänden oder gar Decken laufen können, erzeugt ein beträchtliches öffentliches und wissenschaftliches Interesse. Von allen Tieren ist der Gecko das Schwerste und am besten Haftende, was durch komplexe, hierarchische Haarstrukturen auf der Unterseite seines Fußes ermöglicht wird. Der typische Geckofuß besteht aus Lamellen (400-600 µm lang), Setae (~6 µm breit und ~100 µm lang) und Spatulae (~200 nm breit und lang). Diese Arbeit gibt dem Leser zunächst den theoretischen Hintergrund der benutzten Experimentaltechniken samt der zu Grunde liegenden Physik mit auf den Weg. Mit Hilfe dieser Techniken konnten die Adhäsionskräfte einzelner Spatulae unter Laborbedingungen reproduzierbar zu 10 nN bestimmt werden. Hierfür unverzichtbar war die Probenpräparation mit Hilfe eines fokussierten Ionenstrahlmikroskops. Zusätzlich wurde die Ablösekraft als Funktion verschiedener Parameter (Humidität, Hydrophilitätsgrad und Oberflächenrauhigkeit) gemessen. Dabei stellte sich heraus, dass die Adhäsionskraft stark von der zur Verfügung stehenden Wassermenge abhing. So stiegen im Inneren eines luftdichten Behälters die Kraftwerte mit zunehmendem Humiditäts- und Hydrophilitätsgrad an. Die experimentell gewonnenen Daten wurden mit Hilfe zweier theoretischer Modelle erklärt. Beide Theorien zeigten gute Übereinstimmung mit den experimentellen Werten. Das erste Modell erklärte die Daten mit Hilfe einer Formel für makroskopische Kapillarkräfte, welche auf Nanometer große Wasserbrücken angewendet wurde. Das zweite Model berücksichtigte den Effekt von Wassermonolagenbedeckung auf die van der Waals Kräfte. Die Adhäsionskräfte einer einzelnen Spatula waren außerdem empfindlich gegenüber der Substratrauhigkeit. Sobald die Rauhigkeitswerte in den Bereich der Spatulagröße kamen, führte vermutlich eine unpräzise Kontaktausbildung zu einem distinkten Minimum der Adhäsionskraftwerte im Vergleich zu deutlich glatteren oder rauheren Oberflächen. Desweiteren konnten erstmals die mechanischen Eigenschaften einzelner Setae determiniert werden. Die Haare wurden mit Hilfe dreier unterschiedlicher Methoden untersucht: (a) *in situ* Zugversuche im fokussierten Ionenstrahlmikroskop, (b) Dreipunkt Biegeversuche mittels Raserkraftmikroskopie (eng. AFM) und (c) Nanoindentierungsversuche. Die hier präsentierten Ergebnisse ermöglichen neue Einblicke in die Gecko-Adhäsion auf der Nanoskala und werden bei der Entwicklung künstlicher, biologisch inspirierter Klebebänder helfen.

1 Introduction and Motivation

Biological structures quite often show a complex hierarchical organization[1, 2]. Biologists study various phenomena observable across a wide range of spatial scales: from molecules to cells to organisms, to populations, to communities, and to entire ecosystems. Living organisms span a size range exceeding more than twenty orders of magnitude in volume ($\sim 10^8$ in length), and populate environments that vary in scale by about 10^{25}. These circumstances provide both challenges and opportunities for the design and function of organisms. In this context the concept of hierarchical structure organization quite often stood the test in nature and might be illustrated most fascinatingly using the gecko adhesive toe as a focal point.

As can be gleaned in *De Historia Animalium* the astonishing climbing ability of geckos was already intriguing the Greek polymath Aristotle in the 4th century B.C.[3]. More than two millennia later, it became clear that animals which can cling to walls and walk on ceilings owe that ability to micron and sub-micron scale attachment elements. Thus the gecko, in particular, whose attachment system is the most elaborate so far discovered[4-7], is of great scientific interest. The hierarchical gecko foot structure (Figure 1.1 and more detailed in Figure 3.3) consists of lamellae, setae and spatulae. The mechanistic basis for gecko adhesion has been investigated already intensely before the beginning of this study[4-8] but the lowest hierarchical level, that of the spatula, had never been previously examined due to the experimental difficulty of accessing nanoscale dimensions.

Roughly one billion of these tiny foot-hairs allow the gecko to adhere to both rough and atomically smooth surfaces. In general adhesion has its origin in intermolecular and surface forces[9], which act universally between any two surfaces brought into sufficiently close contact.

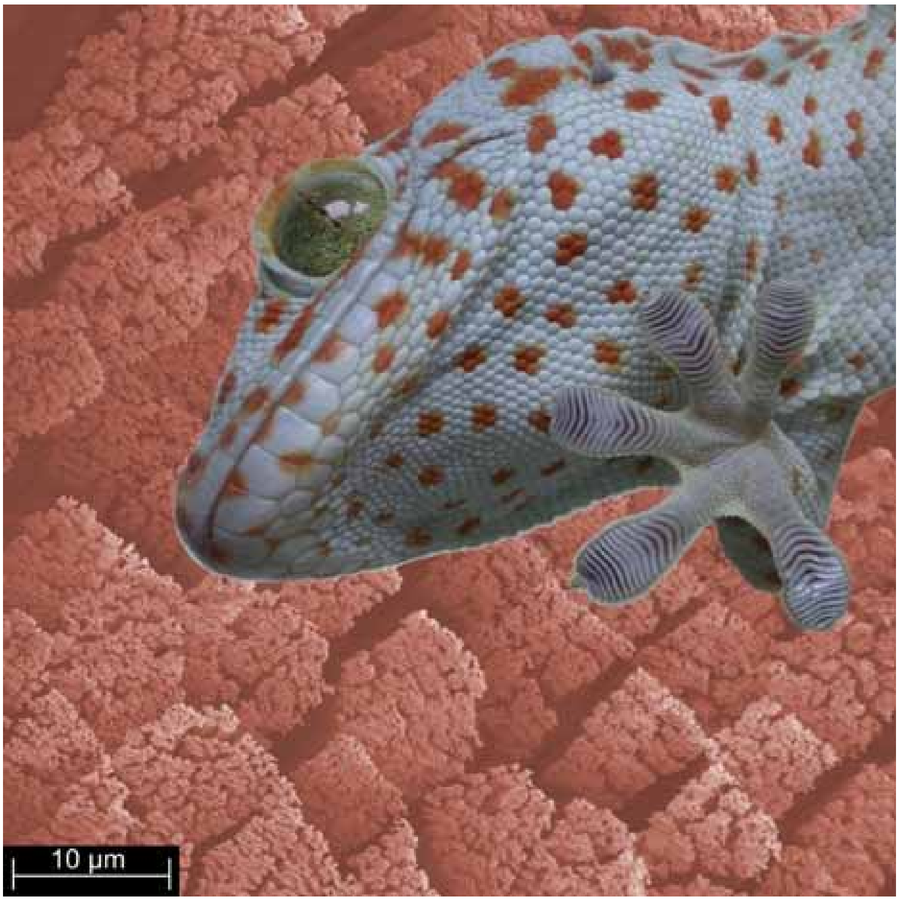

Figure 1.1 The lizard *Gekko gecko* with one foot adhering to a glass plate (foreground) and setal structures of its attachment organs (background).

Adhesion is paradoxical: our daily experience teaches us that ordinary objects do not stick together easily; our hands and feet do not stick to the wall, the pen does not adhere noticeably on the notepaper and even the structural design of the oldest cathedrals was based on the assumption that stones do not stick together but are simply held in place by gravity[10]. Yet it is obvious that the tiny components of the notepaper, i.e. the mechanical wood pulp and ultimately the atoms and molecules, stick together extremely well. Otherwise the notepaper would come to anything and could not be written on. At least in the microscopical world almost everything sticks well[11]. Something nevertheless hinders this universal adhesion in our macroscopical world. A first hint is that clean surfaces in good vacuum adhere much better than the same surfaces under typical environmental conditions making them dirty or oxygen covered. Almost any surface contamination reduces the adhesion. Secondly macroscopical bodies apparently in contact for the human eye are in fact not truly “touching” over the whole nominal contact area due to their surface roughness[12]. For instance, a surface roughness of just a few nanometers is already enough to remove the adhesion between clean and (elastically) stiff solid surfaces[13]. Thus only a small area fraction of the bodies is in intimate contact and therefore close enough for molecular interactions. In addition, the bodies will be elastically deformed near those contacts, and the stored elastic energy is returned during pull-off, thus helping to break the adhesive bond between the solids[14]. In summary the adhesion paradox can be explained by these two important aspects of molecular contact formation: contamination and roughness.

Today’s joining techniques like welding or adhesive bonding also have to deal with these two main problems. On the one hand due to the high requirements on cleanliness the industrial processes are cost-intensive and in addition, once joined, the two parts cannot be separated - for repairs or for possible recycling - without loss of material. On the other hand the adhesives have to deal with all kinds of surface roughness. Therefore typical hook and loop fasteners must be able to wet almost any surface but in turn gradually become dirty and fuzzed. It is reasonable that biomimicry of biological attachment structures offers strong technological advances. Dry adhesive systems potentially permit reversible, firm joints between materials without the need for welding or gluing. Possible applications range from climbing robots and industrial pick and place applications to a substitute for sticky tape that can be used repeatedly.

In this context it is instructive to take a closer look at nature’s solutions by investigating e.g. the attachment system of the gecko. On the one hand evolution had to find ways to ensure (a) that those tiny hairs could come into molecular contact with all kinds of rough surfaces and on the other hand to avoid (b) the contamination of the spatulae[15]. The solution to that problem was the (a) hierarchical and (b) contamination-resisting gecko foot structure as described in detail in chapter 3.1. After the foresaid it is clear that one has to approach the lowest hierarchical level of gecko's attachment system to explore the intermolecular basis of its adhesion. Although to date intensive studies on the gecko foot structure have been carried out[4-8, 16, 17] nothing is known about the mechanical properties of a single seta. Especially there has been an ongoing debate about the range and nature of the spatular pull-off force which has been impossible to access experimentally.

Thus the aim of this work was to find out the mechanical properties of single setae and to investigate the adhesive properties and the underlying physical principles on the level of a single spatula. After the literature review (chapter 2) the method of choice for most of the presented experiments, the atomic force microscopy (AFM) is described in detail. With this theoretical *armamentarium* we were able to access the smallest hierarchical level experimentally and to resolve the nanoscale adhesion of individual gecko spatulae (chapter 3). The second task was to find out more about the physical nature of the measured adhesion forces and as a result evidence for capillarity contributions to gecko adhesion will be given in chapter 4. The ideal wafer surfaces used in those experiments had little in common with real earthly topographies. Therefore chapter 5 details the influence of surface roughness on gecko adhesion. To get a deeper understanding of the spatular adhesion it also became necessary to measure the mechanical properties of its materials basis, i.e. the single gecko seta. Three different approaches were successfully undertaken (nanoindentation, *in situ* tensile tests and three-point bending studies by focused ion beam and atomic force microscopy), which are described in chapter 6. Finally chapter 7 gives an overall summary.

2 Literature Review

Atomic force microscopy is a specific member of the family of scanning probe microscopy (SPM). In 1981 the first member of that family, the scanning tunneling microscopy (STM) was developed. Binnig and Rohrer provided the first real-space determination of a Si (111) surface using STM[18]. They brought a sharp tip so close to the Si substrate that a tunneling current started to flow by applying a voltage between tip and surface. That current could be used to display the surface topography due to its extreme sensitivity to tip-sample separation. One disadvantage of STM was the limited use to (semi-) conductive materials since it is based on the presence of the tunneling current. The invention of the atomic force microscope (AFM) in 1985 sought to overcome this limitation[19]. Having solved one of the most intriguing problems in surface science, the rapid propagation and continued success of SPM in labs around the world led to the award of the Nobel Prize in Physics to Binnig and Rohrer in 1986.

The ability of AFM to create three-dimensional micrographs with resolution down to the nanometer and Angstrom scales has made it an essential tool for imaging and characterizing surfaces in various applications. The instruments can be used in any environment besides ambient air, such as various gases[20], liquids[21, 22], vacuum[18, 23, 24], at low (lower than 100 K)[25] and high temperatures[26]. The applications range from routine surface roughness analysis and measuring the nanomechanical properties of technical materials[27] to probing biomolecules including living cells[28-32] as well as to experiments with other biological materials[22, 33-35] or single molecule experiments[36]. Especially the study of live biological samples requires humid or wet environment and benefits from AFM operating under physiological conditions[28]. One disadvantage of SPM is the scan speed limitation[37]. It typically takes about 5 minutes to image a complete area (e.g. 5 µm x 5 µm) and many applications (e.g. *in situ* experiments) would benefit from faster imaging at the nanoscale.

2.1 AFM working principle

An extremely sharp pyramidal tip, several microns in length with a typical tip radius of about 10 nm, at the free end of a reflective cantilever (~200 µm long) is brought into close proximity of the sample surface by a very low force which is of the order of magnitude typical of intermolecular forces (Figure 2.1).

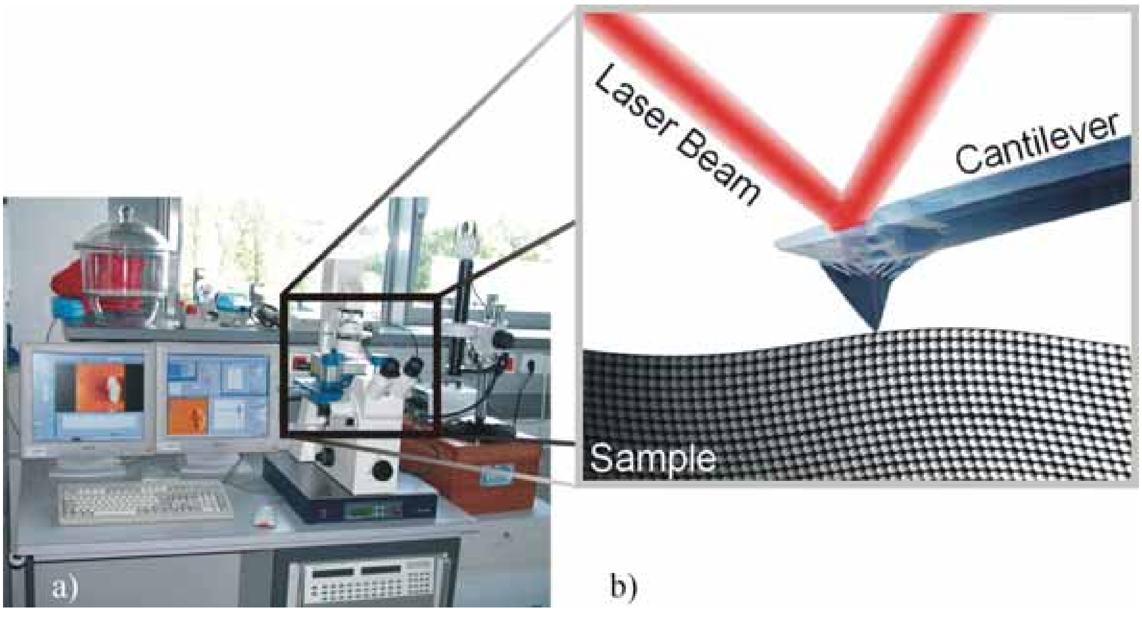

Figure 2.1 a) Experimental setup in the laboratory. b) A sharp pyramidal tip at the free end of a reflective cantilever is brought into close proximity of the sample surface. The laser beam is focused opposite to the tip on the rear side of the beam

A piezo-electric tube scanner provides the movement of the cantilever, which is detected by a laser deflection technique. The laser beam is focused on the rear side of the cantilever as closely as possible opposite to the tip and its reflection is received by a position-sensitive detector (PSD). The cantilever is tilted downward by about 10° with respect to the horizontal plane ensuring that after successful approach only the tip contacts the surface. The measured differential PSD voltage provides the AFM signal, which is a very sensitive measure of the vertical and lateral cantilever deflections. Micro- and nanotechnology increasingly require not only topographical information of the sample but also their material properties. To clarify the basics of AFM force measurements, Figure 2.2 shows a typical force-versus-distance curve together with the corresponding cantilever deflections.

At the initial state (1.) the tip-to-sample distance is high thus the force acting on the cantilever beam is zero. As the cantilever gradually moves closer to the surface, weak forces increasingly attract the tip until finally at very small separation distances the cantilever suddenly jumps into contact (2.) and reaches a new equilibrium. Attractive (e.g. van der Waals and capillary forces) and repulsive (e.g. Pauli repulsion) forces are now acting equally strongly on the probe tip. At this moment the distance between tip and surface atoms is comparable with a typical chemical bond length (several angstroms). Pushing the cantilever further towards the hard sample surface results in an increasing repulsive force because more and more atoms are coming so close together that their electron clouds begin to repel each other electrostatically. These strong forces cause the cantilever to bend rather than forcing the tip closer towards the sample. According to Hooke’s law the slope in this repulsive force regime is proportional to the cantilever spring constant c, which is required together with the instruments sensitivity S to quantify forces by AFM. S is the proportionality factor between the detected change in voltage and the measured change in deflection. In this manner the instrument can be calibrated. At a set point value the cantilever turns (3.) and starts to retract from the surface. The tip remains in contact with the surface due to adhesion forces causing the cantilever to bend downwards (4.). Eventually the piezo-electric tube scanner overcomes the maximum adhesive force, the probe tip breaks free and the cantilever returns to its initial state (1.).

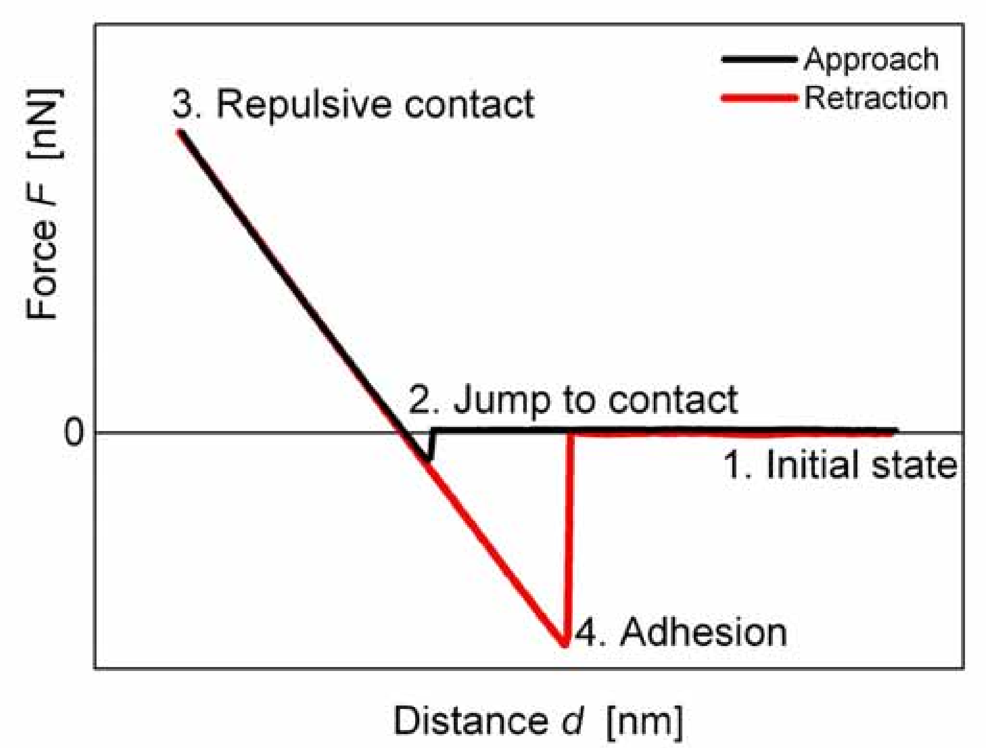

a)

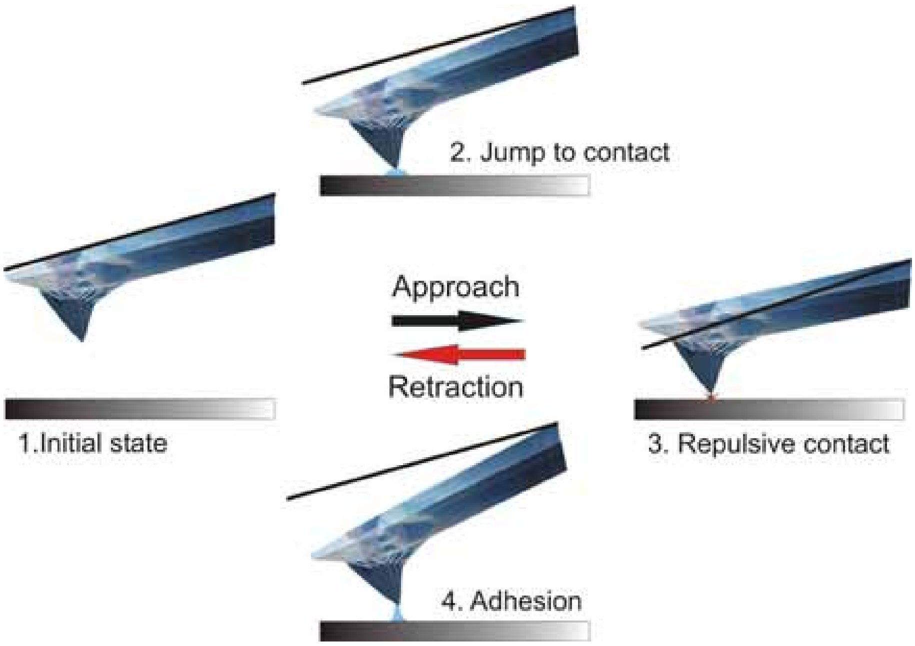

b)

Figure 2.2 a) Original force versus distance curve as observed by AFM and b) the corresponding cantilever deflections during approach and retraction.

It is worth knowing that adhesion is a dissipative and therefore irreversible process. Forces acting during the cantilever-to-sample approach differ from the forces during the probe retraction (Figure 2.2). The work of adhesion that has to be exerted in order to separate the two surfaces is lost as heat to the environment, giving rise to a hysteretic force-distance behavior.

Reasons for this hysteresis are manifold: A larger hysteresis is detected if one switches from ultra high vacuum to ambient conditions due to the presence of water and organics (which enable molecular entanglement). Additionally all cantilever instabilities (low cantilever stiffness, jumping events due to nonlinear forces) as well as friction forces, and high temperatures contribute to the dissipative process. A detailed review giving a deeper theoretical background and presenting the great variety of AFM force-distance curves has been written by Cappella and Dietler[38]. A guide for the interpretation of force curves in force microscopy has been published by Burnham *et al.*[39].

2.2 Operation modes

In atomic force microscopy there are several operation modes to image and characterize a specimen. All of them are based on the same working principle: A sharp tip scans over the surface of interest and the final (topography, adhesion or stiffness) map is composed of point-by-point measurements of the interaction between tip and sample. In the following four operation modes are described: the contact, non-contact, intermittent-contact and the digital pulsed force mode™. The different modes operate in distinct force regimes, which can be associated with specific ranges of the Lennard-Jones potential. The potential is only dependent on the distance *d* between the molecules or atoms and is described as:

$$P(d) = 4u\left[\left(\frac{j}{d}\right)^{12} - \left(\frac{j}{d}\right)^{6}\right] \qquad [2.1]$$

where *u* and *j* are the empirical Lennard-Jones parameters and have the units [J] and [m] respectively. A schematic of the potential as a function of the distance *d* with the corresponding operation mode regimes is shown in Figure 2.3.

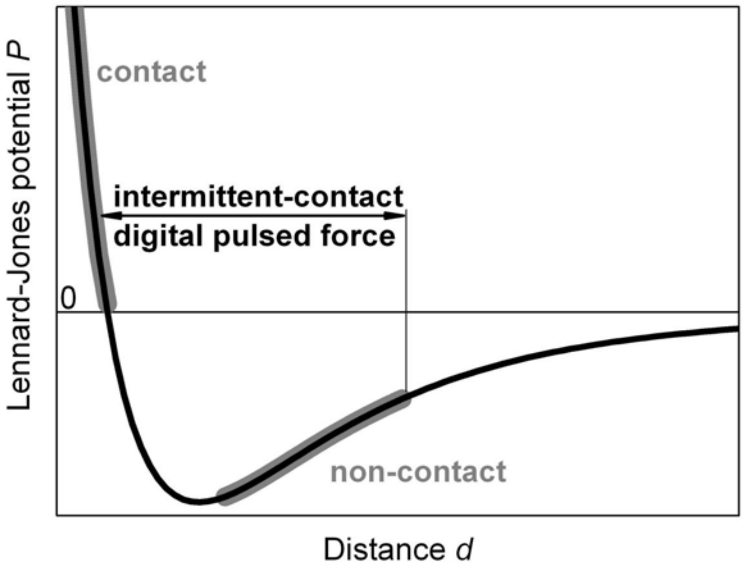

Figure 2.3 Lennard-Jones potential *P* as a function of the distance *d*. The corresponding AFM operation mode regimes are indicated along the curve.

The Lennard-Jones force is the negative derivative of the potential. It is mildly attractive as two uncharged molecules or atoms approach each another from a distance, but strongly repulsive when they get too close.

2.2.1 Contact mode

The most common imaging technique needs a detection and feedback system that measures the cantilever response and re-adjusts its position. Features on the sample surface cause the cantilever to deflect in vertical and lateral directions. The AFM system (NanoWizard®, JPK instruments AG, Berlin, Germany) applied in the present study uses a hardware linearization in all three axes also for closed loop measurements.

It continuously adjusts the position of the cantilever above the surface during the scanning procedure. For the vertical deflection a set point has to be selected (which is proportional to the force pushing the cantilever on the surface) and the feedback system adjusts the height of the cantilever base to keep the vertical deflection constant as the tip moves over the surface. This re-adjustment provides the signal of the topography. The contact forces are typically in the nN range. Each change in the deflection is detected by the PSD and gives rise to a vertical movement of the piezo-electric tube scanner to compensate this variation. The contact force causes the cantilever to bend while accommodating the respective topography and has the potential to damage the surface and/or the tip. Especially if the tip is dragged across soft materials such as polymers or biological materials, this circumstance becomes important. The fact that contact-mode AFM is a static measurement makes it prone to drift and can lead to a low signal-to-noise ratio. On the one hand low stiffness cantilevers can be used to increase the signal but on the other hand they are too weak to resist strong attractive forces resulting in the so called “snap-in” instability close to the surface[38]. Thus imaging can only be operated in true physical contact including the problem of sample damage. This limitation had been overcome by the development of the non-contact mode.

2.2.2 Non-contact mode

The non-contact mode[40, 41] uses a frequency modulation technique where the cantilever oscillates at high amplitudes (up to 150 nm) and senses the force gradient between tip and sample. The total force (in the range of pN) between tip and sample is much smaller compared to the contact mode and provides the desired protection of soft or elastic samples with improved signal-to-noise. However, in this mode it is impossible to measure the mechanical properties quantitatively. Capillary forces make it particularly difficult to control the scanning in ambient conditions because the tip can jump spontaneously into contact and damage the soft surface. Therefore atomically-resolved non-contact mode images are only obtainable under ultra high vacuum (UHV) conditions. Another solution to this problem is to work in liquids as long as damping effects are taken into account.

2.2.3 Intermittent-contact mode

The intermittent-contact mode (also known as tapping mode®) is a technique used for studying soft and compliant samples that are susceptible to damage[42]. A large cantilever spring constant c of ~40 N/m is needed to avoid the spontaneous snap-in instability. The modulated amplitude (as opposed to the frequency modulation technique used by non-contact mode AFM) is kept large enough so that the tip does not get stuck to the sample. The cantilever oscillation is driven with a frequency close to its resonance (typically in the range of 100 kHz - 400 kHz) leading to an intermittent repulsive contact with the sample surface (Figure 2.3).

As the cantilever begins to cyclically contact the surface, the oscillation amplitude is reduced due to dissipated energy[43] during contact formation. This loss is taken as a measure of the surface topography. The feedback loop maintains the amplitude oscillation while the tapping tip is scanned across the sample. During that dynamical process the detection sensitivity is very high and has the potential to provide sub-angstrom vertical resolution. By avoiding continuous contact formation during the scan, lateral forces are remarkably reduced thereby minimizing both tip-sample degradation and contamination. Additionally intermittent-contact mode can also provides a phase image by simultaneously monitoring the phase lag of the cantilever oscillation relative to the signal sent to the cantilever's piezo driver. By mapping the phase shift during the scan, qualitative variations in friction and viscoelasticity can be detected. Since the cantilever is moving in a non-linear force field and dissipates energy due to interactions with the surface[43], there is currently no simple quantitative correlation between phase contrast and the property of the surface. The potential to image heterogeneous samples with topographical and compositional contrast spurred many fundamental studies on the dynamics of the tip-surface interaction. A comprehensive review of these studies was published in 2002 by García and Pérez[44].

It must be pointed out that in ambient conditions most rigid surfaces are covered by a few monolayers of water (chapter 4) and it looks quite different if one compares contact and intermittent-contact mode images of identical surfaces. The atomic force microscope operating in contact mode penetrates the liquid and images the “real” surface beneath whereas the AFM working in intermittent-contact mode additionally images the water layer covering the surface. Thus it is noticeable that on the one hand map and information of the operation mode used should be provided together and on the other hand a comparison of two surfaces should be carried out only if the same imaging mode had been used.

2.2.4 The Digital Pulsed Force Mode™

The Digital Pulsed Force Mode™ (DPFM) is a non-resonant, intermediate-contact mode for AFM[45]. Thus due to minimized lateral forces it also avoids surface damage. The main difference compared to the intermittent-contact mode is the use of a lower spring constant (~3 N/m) and the point-by-point measurement of complete force-distance curves. By means of DPFM it is possible to access simultaneously any information contained in topographical imaging and force-distance curves for every pixel of the map. Compared to the time-consuming mapping of the interaction forces by AFM in the past[46] this method is a substantial progress. Mapping can be performed at normal scan rates (e.g. 1 Hz), because the high speed data-acquisition system is able to work continuously at 10 MB/s. Properties such as viscosity, energy dissipation, contact-time and long range forces can be analyzed and mapped along with topography. A modulation generator introduces a sinusoidal signal to the piezo electric scanner with tunable amplitude (10 nm - 500 nm) and frequency (0.1 kHz - 2 kHz). Basically a complete force-distance cycle is carried out at every pixel of the final image.

Figure 2.4 shows a typical DPFM force *vs.* time signal. For the analysis first the baseline has to be determined. All other parameters are related to their position, which may vary from pixel to pixel due to long-range electrostatic forces. During approaching the tip suddenly snaps into contact (Figure 2.2). Subsequently the tip is pushed further against the sample. In an analogous manner the slope of the increasingly repulsive force is related to the local stiffness. The stiffer the investigated specimen the larger is the slope. Its value is recorded and represented in a stiffness map. Next the force signal reaches the maximal (positive) force F_{max}, which is used as the feedback signal for the AFM control circuits and therefore determines the topographical image. As the tip is retracted, the force signal changes sign (from positive, repulsive to negative, attractive forces). In the end, the tip detaches and a distinctive force minimum is observed. Its value is recorded and fed into an additional analogue AFM input channel leading to the desired adhesion map. The subsequent free cantilever oscillation is damped towards the baseline and the whole cycle can start again.

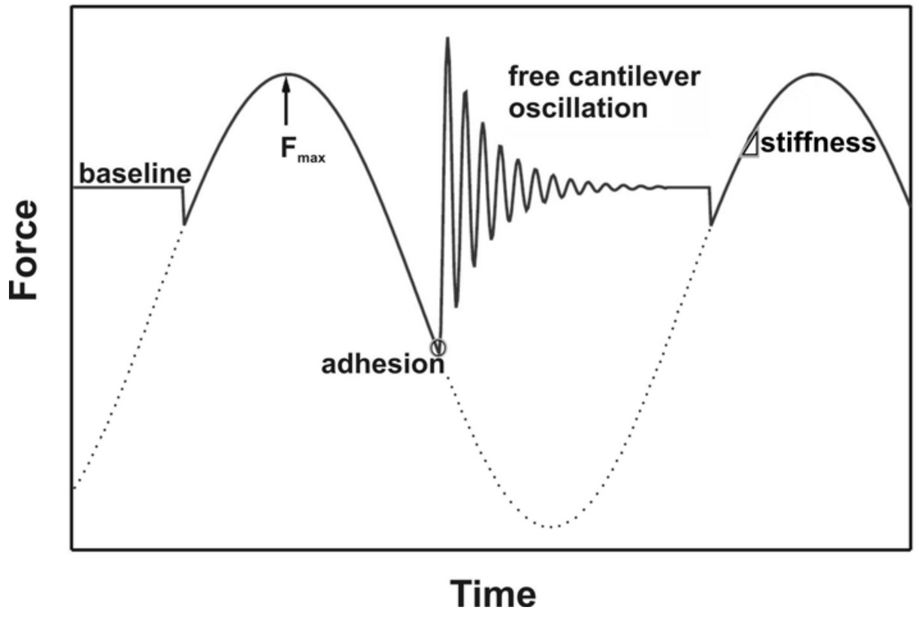

Figure 2.4 Schematic showing the modulation voltage (dotted line) and the force signal (solid line) for a complete modulation period.

Results of the usage of DPFM will be presented in chapter 6. The intermittent-contact mode was used in this work for imaging of the setae and spatulae (Figure 3.2) whereas contact mode was always used where in addition to the surface topography locally force-distance curves had to be determined.

2.3 Tip-surface interactions

The study of tip-surface interactions is an important link between the macroscopical and nanoscopical worlds. Giving full details of the intermolecular and surface forces is beyond the scope of this work but the interested reader can find out more by reading Israelachvili[9] and Burnham[47]. Because of the breadth and depth of this subject just three classes of surface forces will be presented in the following sections due to their immediate importance to the investigations presented here: electrostatic, electrodynamic and capillary forces.

2.3.1 Electrostatic forces

Electrostatic forces include those due to charges, image charges and dipoles. Since the time of the ancient Greeks it has been known that amber rubbed with fur would become "electrified" and attract small objects. The weakness of electrostatic forces between different everyday objects reflects the fact that matter consists of almost exactly equal numbers of positively charged protons and negatively charged electrons. In 1785 it was Charles A. Coulomb, who first quantitatively measured the electrical attraction and repulsion between charged objects. He formulated that the electrostatic force F_{el} is proportional to the product of the object charges (q_i) and inversely proportional to the square of the distance d between them:

$$F_{el} \propto \frac{q_1 q_2}{d^2} \qquad [2.2]$$

If, as an illustration, one sets $q_1 = q_2 = 1.6 \times 10^{-19}$ C, the charge of one electron, and solve for the force when the two electrons are an atomic distance d = 0.2 nm apart, one finds that the resulting force is about 6 nN. This is a magnitude that can be detected with all AFMs. However the forces can be attractive or repulsive depending on whether like or unlike charges are closer together. Only for an induced dipole or a freely rotating permanent dipole in vacuum or air is the interaction energy with a charge always attractive. On average, dipoles in a liquid orient themselves to form attractive interactions with their neighbors, but thermal motion can create some instantaneous configurations that are, in fact, repulsive. In general strong repulsive forces are referred to as exchange, hard-core, steric, or Born repulsion.

2.3.2 Electrodynamic forces

The short ranged van der Waals (vdW) forces play a central role in all phenomena involving intermolecular forces, for while they are not as strong as Coulomb or H-bonding interactions, they occur between *all* atoms and molecules and thus *a priori* between *all* macroscopic bodies. Considering oscillating electrons it becomes clear that there is not just one vdW force but rather there are three forces: namely the London (fluctuation), Keesom (orientation) and Debye (induction) forces. With the exception of highly polar materials such as water, London dispersion interactions give the largest contribution to the vdW attraction. A typical strength for “vdW bonds” is in the range of 0.01 to 0.1 eV per atom and the potential depends on the intermolecular distance as d^{-6}. A third medium in which the two opposite surfaces are immersed strongly affects the force magnitude[9, 48]. However, the van der Waals force between any two materials in vacuum is always attractive; the force between two identical materials is always attractive, too, but the force between two different materials in a liquid medium can be repulsive.

Dispersion interactions are to a first approximation additive, and their contributions to the interaction energy between two macroscopic bodies across vacuum can be found by adding up the pair-wise interactions as described in 1937 by Hamaker[49]. Today the interaction energy is generally described in terms of the Hamaker constant H. It reflects the strength of the vdW interaction for two bodies 1 and 2 in a medium 3 at a temperature T, with permittivities e_i and indexes of refraction n_i. The first term includes Keesom and Debeye interactions, the second the London interaction:

$$H = \frac{3}{4} k_B T \left(\frac{e_1 - e_3}{e_1 + e_3} \right) \left(\frac{e_2 - e_3}{e_2 + e_3} \right) + \frac{3h\nu}{8\sqrt{2}} \frac{(n_1^2 - n_3^2)(n_2^2 - n_3^2)}{\sqrt{n_1^2 + n_3^2}\sqrt{n_2^2 + n_3^2}[\sqrt{n_1^2 + n_3^2} + \sqrt{n_2^2 + n_3^2}]} \qquad [2.3]$$

where k_B is Boltzmann’s constant, h is Planck’s constant and v is the frequency of the electrons that orbit the nuclei. Typical values for H are about 10^{-20} - 10^{-19} J for interactions across vacuum (higher values are found for metals). Hamaker constants for interactions in a medium are an order of magnitude lower than in vacuum. Because of its high permittivity (~80), in water for instance, H is drastically reduced leading to almost no attractive or even repulsive forces.

Assuming an atomic distance $d = 0.2$ nm and using Derjaguin's equation[50] the vdW force in air between a spherical AFM tip (radius $R = 10$ nm) and a flat surface ($H = 10^{-19}$ J) can be approximately calculated as:

$$F_{vdW} = \frac{HR}{6d^2} \approx 4\ \text{nN} \qquad [2.4]$$

2.3.3 Capillary forces

The capillary force arises from the Laplace pressure of curved menisci formed by condensation of a liquid between and around two adhering surfaces. In the context of AFM measurements this means that at the moment when the tip contacts the liquid covered surface, the aquatic film reshapes to a bridge between AFM tip and surface (Figure 2.5).

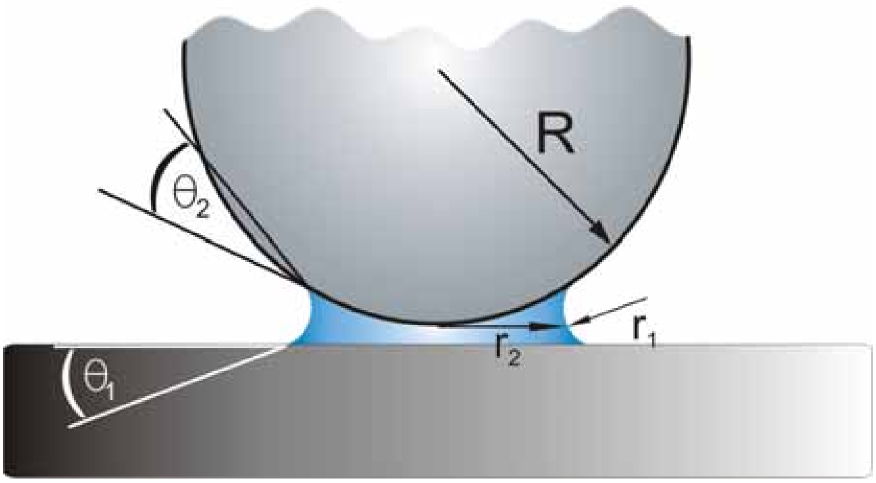

Figure 2.5 A capillary bridge (outer and inner radius r_1 and r_2 respectively) between a spherical tip (radius R, water droplet contact angle θ_2) and a flat surface (water droplet contact angle θ_1).

The liquid wets the AFM tip if the water-cantilever contact is energetically advantageous as compared to the water-air contact. It is intuitively clear but also thermodynamically favorable that the neck-curved bridge tends to flatten. This can only be achieved by pulling down the cantilever meaning that an attractive force acts on the AFM tip. The amount of this force can be derived from Laplace's equation. According to Pierre Simon de Laplace the pressure inside a liquid is modified over the atmospheric pressure by:

$$\Delta p = \frac{F}{\pi r_2^2} = \gamma_L \left(\frac{1}{r_1} + \frac{1}{r_2}\right) \qquad [2.5]$$

where γ_L is the liquid/vapor surface tension, r_2 and r_1 are the principal radii of surface curvature (Figure 2.5). Radii are taken as positive for convex curvatures and negative for concave curvatures. The capillary force between a sphere (radius R, water droplet contact angle θ_2) and a flat surface (water droplet contact angle θ_1) can be derived using simple geometrical correlations[9, 51]:

$$F_{cap} = 2\pi R \gamma_L \cdot (\cos\theta_1 + \cos\theta_2) \overset{(\theta_1=\theta_2)}{=} 4\pi R \gamma_L \cdot \cos\theta \qquad [2.6]$$

Assuming the AFM tip radius R to be 10 nm, using the liquid/vapor surface tension γ_L at 20 °C equal to 72.5 mJ/m^2 for water/air, one gets the following estimate for small θ: $F_{cap} \approx 10$ nN. Thus, in AFM the capillary force is of the same order of magnitude as the van der Waals interaction (Eq. [2.4]).

Moreover, even if the sample surface is hydrophobic, capillary attraction acts if the sum of both contact angles (on the cantilever θ_2 and on the sample θ_1) is less than 180°. This can easily be verified using the following trigonometrical correlation: $\cos\theta_1 + \cos\theta_2 = 2\cos([\theta_1+\theta_2]/2)\cos([\theta_1-\theta_2]/2)$. Additionally the capillary force might increase with time because in the case of surfaces covered with surfactant or polymer molecules (amphiphilic surfaces), it was observed[52, 53] that these molecules can change their conformation on exposure to humid air, so that non-polar groups are replaced by polar groups, which renders the formerly hydrophobic surfaces hydrophilic. This effect was also found with lipid and protein surfaces[54], which is an interesting result in the context of biological materials. When two surfaces of that type come into contact, water will condense around such preferred nucleation spots (chapter 4) and the adhesion force will be affected - generally increasing well above the value expected for inert hydrophobic surfaces[52-54]. In general for high resolution AFM imaging the influence of capillary forces must be minimized. Adjusting ambient conditions such as working under dry nitrogen, in vacuum, or in liquids often eliminates capillarity effects and remarkably improves resolution. Interpretation of experimental AFM data in terms of intermolecular and surface forces is often difficult because too many atoms are involved. For example, considering vdW forces it is basically possible to determine *a priori* the attraction force between tip and sample. The force would be equal to the sum of all pair wise interactions between cantilever molecules and the studied surface. However neither the exact molecule positions nor their correct number is known, which makes a single molecule analysis quite challenging[55]. In such cases continuum mechanical models are useful. Calculating the forces acting within the area of atomic contact between surfaces, it is important to keep in mind that continuum contact mechanics start to break down as the contact radius approaches atomic dimensions[56].

2.4 Contact mechanics

While *solid mechanics* deals usually with bulk material properties *contact mechanics* deals with properties in the vicinity of body contacts. In the context of AFM, both, tip and specimen are regarded as macroscopical bodies whose physical characteristics are described by parameters as Young's modulus or surface energy. In contact mechanics the measured forces are explained in terms of these accessible properties. If a large cantilever tip contacts a sample surface, forces start to act giving rise to elastic deformations of both sample and tip. This can affect the acquired image or force measurements. To properly interpret the measured data and to choose the appropriate operation mode it is necessary to apply the principles of contact mechanics[57, 58]:

2.4.1 The Hertz model

The solutions Heinrich Hertz published in 1882 allow to find the contact radius and penetration depth as a function of the applied load[59]. He considered two spheres (radii R_1 and R_2) compressed by a force F resulting in a contact area with radius a (Figure 2.6).

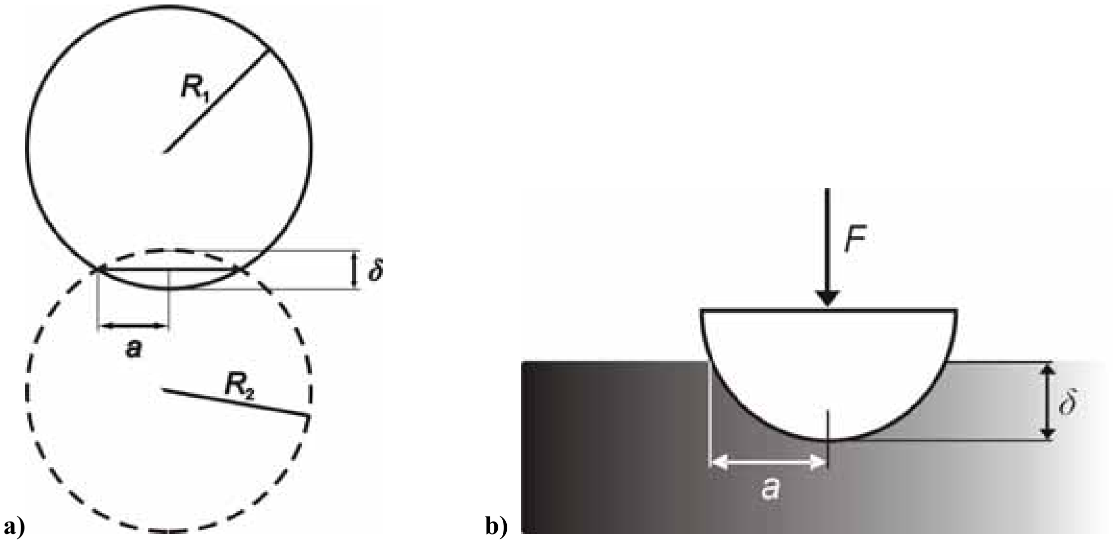

Figure 2.6 a) Hertz model of two compressed spheres (radii R_1 and R_2) with contact radius *a* and penetration depth δ and b) for an elastic sphere in contact with an elastic half space. For the purpose of a better illustration the dimensions are exaggerated.

The main assumptions made were: linear isotropic elasticity, small strains ($a << R_1$ and R_2), frictionless surfaces and no adhesion. Hertz determined the contact radius and the penetration depth δ as:

$$a^3 = \frac{3}{4}\frac{FR^*}{E^*} \qquad [2.7]$$

$$\delta = \frac{a^2}{R^*} \qquad [2.8]$$

where R^* describes the effective sphere radius and E^* the effective modulus defined as:

$$\frac{1}{E^*}=\frac{1-v_1^2}{E_1}+\frac{1-v_2^2}{E_2} \quad and \quad R^*=\frac{R_1R_2}{R_1+R_2} \qquad [2.9]$$

Here E_i are the Young's moduli and v_i the Poisson ratios of the two bodies. Combining equations [2.7] and [2.8] it becomes clear that the penetration depth δ is proportional to the $F^{2/3}$. The limiting case $R_2 \rightarrow \infty$ (spherical cantilever tip with radius R_1 on a flat surface) becomes important in SPM. Typical magnitudes specific for AFM are as follows:

- contact radius – up to 10 nm
- penetration depth – up to 20 nm
- contact pressure – up to 10 GPa

The fact that in this model adhesion is not considered leads to big errors in calculations where attractive forces play the dominant role. In most AFM experiments molecular interactions become important therefore Hertz' assumptions are rather relative in that case. In 1971 the Hertz model was extended to include adhesion effects by Johnson, Kendall and Roberts (JKR)[60].

2.4.2 The Johnson-Kendall-Roberts (JKR) model

The Johnson-Kendall-Roberts theory calculates the increase in contact area between two elastic bodies resulting from their mutual attraction. In their formulation the adhesion force can be understood as an additional Hertzian force (Figure 2.7 a). Thus the attraction weakens the force of elastic repulsion and is responsible for neck creation during separation. These additional specimen deformations take place before the sphere detaches at a finite contact radius a_0 (Figure 2.7 b).

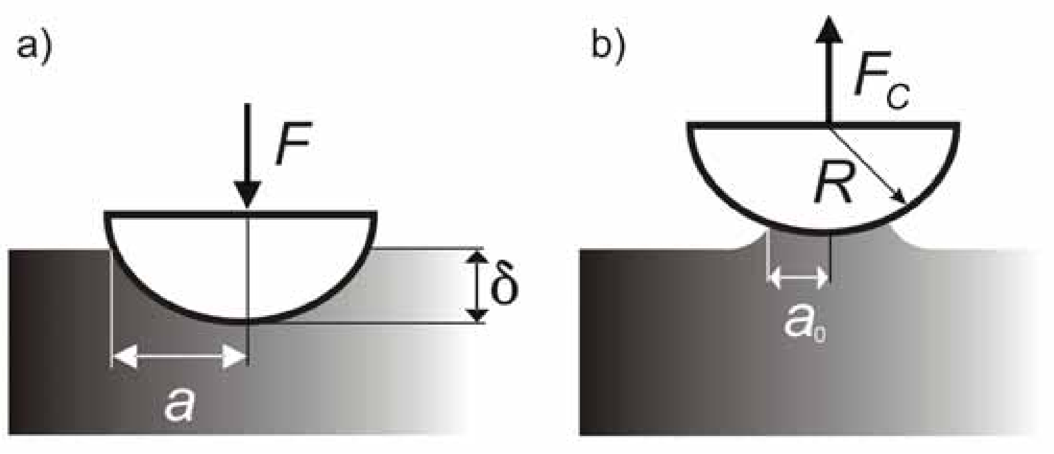

Figure 2.7 a) The adhesion force considered in the JKR theory can be understood as an additional Hertzian force *F*. b) Neck formation takes place before the sphere detaches at the pull-off force F_C and a finite contact radius a_0.

The attraction is described by the Dupré energy of adhesion $\gamma = \gamma_1 + \gamma_2 - \gamma_{12}$ where γ_1 and γ_2 are the respective surface energies and γ_{12} is the interfacial energy. The term γ corresponds to the work per unit area required to separate the surfaces. The JKR contact radius *a* is given as a function of the externally applied load *F* for an elastic sphere in contact with an elastic half space as:

$$a^3 = \frac{3}{4}\frac{R^*}{E^*}\left[F + \frac{3}{2}\pi R^* \gamma + \sqrt{3\pi R^* \gamma F + (\frac{3}{2}\pi R^* \gamma)^2}\right] \qquad [2.10]$$

where γ is the thermodynamic work of adhesion. In the absence of surface forces ($\gamma = 0$) equation [2.10] reduces to the classical Hertz model (equation [2.7]). The resulting sphere-plane pull-off force F_C is given as:

$$F_C = \frac{3}{2}\pi R \gamma \qquad [2.11]$$

This can be compared to the pull-off force measured in AFM experiments. Note that Young's modulus does not enter in the case of sphere-plane contact. Carpick *et al.*[61] used a Pt-coated AFM tip in contact with the surface of mica cleaved in ultrahigh vacuum to show that at low loads friction was proportional to the contact area as predicted by the JKR model. Although the theory shows good agreement when applied to AFM problems, a problem remains because this model predicts infinite stresses at the border of the contact area.

2.4.3 The Derjaguin-Muller-Toporov (DMT) model

The alternative thermodynamical approach by Derjaguin, Muller and Toporov[50] (DMT) assumes attractive forces to act in a circular area outside the contact zone, which results in a disappearance of the mathematical singularity. This model is applicable to AFM cantilevers with small tip radius *R*, high spring constant and low tip adhesion (hydrophobic surface). In DMT theory the sphere-plane pull-off force is given by:

$$F_C = 2\pi R\gamma \qquad [2.12]$$

Enachescu *et al.*[62] demonstrated in 1998 that the load dependence of the contact area in UHV-AFM experiments for an extremely hard single asperity contact is perfectly described by the DMT continuum mechanics model.

2.4.4 Comparison of the models

To compare the models described above (Hertz, JKR, DMT) it is necessary to introduce normalized parameters. Hence the contact radius $\overline{a}$, the force $\overline{F}$ and the penetration depth $\overline{\delta}$ are defined as:

$$\overline{a} = a\left(\frac{E^*}{\pi R^{*2}\gamma}\right)^{1/3}, \quad \overline{F} = \frac{F}{\pi R^*\gamma} \quad \text{and} \quad \overline{\delta} = \delta\left(\frac{E^{*2}}{\pi^2 R^* \gamma^2}\right)^{1/3} \qquad [2.13]$$

In table 2.1 the assumptions of the three theories with the corresponding normalized equations are presented at a glance for quick and easy comparison.

Model	Assumptions	Normalized equations
Hertz	Linear elasticity No adhesion No friction	$\bar{F} = \bar{a}^3$ $\bar{\delta} = \bar{a}^2$
JKR	Short-range surface forces acting within the contact area No friction	$\bar{F} = \bar{a}^3 - \bar{a}\sqrt{6\bar{a}}$ $\bar{\delta} = \bar{a}^2 - \frac{2}{3}\sqrt{6\bar{a}}$
DMT	Long-range surface forces acting outside the contact area No friction	$\bar{F} = \bar{a}^3 - 2$ $\bar{\delta} = \bar{a}^2$

Table 2.1 Model assumptions of the Hertz, JKR and DMT theories at a glance with the corresponding normalized equations.

2.5 Research on hairy attachment organs in geckos and other animals

In 1965 Ruibal and Ernst[5] performed combined light and electron microscope studies of the digital setae of geckos and other lizards. In contrast to *Anolis* and *Aristelliger,* they found *Gekko* setae to be longer and more complex, with numerous branchings. They determined that the free ends of the gecko setae consist of small flattened spatulas and suggested that the large spatular contact area is responsible for their high total frictional force.

Hiller[4] described the structure and function of adhesive pads in different gecko species in 1968. He measured the adhesive force of a whole animal as a function of the water droplet contact angle, an indicator of the substrate's free surface energy. Hiller found that the detachment force of *Tarentola m. mauritanica* increased linearly with substrate hydrophilicity. He also showed that the gecko's ability to cling to inclined surfaces weakened constantly over a period of one month after molting.

Russell[17] elucidated the functional morphology of *Gekko gecko*'s foot in 1975. Later he described the development of the subdigital adhesive pads of *Ptyodactylus guttatus* together with Rosenberg and Cavey[63]. This work focused on the entire attachment device. The authors pointed out that *all* hierarchical levels of the toe are important. Stork[64] compared the adhesive structures of lizards and anthropods. He showed that the attachment device dimensions varied for different lizard groups. In 1996 Irschick *et al.*[7] examined the clinging ability and the subdigital pad area in 14 pad-bearing lizard species from three families. They demonstrated that the clinging ability was tightly correlated with the pad area of the lizards. They also claimed that for a given pad area, the adhesive force varied among the families.

In 2000 Autumn *et al.*[8] reported direct friction and adhesion measurements of a single gecko seta. His measurements revealed that a seta adheres ten times more effectively than predicted from maximal estimates on whole animals. His hypothesis that individual setae operate by van der Waals forces was supported by adhesive force measurements and estimates from the JKR theory. In his experiments he used a microelectro-mechanical systems force sensor and a wire as a force gage. He also explained how the macroscopic orientation and preloading of the seta influences attachment forces. He discovered that increasing the angle between the setal shaft and the substrate to 30° aided detachment[6]. He contradicted surface hydrophilicity as a factor influencing the adhesive force. In fact, he claimed that the gecko adhesion is based on van der Waals forces[16] and rejected possible mechanisms relying on high surface polarity, including capillary adhesion. In his experiments the hydrophobic toes of live Tokay geckos adhered equally well to hydrophilic and hydrophobic, polarizable surfaces.

In 1957 Homann[65] showed that the number of scopulae of the spider *Heteropoda* increased with the animals age and mass. Additionally he observed that the spiders could cling to a certain glass surface. However, as soon as hydrophobic silane groups coated the same glass surface the animals could no longer adhere, which led to his hypothesis that spiders use ubiquitous monolayers of water to achieve good adhesion. In 1979 Bauchhenss[66] examined the pulvilli of *Calliphora erythrocephala* using light microscopy, fluorescent light microscopy, scanning electron microscopy and transmission electron microscopy. She reported several thousand, long, slender hairs with sole-like tips and showed that the adhesive strength depends on the pulvilli structure.

Gorb[67] studied the fly adhesive pad in 1998 and he showed that distal tenant setae are adapted to the delivery of an adhesive secretion. In 2001 Gorb *et al.*[68] revealed the scale effects on the attachment pads and friction forces in syrphid flies. Recently Langer, Ruppersberg and Gorb[69] reported setal adhesion forces of a fly. They showed that a terminal plate has a higher border and considerably lower centre and that the local adhesion was approximately twice as strong in the centre of the plate as at the border. Additionally they showed that adhesion strongly decreased with decreasing volume of the footprint fluid, indicating that the pad secretion layer covering the terminal plates is crucial for generating a strong attractive force. In 2003 Arzt, Gorb and Spolenak[70] revealed an inverse scaling effect in hairy attachment devices of animals with widely varying body weight, such as flies, spiders, and geckos. The bigger and heavier the animal, the smaller were the terminal elements responsible for the contact formation. This general trend was quantitatively explained by applying the principles of contact mechanics, which revealed that the setal areal density is proportional to the mass of the animal $m^{2/3}$.

Kesel *et al.*[33] used atomic force microscopy to show that a single spider setula can produce an adhesive force of ~40 nN perpendicular to a surface. In contrast to Homann[65] they assumed that van der Waals forces are the underlying adhesive forces, although final evidence has yet to be provided in their opinion.

More recently Sun *et al.*[71] measured spatular adhesion forces of a gecko by replicating the experimental setup reported by Kesel *et al.*[33]. Using AFM they claimed to measure single spatula forces in water and in air with varying relative humidities by the force-distance method. They found that the presence of water strongly affects the adhesion force and claimed that the dominant force involved is the capillary force. However, in both studies[33, 71], the experimental setup (consisting of a tipless cantilever approaching the respective hairy attachment organs from the top) was not completely controllable. As the cantilever approached the hairy array of either spider setulae or gecko spatulae, it is very unlikely that the detected forces came exclusively from a *single* contact between the AFM tip and the animal hair.

In summary, while many experimental studies were performed on several aspects of hairy attachment systems, to date neither adhesion forces of a single gecko spatula nor the mechanical properties of an isolated seta have been reliably measured. In fact, unambiguously measuring spatular adhesive forces would ensure that the changes in adhesion result from changes in the investigated parameter and not from changing the number of adhering spatulae. Additionally little is known about the influence of surface roughness on gecko adhesion. The aim of the present dissertation is to answer these important questions, which will also provide the fundamental basis upon which artificial attachment systems can be developed.

3 Resolving the Nanoscale Adhesion of Individual Gecko Spatulae by AFM

Abstract - Animals with different size and weight can adhere to and climb up vertical walls and even overhanging surfaces. This ability is caused by very efficient attachment structures which geckos have developed to greatest and subtlety and effectiveness. The adhesion mechanism in the millions of setae on their toes has been intensively investigated for decades. Adhesion forces of single setae on different substrates have previously been measured by a MEMS technique[8, 16]. Here the first successful experiments are reported in which the force-displacement curves were determined for individual spatulae by atomic force microscopy. The adhesion force for these smallest elements of the gecko's attachment system is reproducibly found to be about 10 nN.

3.1 Introduction

The structures of biological attachment systems follow two evolutionary principles. Comparative studies[72, 73] of hundreds of insects and other animal species suggest that (Figure 3.1):

- The ‘‘hairy’’ attachment system consists of finely structured protruding hairs with size ranging from a few hundred nanometers to a few microns, depending on the animal species.
- The ‘‘smooth’’ attachment system exhibits a relatively flat and adaptable surface covering a fine microstructure.

The function of both attachment systems is to enhance the adaptability to surface roughness of different levels of magnitude and to ensure intimate contact formation.

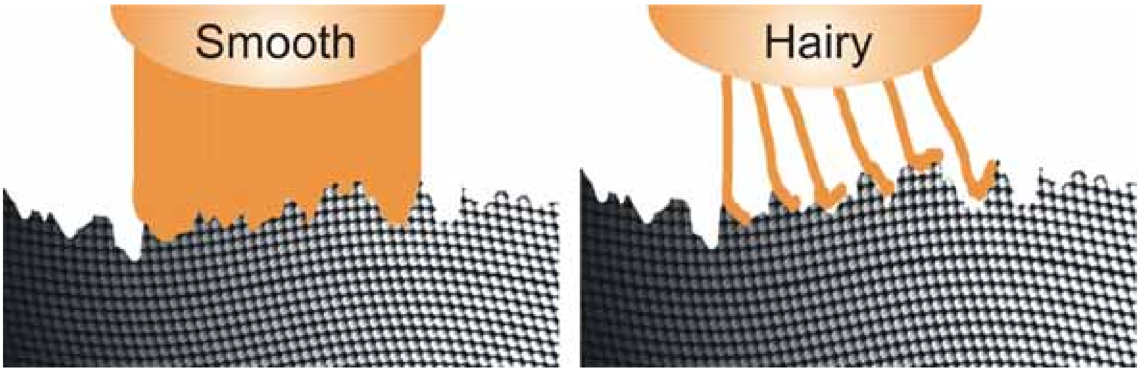

Figure 3.1 Schematic of a smooth and a hairy attachment systems adapting to a rough surface.

Understanding these intriguing attachment systems and the biological adhesion mechanism is an essential prerequisite for the bioinspired design of dry adhesive systems. It is therefore not surprising that the gecko, in particular, whose attachment system[5, 17] is the most elaborate in nature so far discovered[6, 7], attracts great scientific attention. Rosenberg *et al.*[63] described how gecko toes undergo several development steps before reaching their final structure. They showed that the subdigital pads (organs at the bottom side of gecko's digits) are made of integrated elements derived from the periderm and epidermis. The pads initially appear as paired swellings at the distal tips of the digits. As soon as the periderm is shed, the epidermal structure appears: The ventral side of the geckos toe bears so-called lamellae with arrays of 3-5 micron-thick setae, which in turn are subdivided at their tips into 100 to 1000 spatulae of 200 nm dimensions. The mean height of a gecko spatula could be measured analyzing AFM cross sections as shown in Figure 3.2.

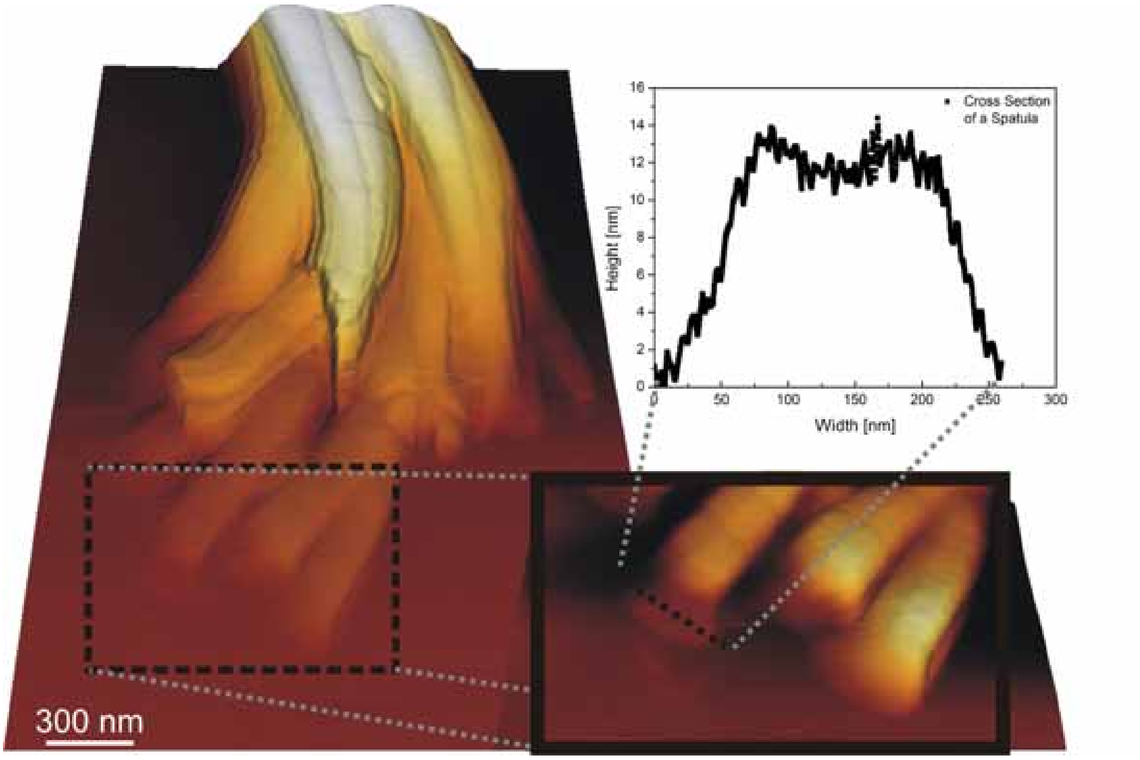

Figure 3.2 AFM based 3D-view of a gecko seta on a glass cover slip using intermittent-contact mode. The zoom provides additional insight of three spatulae adhering to the substrate. The inset shows the spatular height profile.

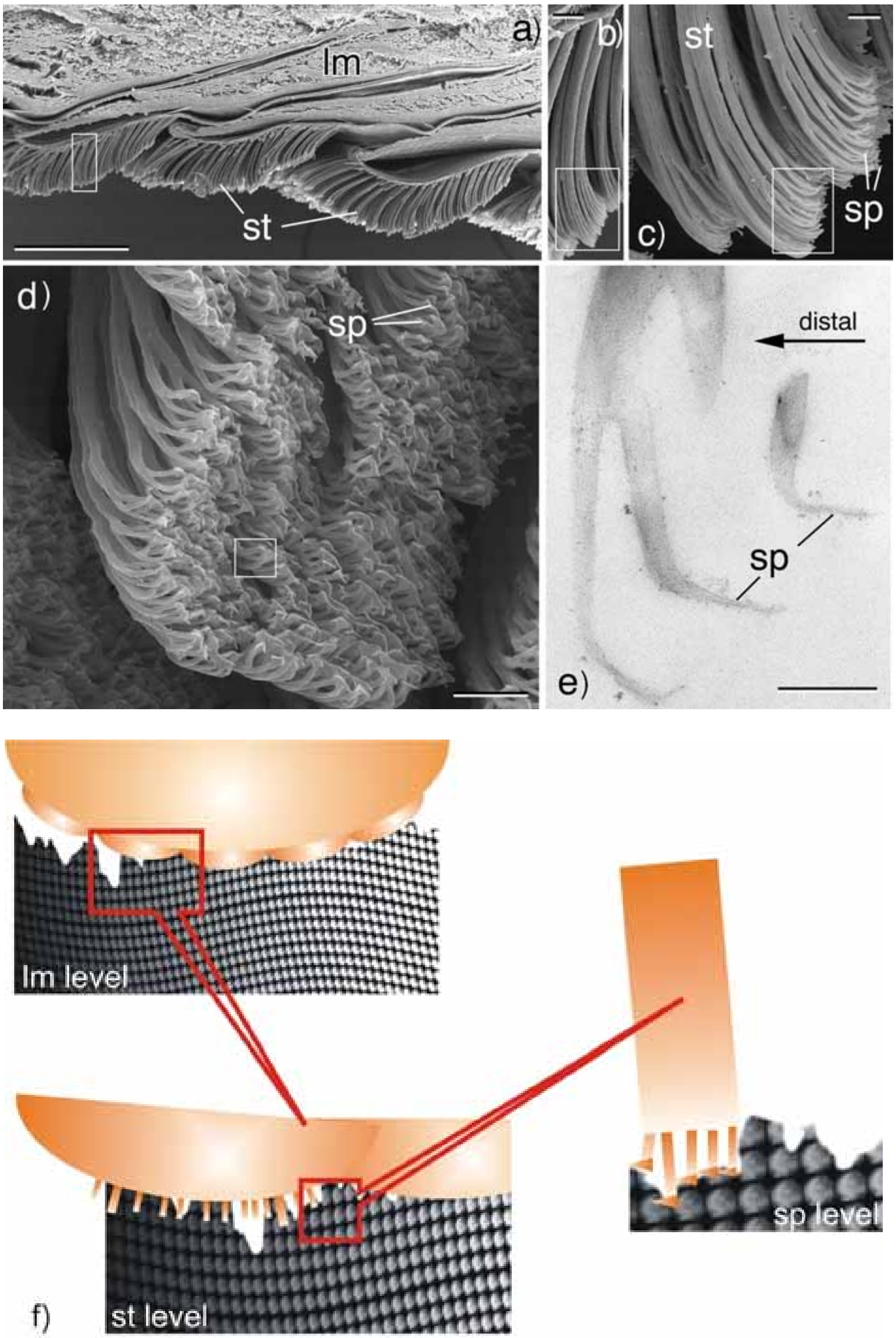

Figure 3.3 Hierarchical organization of the gecko attachment system. a) Longitudinal section of the gecko toe with three rows of lamellae (lm) covered with many setae (st) on the ventral side (scale bar = 200 µm). b) Single setae (scale bar = 10 µm). c)-d) Setae branching into spatulae (sp) (scale bars = 2 µm). e) Spatulae (scale bars = 300 nm) [a)-d) SEM; e) TEM; a)-e) courtesy of S. N. Gorb]. f) Schematic of the hierarchical organization: on the top the lamellae level is displayed, in the middle the seta level is reached and at the surface the contact formation is shown on the spatular level.

The lamellae, setae and tiny spatulae as shown in Figure 3.3 are responsible for the intimate contact with rough and smooth surfaces alike. The asymmetrical seta structure may have been developed to allow for both robust attachment and quick detachment[74] by toe peeling within 10 to 20 milliseconds[6]. So far several measurements at varying hierarchical levels corresponding to adhesion forces between µN and N have been reported for the gecko[4, 7, 8]. In the late sixties adhesion experiments with a whole animal were performed[4]. In 2000 adhesion forces of a single seta has been measured using a micro-electromechanical system (MEMS)[8]. The spatula level has, however, remained inaccessible so far. The aim of the present work was to determine the adhesion force of single spatulae by applying advanced methods of specimen preparation and force measurement.

3.2 Experimental

3.2.1 Preparation of the glass substrate

The substrate for the adhesion measurements was an alkali lime silica glass cover slip (Menzel Glasbearbeitungswerk GmbH & Co. KG, Braunschweig, Germany). First a “basic cleaning” was performed with 'piranha’ solution, i.e. a 1:1 mixture of concentrated sulphuric acid and hydrogen peroxide (30 %) for half an hour. Hereafter it was rinsed in fresh hot Millipore^{TM} water for 30 minutes. The standard cleaning procedure immediately before each experiment was as follows: the glass (peak-to-peak roughness < 10 nm) was cleaned again in an ultrasonic bath sequentially by toluene, acetone and ethanol. Accelerated drying was performed by dry nitrogen blown on the surface while the sample was already mounted in the AFM stage. For characterizing the wetting behavior the static contact angles of a sessile water drop were determined using the model of Owens and Wendt[75] by means of the contact angle system OCAH 230 (dataphysics instruments GmbH, Filderstadt, Germany). The water droplet contact angle amounted to ~58° for the cleaned glass cover slip.

3.2.2 Preparation of single spatulae

A single seta was sheared off a non-moulting, deep frozen gecko foot (*Gekko gecko*) with the aid of a needle tip. Using a binocular microscope the isolated seta was then glued to the end of well calibrated[76] contact mode cantilever (MikroMasch, Tallinn, Estonia). Gluing of inorganic particles to AFM cantilevers is well known to the scientific AFM community[77, 78] and served as a model. We used this knowledge to glue Si spheres to a tipless cantilever as displayed in the high resolution scanning electron micrograph (SEM: LEO 1530 VP, Carl Zeiss SMT Ltd., Cambridge, U.K., Figure 3.4). This cantilever had been used to investigate size effects in adhesion measurements within the scope of Holger Pfaff's Ph.D. thesis[79]. Additionally quantitative friction force measurements were performed in a non-gecko related project, which will not be described here.

Figure 3.4 Gluing of inorganic particles to AFM cantilevers is well known in the AFM community. Here a Si sphere was attached to a tipless cantilever to investigate size effects in adhesion measurements[79].

In detail the glue procedure of the organic material was as follows: a hair of an eyebrow was manually picked up by tweezers and brought into close proximity of the isolated seta (Figure 3.5 a). Once both hairs were close enough together the seta stuck to the eyebrow hair due to the intermolecular forces, which were acting at the intimate contact. Finally the seta could be transferred to the glue-covered cantilever tip.

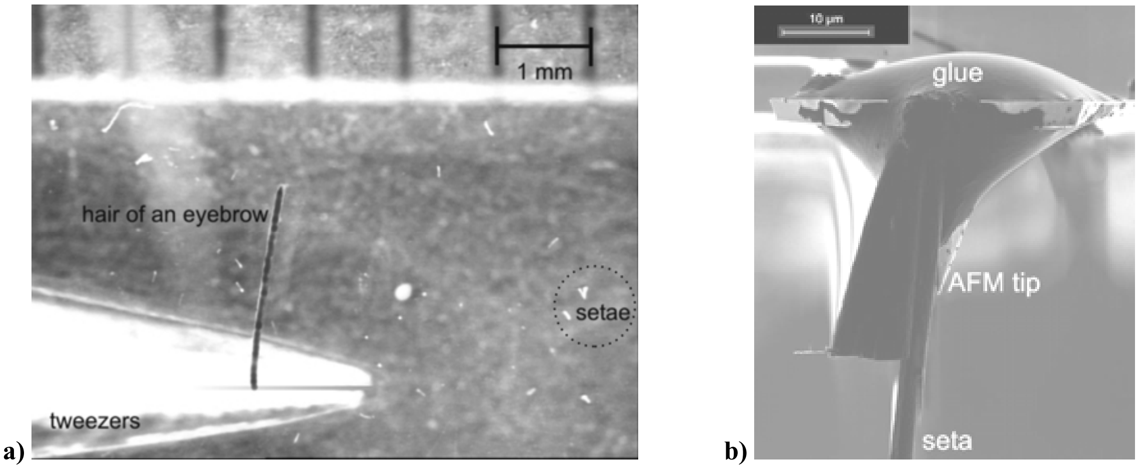

Figure 3.5 a) A hair of an eyebrow is held by tweezers and brought into proximity of isolated setae by means of a binocular microscope. b) Single seta glued to the cantilever close to the AFM tip using small amounts of UV curing glue.

As shown in Figure 3.5 b) small amounts of UV curing glue were used (Henkel Loctite Deutschland GmbH, München, Germany) to allow suitable alignment of the seta during the attachment procedure. The hair had to be perpendicular to the cantilever for correct force measurements. When the seta was positioned adequately, it was fixed by hardening with a UV lamp (maximum exposure time 10 min, wave length 366 nm). Hereafter the specimen was processed in a focused ion beam (FIB) microscope (FEI 200xP, Oregon, USA). Explaining the details of this microscope is beyond the scope of this work but an informative introduction to the technology and the operating principles of FIB can be found with Reyntjens and Puers[80].

Working with low currents (i.e. 11 pA) and starting on the cantilever tip at the glue dot the ion beam was moved along the stalk of the seta cutting off one hair after another at each emerging branch connection. To prevent radiation damage by the Ga^+ ions, imaging of the finally remaining spatulae was avoided. In the end all terminal branches of setae were machined away and a few isolated single spatulae $(N \leq 4)$ remained

(Figure 3.6). Using FIB it could be simultaneously verified that the glue did not spread along the stalk of the seta, which would have changed its mechanical properties. Finally the cantilever was installed in the AFM and the laser spot was positioned on the backside of the cantilever tip.

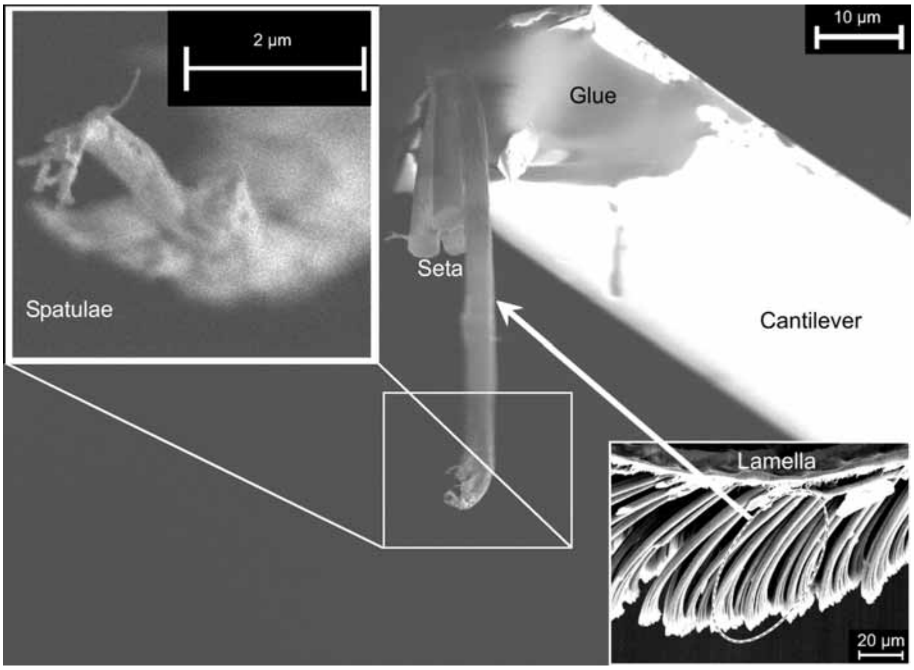

Figure 3.6 SEM image of a single seta glued to an AFM cantilever. Insets show lamellar structure at lower magnification (lower right) and four single spatulae isolated at the setal tip by FIB micromachining (upper left).

3.2.3 Force measurement for a single spatula during perpendicular pull

Several reports of AFM cantilever analysis and calibration have been published within the past years[81-85]. In this work the well established thermal noise method[76, 86] has been used to carefully calibrate the silicon contact-mode cantilever (CSC12/Cr-Au/50). The force resolution of the AFM amounts to several pN. Each spatula was brought in contact by applying a vertical preload. A force of 90 nN seemed to assure an ideal contact formation, while increasing the preload beyond this value did not lead to higher adhesion forces. Contact formation was achieved by automatically approaching the cantilever with the seta towards the glass while simultaneously monitoring the vertical deflection of the cantilever. Trying to mimic the biomechanics of the gecko a shearing movement of 7 µm parallel to the substrate surface preceded each adhesion measurement. This was possible by using a Java script developed by the AFM manufacturer (full details of the script are given in the appendix, a visualization of the cycle is given in Figure 3.7). It allowed shearing the seta in any desired way. The optimal direction had to be parallel to the spatular alignment and was defined by the alignment of the spatula relative to the cantilever beam, which had been known from the manipulation in the FIB. After shearing the cantilever was vertically withdrawn while simultaneously measuring the forces (512 or 1024 points per cycle). The pull-off force was defined as the minimum in the force-distance curves equivalent to the maximum tensile force a spatula could exert perpendicularly to the surface before complete detachment.

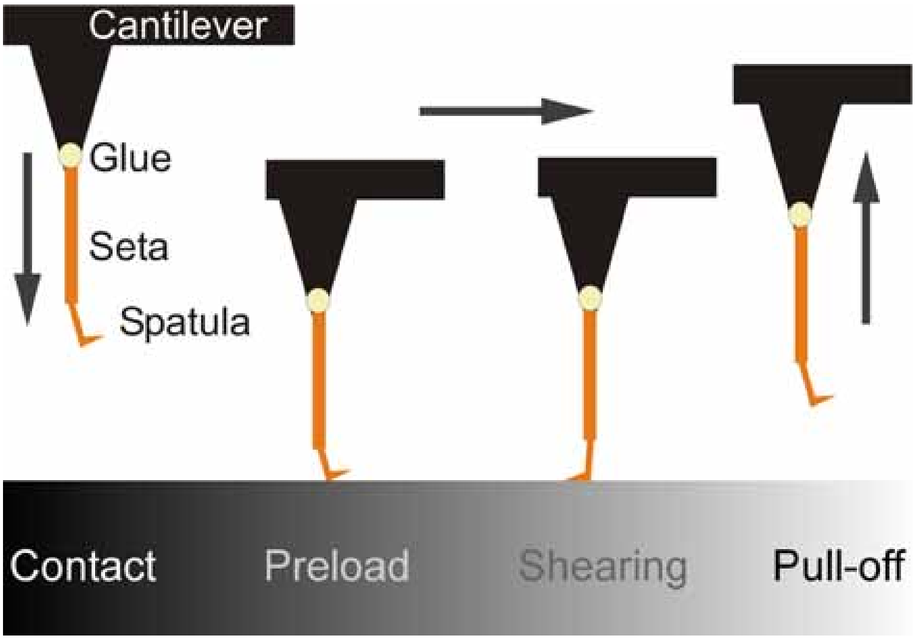

Figure 3.7 Experimental procedure: First, the spatula was brought into contact with a defined compressive preload perpendicular to the surface. Then, the specimen was sheared over a distance of 7 µm while maintaining the preload. Finally, the force-distance curve was measured during retraction, from which the adhesion force was extracted.

In this way, measurements for two different setae were made at ambient conditions (~50 %) monitored by a commercially available hygrometer (testo 177-H1, Testo AG, Lenzkirch, Germany). Ten measurements were performed at thirteen different locations on the glass cover slip for each seta, resulting in more than 200 data points. In addition, measurements (N = 65) were performed when the identical substrate was completely submerged under pure Millipore water^{TM}.

3.3 Results

The mean height of a gecko spatula could be measured analyzing AFM spatular cross sections as shown in Figure 3.2 and amounted to 11.2 ± 1.9 nm (mean value of ~500 measurements on ten different spatulae): The mean standard deviation for one spatulae was 1.6 nm. At ambient conditions for two different setae with four spatulae each, three typical force-distance curves were observed as shown in Figure 3.8.

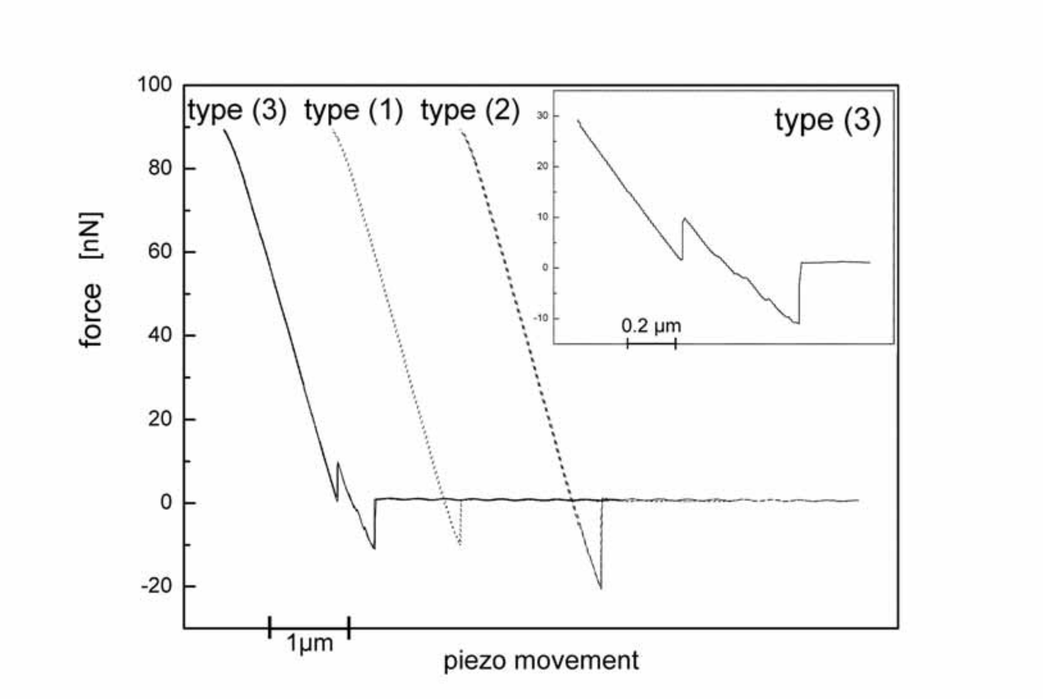

Figure 3.8 Typically observed force-distance curves (during the retraction phase) for a seta with an array of four spatulae at its tip. Three different types of curves were observed: Type 1: a pull-off force of approximately 10 nN, Type 2: pull-off force of roughly 20 nN, Type 3: two pull-off force maxima, suggesting sequential detachment events. The inset renders this curve in more detail.

Frequently (~120 times), type 1 was encountered which displays a maximum pull-off force of ~ 10 nN. Type 2 exhibits almost exactly twice this value. Finally, in type 3 (which occurred in about 5 % of the measurements) two serial pull-off events are seen. The first detachment force amounted to ~8 nN, whereas the second peak exhibited almost the same pull-off force (~10 nN) as measured in type 1. Figure 3.9 presents a histogram of the measured adhesion forces. It clearly shows two peaks at ~10 nN and ~20 nN. The first peak, which comprises 43.5 % of our experiments, lies at a mean value of 10.8 nN (with a standard deviation of 1.0 nN). 53.8 % of the measurements contribute to the second peak found at 20.4 ± 1.9 nN. A weak third peak can be identified at ~30 nN. A remarkable drop in adhesion force (2.4 ± 0.5 nN) of seta 2 was detected when the whole setup was completely submerged in pure Millipore^{TM} water.

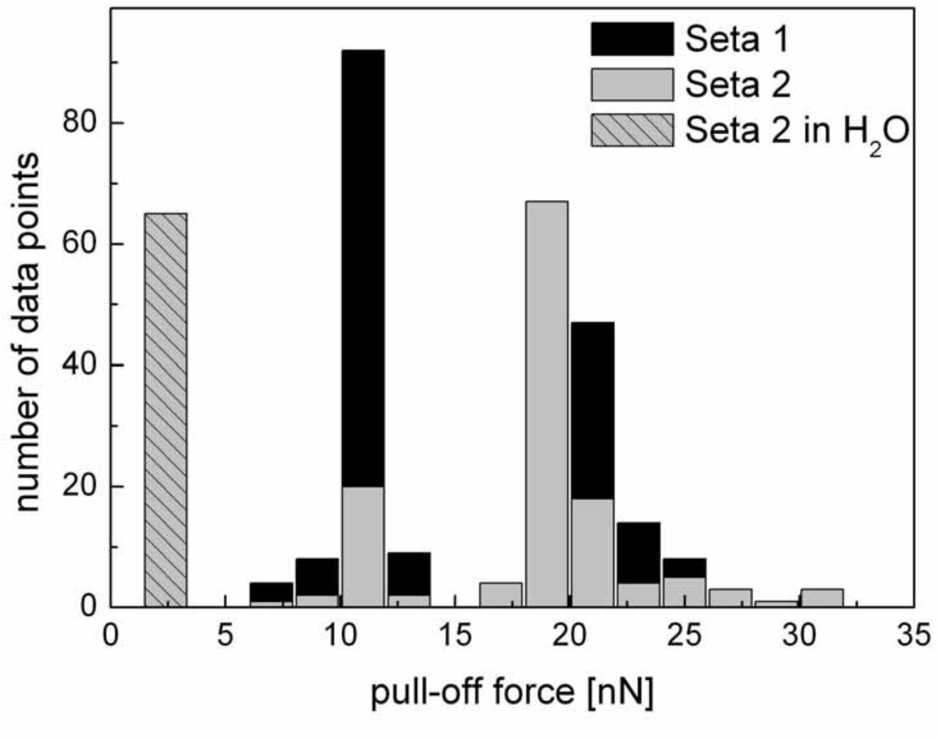

Figure 3.9 Frequency histogram of all measurements showing two strong peaks at 10.8 ± 1.0 nN and 20.4 ± 1.9 nN at ambient conditions. A weak peak is seen at ~30 nN. A further peak at 2.4 ± 0.5 nN is measured for seta 2 when completely submerged in pure Millipore^{TM} water.

3.4 Discussion

It stands to reason to correlate the measured pull-off forces with the number of spatulae in contact. From the force-distance curves the following sequence of events is therefore inferred (Figure 3.10): In type 1, exactly one spatula was in contact with the substrate before detachment, whereas in type 2 two spatulae detached simultaneously. Type 3, the most interesting case, can be explained by assuming that two of the four spatulae were initially in contact; on retraction, one of the spatulae detached first at a force of ~8 nN, whereas the second spatula exhibited the usual pull-off force (~10 nN). The reason for this difference may be due to a load shedding process caused by variability in spatula length or small differences in substrate height (Figure 3.10). The first spatula detaches very early at almost zero force. This can be ascribed to the shearing movement where repulsive elastic energy could be stored because of two reasons. One is that variability in spatula length causes the longer hair to store more elastical energy during the shearing movement than the shorter one and the second reason is analogically explained. As both hairs have the same length any difference in substrate height would have the same effect on the stored elastic energy leading to the earlier detachment of the virtually longer hair.

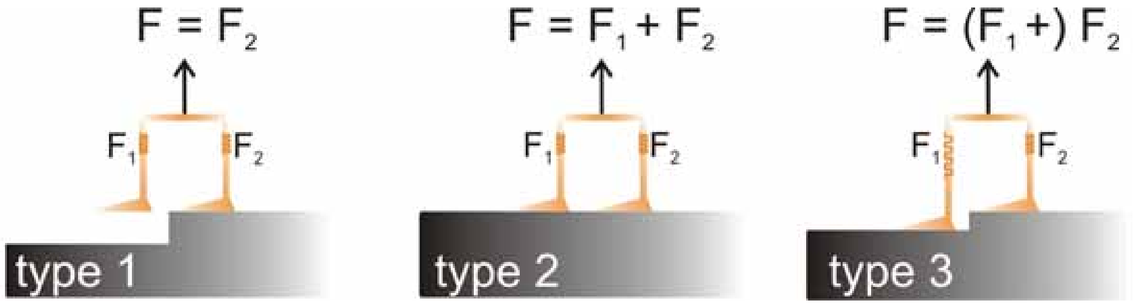

Figure 3.10 Schematic explanation of the experimental results for the three different detachment types.

The interpretation of the different detachment events is encouraged by the histogram of the measured adhesion forces (Figure 3.9). It is intuitive and reasonable to attribute the two strong peaks to the discrete number of spatulae adhering to the substrate. The first peak is assumed to correspond to a single-spatula separation whereas the second peak at ~20 nN is ascribed to a two-spatula detachment. The latter could result from two out of four different spatulae and was broader than the first peak at 10 nN due to the higher number of permutations. The weak third peak at ~30 nN may be due to three spatulae detaching simultaneously. As higher pull-off forces were not measured, the case of four spatulae in contact does not seem to have occurred in the experiments. The measured adhesion force of ~10 nN per spatula is in agreement with theoretical estimates and earlier results. We use the model developed by Johnson, Kendall and Roberts[60] (chapter 2.4.2) for the adhesive contact of a sphere with a semi-infinite half space to get an estimate for the work of adhesion γ.

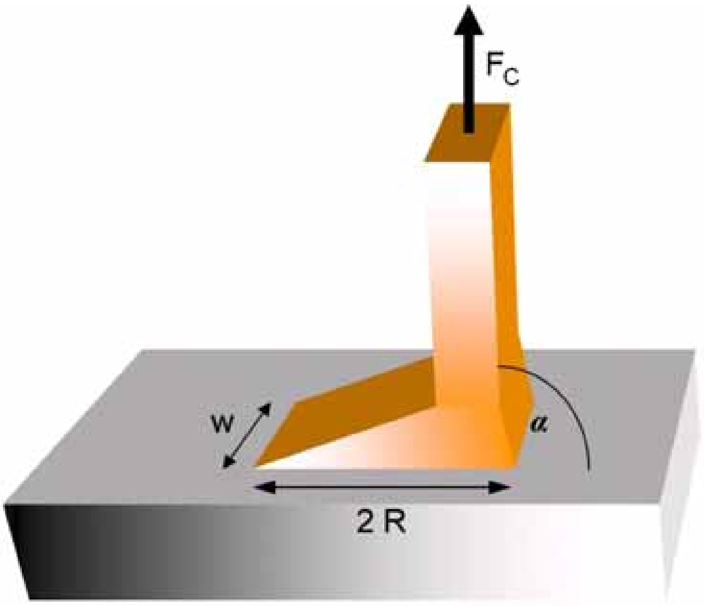

Figure 3.11 Sketch of a perpendicularly (α = 90°) contacting single spatula with length 2*R*, width *w* and pull-off force F_C.

Approximating the tip of the spatula by a sphere of radius $R = 100$ nm and setting the pull-off force $F = 10$ nN, one obtains:

$$\gamma = \frac{2F}{3\pi R} \approx 21\frac{mJ}{m^2} \qquad [3.1]$$

A similar estimate results from Kendall's considerations[87], which describe the force required to peel a thin tape with width w (assumption $w = 200$ nm) from a rigid substrate in perpendicular direction:

$$\gamma \approx \frac{F_C}{w} \approx 50\,\frac{mJ}{m^2} \qquad [3.2]$$

Both calculated values lie well in the range expected for interactions of intermolecular forces (10 mJ/m^2 - 100 mJ/m^2)[9]. The adhesion force of a whole gecko (with about 10^9 spatulae) can be estimated as 10 N. Considering a typical body weight of 50 g to 100 g, this would result in a "safety factor" of not less than 10. This large value supports the conjecture that only a fraction of the total number of spatulae is in contact with the substrate at any given moment. The small height (~11 nm) of the terminal elements probably helps the animal to bring these flat plates as close as possible to a large variety of surface topographies. Unambiguously defining the adhesive behavior of an individual spatula is fundamental to identifying the adhesion mechanism. The understanding of natural attachment solutions is a key to the exploitation of biomimetic structures for dry adhesive applications. Recent modeling has shown that the adhesive force of a fibrillar system can be increased by splitting up the contact into progressively smaller fibers[16, 70, 88]. This effect has also been theoretically studied as a function of contact shape[70, 89], with the result that at the nanoscale the shape loses importance. The question remains whether adhesion forces could be further increased for fibers considerably finer than gecko spatulae. The interplay between fiber radius, fiber aspect ratio, material and shape to find an optimal solution has been described in a recent paper[90]. One finds that while contact mechanics imposes limits on contact refinement, there seems to remain scope for improving the contact strength over that of the gecko. First prototypes of dry adhesives exhibit promising adhesive properties that partially substantiate the effect of contact splitting[79, 91-94].

The present results are not in disagreement with earlier measurements by Autumn *et al.*[8]. Dividing their setal adhesion forces, which range from 1 µN to 20 µN, by the number of spatulae per seta (100 to 1000), leads to an expected force value of the magnitude found in our experiments. These estimates (at ambient conditions) and the values found for the work of adhesion support in principle the hypothesis of Autumn *et al.*[16] that van der Waals forces are responsible for gecko adhesion. At least they let suggest that at ambient conditions vdW forces are sufficient for gecko adhesion and of the same order of magnitude as any other conceivable attractive force contribution.

However, comparing equations [2.4] and [2.6], it becomes clear that capillarity contributions are of the same order of magnitude as van der Waals forces. In ambient conditions most rigid surfaces are covered by a few monolayers of water, which was also the case in our experiments. However, changing from a few monolayers of water on top of the glass cover slip to a completely submerged experimental setup a remarkable drop (almost five times smaller) in spatular adhesion force was measured. This effect has also been reported for completely different adhesion phenomena[9].

3.5 Summary

This chapter described a sophisticated experiment that allowed the first measurements of the adhesive properties of individual gecko spatulae by combining focused ion beam micromachining of biological materials with sensitive AFM measurements. Mimicking the biomechanics of the gecko the experiments yielded adhesion forces which, due to refinement of the contact elements, were in the 10 nN range (three orders of magnitude finer than the previous measurements[8]). Extrapolating this value resulted in a “safety factor” of not less than 10 for the whole animal at ambient conditions. A remarkable drop in pull-off force was detected when the whole setup was completely submerged in water. Additionally AFM measurements revealed the extreme flatness of these final contact elements. Being only ~11 nm thick, the flexible spatula in its unique combination with the higher hierarchical levels (seta and lamella) allows the animal to adapt to almost any surface roughness (chapter 5).

4 Evidence for Capillarity Contributions to Gecko Adhesion

Abstract - The hairy attachment system on a gecko toe, consisting of one billion spatulae in the case of *Gekko gecko*[5], allows it to adhere to almost any surface topography. This chapter details the first measurements of the adhesion force exerted by a single gecko spatula for various atmospheric conditions and surface chemistries. Through judicious choice and modification of substrates, the short-range and long-range adhesive forces are separated. In contrast to previous work[16], the measurements clearly show that capillarity significantly contributes to gecko adhesion on a nanoscopic level[95]. These findings are crucial for the development of artificial, biomimetic attachment systems.

4.1 Introduction

To date, gecko adhesion experiments were performed on the level of a whole foot[4, 7] or of a single seta[8] (still consisting of 100 to 1000 spatulae). As shown in chapter 3, combining focused ion beam micromachining with atomic force microscope measurement techniques has made it possible to determine the pull-off force of even a single spatula[96]. The present chapter describes how this nanomechanical technique has been used to shed new light on the gecko adhesion mechanisms in the presence of water.

The dominant mechanism of gecko adhesion is still a matter of debate. Early[4, 97] and recent studies[98] of gecko adhesion invoked capillary forces due to macroscopical liquid bridges, whereas a recent investigation[16] rejected the contribution of capillarity and indicated that van der Waals forces alone give rise to the high adhesion observed. It is well known that even a monolayer of water, always present on surfaces under normal atmospheric conditions[99, 100], can significantly influence the attraction between two surfaces[98, 101-105]. In view of the recent results obtained by Autumn *et al.*[16], the controlling adhesion mechanism remains inconclusive.

The present detachment experiments on the spatular level were performed with substrates of varying degree of hydrophilicity (water droplet contact angle) and as a function of air humidity. As the gecko exhibits a dry adhesion system and does not produce secretion, any capillarity effects must be due to the air humidity controlled in our experiment. The specimen preparation and measurement technique is the same as described in the previous chapter. It is based on AFM detachment experiments of spatulae isolated by micromachining with a focused ion beam microscope (Figure 3.6). Only pull-off forces of single spatulae are reported; in cases where two spatulae detached simultaneously, the force value was halved. In total, about 600 detachment measurements were performed on two setae with four spatulae at their ends.

4.2 Experimental

4.2.1 Preparation of the substrates

Silicon wafers of type N were supplied by Wacker Siltronic GmbH, Burghausen, Germany, and type T wafers by SilChem Handelsgesellschaft GmbH, Freiberg, Germany. The thickness of the amorphous Si oxide layers was determined by ellipsometry (EP^3, Nanofilm, Göttingen, Germany)[106]. These wafer surfaces were modified in two different ways resulting in different wetting properties[107, 108]. After the wafers were cut, the remaining pieces were cleaned with a snow jet (a fast CO_2 jet containing CO_2 crystals; Tectra GmbH, Frankfurt/Main, Germany) to remove microscopic contaminations. The samples were then treated with 'piranha’ solution, i.e. a 1:1 mixture of concentrated sulphuric acid and hydrogen peroxide (30 %) for 30 min. They were rinsed in fresh hot Millipore^{TM} water for 30 min immediately before the adhesion experiments. To produce hydrophobic substrates, they were covered with a monolayer (2.4 nm thick) of octadecyl-trichloro-silane (OTS, Aldrich Chemie, Steinheim, Germany). Before the experiments, they were cleaned in an ultrasonic bath by ethanol, acetone and toluene. The last cleaning procedure was also done for the alkali lime silica glass cover slip.

4.2.2 Force measurement for a single spatula

Two types of experiments were performed: First, substrates with surfaces of different contact angles for Millipore^{TM} water were produced by varying the surface chemistry of Si wafers by silanization. The substrate types used were wafers with different thicknesses of the top amorphous Si oxide layer (‘N’ stands for the natural ~2 nm thin oxide layer, ‘T’ for the thermally grown thick ~192 nm layer). The static contact angles of a sessile water drop were determined by means of the contact angle system OCAH 230 (dataphysics instruments GmbH, Filderstadt, Germany). When thoroughly cleaned, the Si oxide surfaces were hydrophilic (water droplet contact angle of about 10°). Both wafer types were alternatively covered by a hydrophobic monolayer of silanes (OTS) causing water droplet contact angles greater than 100°. This resulted in four types of substrates, abbreviated in the following as 'N-phil', 'N-phob' as well as 'T-phil' and 'T-phob'. Contrary to earlier studies with different substrate materials[16], the investigation presented here allows to separate effects of short-range forces from those of long-range interactions: substrates exert either identical short-range but different long-range forces (N-phil and T-phil *vs.* N-phob and T-phob) or different short-range but similar long-range forces (N-phil and N-phob *vs.* T-phil and T-phob)[107, 108]. The roughness of all surfaces was comparable (N-type: RMS below 0.15 nm, T-type: below 0.2 nm). For comparison with the earlier data[96], the same flat alkali lime silica glass (water droplet contact angle 58.4 ± 2.7°) was used again. Additionally an Aquacer® coated Si-wafer (BYK-Chemie GmbH, Wesel, Germany) was investigated to complete the experimental series.

The second type of experiment involved systematic and controlled variation of air humidity. The experimental setup consisted in an AFM, which had been placed in an airtight container. Inside this container the humidity level was adjusted by varying the flow rate of dry nitrogen and continuously monitored by a commercially available hygrometer (testo 177-H1, Testo AG, Lenzkirch, Germany). Additionally the increase in thickness of the water layer on a wafer surface was measured by ellipsometry, as a function of humidity[106]. As an extreme case, detachment experiments were also performed for the N-phil and the glass substrates when completely submerged under fresh Millipore™ water.

4.3 Results

Figure 4.1 shows the results of the spatular detachment measurements for the four different types of Si wafers as well as for the glass and the Aquacer® coated substrate, all at ambient temperature (25 °C) and humidity (52 %). Significantly higher pull-off forces were recorded for both hydrophilic wafers, N-phil and T-phil, compared to the N-phob and T-phob substrates. In detail the N-phil surface (contact angle 10 ± 7°, N = 5 each) gave pull-off forces of 18.4 ± 3.5 nN (N = 60 each).

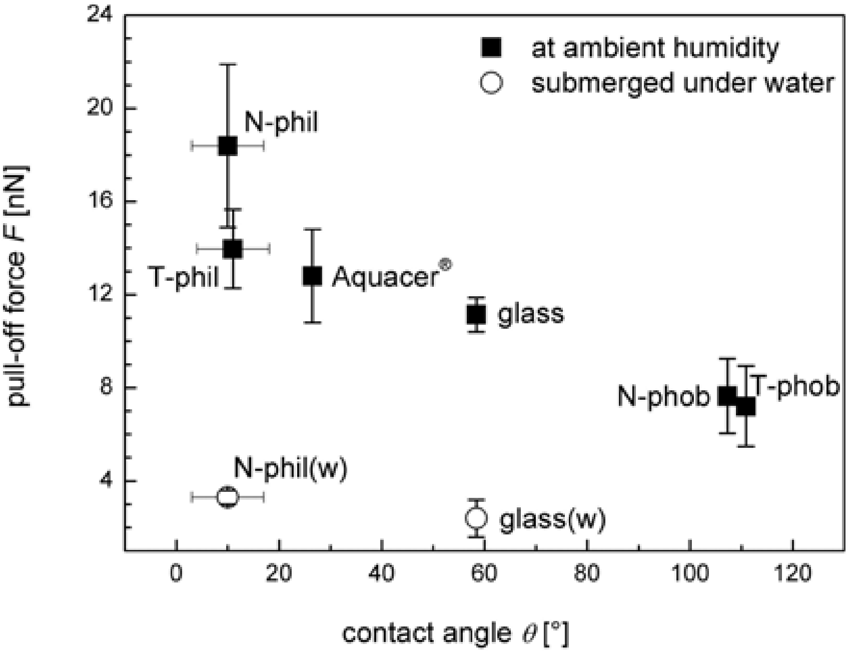

Figure 4.1 Spatular pull-off force *vs.* contact angle θ of a water drop on four types of Si wafers and on glass. Wafer families N and T differ by the thickness of the top amorphous Si oxide layer. The 'phob' type was obtained from 'phil' type wafers by deposition of OTS. The relative humidity during the experiment was 52 %. For comparison, the pull-off force on a glass substrate ($\theta = 58.4^{\circ}$) measured at comparable humidity (glass square data point taken from measurements displayed in Figure 4.2) is included. Aquacer® is a commercially available coated Si wafer (θ = 26.5°). Additionally pull-off forces of one spatula when completely submerged under water (open circles labeled with glass(w) and N-phil(w)) are displayed.

The adhesion force was slightly lower (14.0 ± 1.7 nN) on the T-phil substrate (11 ± 7°). The pull-off force was reduced by a factor of ~2.4, to 7.7 ± 1.6 nN, on the N-phob surface (107.3 ± 0.6°). A further small decrease in adhesion was found for T-phob substrate (110.9 ± 0.7°). Here the adhesion force averaged 7.2 ± 1.7 nN. On the

Aquacer® coated Si-wafer (26.5 ± 2.5°) an average value of 12.8 ± 2 nN was detected. For the glass substrate, the pull-off forces were high when measured at ambient humidity (11.1 ± 0.7 nN). When submerged in water, strongly reduced values were found, i.e. 2.4 ± 0.8 nN for glass and 3.3 ± 0.3 nN for N-phil (N = 65). The detachment forces were sensitive to the presence of the OTS layer but not to the thickness of the oxide layer (N *vs.* T-type). This proves that adhesion was determined by short-range forces, while long-range forces are insignificant. It is essential to note that detachment distances in van der Waals adhesion are typically smaller than a nanometer and independent of the strength of the force, i.e. of the Hamaker constant. Therefore the long-range part of the attractive dispersion force is indeed irrelevant and the pull-off force is directly proportional to the minimum value of the potential. This minimum is influenced solely by the chemical composition of few layers at the outermost surface of the substrates.

Figure 4.2 displays the spatular pull-off forces on the glass surface as a function of air humidity. Similar to the results in Figure 4.1, the pull-off force values varied by up to a factor of ~2. In virtually pure nitrogen atmosphere (~1.5 % humidity, which is the lower detection limit of the hygrometer) the adhesion force was found to be 6.4 ± 0.6 nN, N = 10 for specimen 1 and 7.0 ± 0.1 nN, N = 10 for specimen 2. With increasing humidity, the adhesion forces were found to increase in a monotonic manner; the increase was roughly linear for specimen 1, and exhibited a steeper initial slope followed by a plateau-like behavior in specimen 2.

The maximum forces for both specimens were almost identical (12.1 nN for specimen 1 and 12.3 nN for specimen 2). These experiments were highly reproducible: Refilling the container with pure nitrogen resulted in the same previously measured minimum pull-off force of ~7 nN. The same experiments conducted on the N-phob substrate resulted in a much smaller increase of adhesion force and larger scatter in the data. The inset in Figure 4.2 shows the result of the ellipsometric thickness-increase measurements of the water layer on a N-phil wafer[106]. At a humidity of 88 %, the original film thickness on the wafer increased by ~0.2 nm, which roughly corresponds to one additional monolayer of water. Therefore in our experimental setup we had at least a partial or insular coverage of the substrate by a monolayer of water.

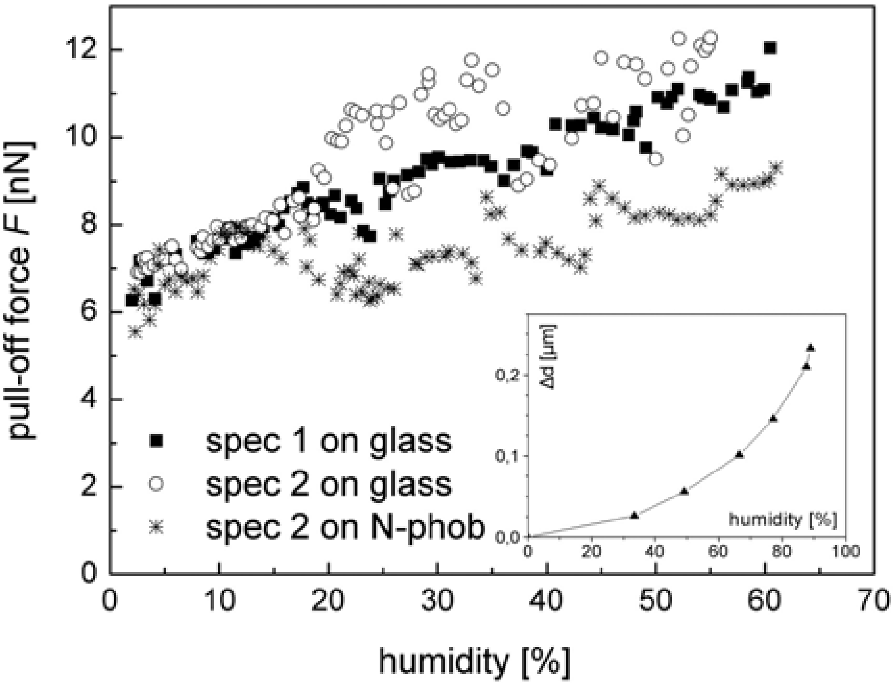

Figure 4.2 Spatular pull-off forces of two different specimens on glass and N-phob versus humidity at ambient temperature. The inset shows the increase Δd in water film thickness on a N-phil wafer with increasing humidity as measured by ellipsometry[106].

4.4 Discussion

The essential finding of this study is that the adhesion force of a gecko spatula rises significantly for substrates with increasing hydrophilicity (Figure 4.1) and with increasing levels of air humidity (Figure 4.2). This striking behavior suggests that water layers between spatula and substrates can exert an important influence on the adhesion forces. Both types of experiments are essential for this conclusion because a change in surface chemistry alone (Figure 4.1) cannot differentiate between humidity and van der Waals effects. Hiller[4] reported that the adhesion of living geckos increases with decreasing water droplet contact angle. In his study the gecko *Tarentola m. mauritanica* was investigated. This animal exhibited an adhesion force of ~235 mN to rigid polyvinyl chloride (θ = 55°). Normalizing this force by the spatular force (~11 nN) for the glass cover slip (θ = 58.4°) obtained in this study gives an estimate of the number of spatulae in contact ($N \approx 2.1 \cdot 10^7$). By assuming the same number of spatulae to be in contact in all experiments we obtain the open circles shown in Figure 4.3. Our data qualitatively show a good correlation with his results even though the dependence on water droplet contact angle seems to be more pronounced.

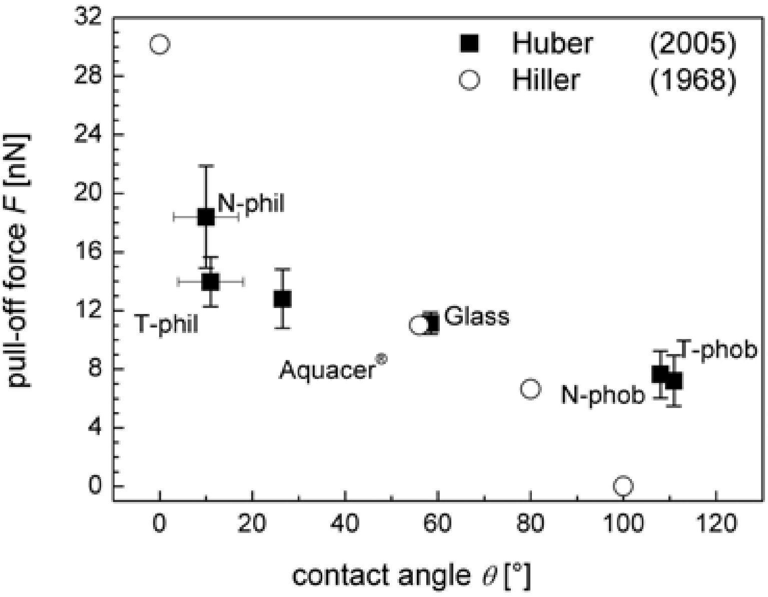

Figure 4.3 Spatular pull-off forces of *Gekko gecko* (Figure 4.1) in comparison to Hiller's data for *Tarentola m. mauritanica* standardized to spatular adhesion forces.

It is instructive to verify whether the magnitude of the increases in adhesion force is also reasonable from a theoretical point of view. In principle the experimental data (Figure 4.1 and Figure 4.2) can be explained in two ways: (a) by capillary forces due to nanobridges or (b) by a change of the effective short-range substrate interaction due to adsorbed monolayers of water.

4.4.1 Explanation by capillary forces due to nanobridges

In the context of gecko adhesion a macroscopic interpretation by standard capillarity[103] must be considered with caution. Humidity dependence of adhesion in the presence of water is a complex subject, which has received considerable attention over recent years e.g. references[109-111]. The required water amount classically depends on the contact angles of the surfaces and on the relative humidity[105]. The ellipsometry data confirmed that only adsorbed monolayers of water were present[106]. As a possible explanation we attempt a description by the following model. Tiny water bridges (nanobridges) are assumed to contribute to gecko adhesion. Although of molecular dimensions, the attractive interactions due to the presence of the nanobridges will be described by macroscopic capillarity. Next we assume that the number of nanobridges scales with relative humidity. Classically the capillary force between two flat surfaces with water droplet contact angle θ at a separation distance D can be derived from Laplace's equation [2.5]. Considering the rectangular triangle (ABC) with r_1 as one of the principal radii of surface curvature, it is true that (Figure 4.4)[112]:

$$\cos(\theta) = \frac{D/2}{r_1} \qquad [4.1]$$

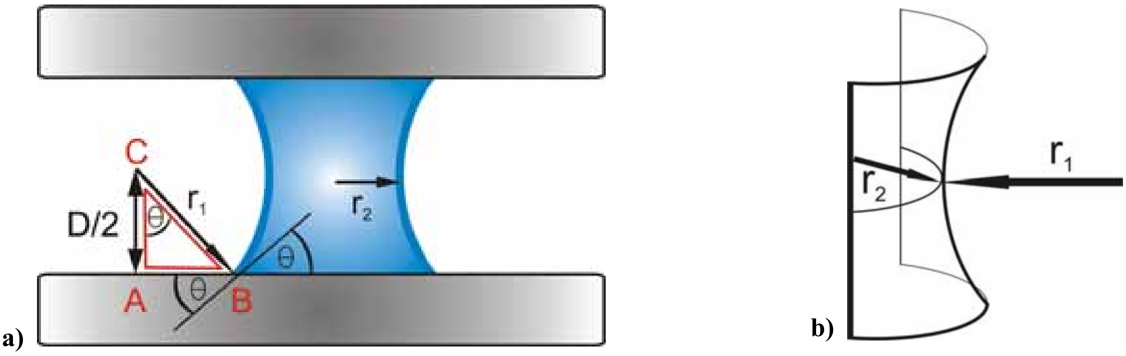

Figure 4.4 A capillary bridge (radii r_1 and r_2) between two surfaces (water droplet contact angle θ) at a separation distance D a) plane-view b) 3D-view.

Combining equations [4.1] and [2.5] leads to the capillary force F_{nb} due to one nanobridge between two flat surfaces[112]:

$$F_{nb}(\theta) = \pi\, r_2^2 \gamma_L \left(\frac{2\cos\theta}{D} - \frac{1}{r_2}\right) \qquad [4.2]$$

where γ_L is the liquid/vapor surface tension (72.5 mJ/m^2 for water/air). Only positive contributions of F_{nb} are assumed. Furthermore an empirical equation $N(h) = \beta \cdot h$ was used to calculate the number N of nanobridges as a function of relative humidity h (Figure 4.5); β is a fit factor. It is assumed that the dry spatular regions additionally contribute to the adhesion. Therefore the total adhesive force is composed of both the van der Waals force F_{dry} and the force contribution due to N nanobridges F_{nb}:

$$F(h,\theta) = F_{dry} + N(h) \cdot F_{nb}(\theta) \qquad [4.3]$$

where F_{dry} is the vdW force of the dry spatula, which amounts to about 7 nN for the glass substrate as well as for the T and N-phob wafers. The full amount of F_{dry} is used in equation 4.3 because the spatular surface area covered by the nanobridges will be found to be very small.

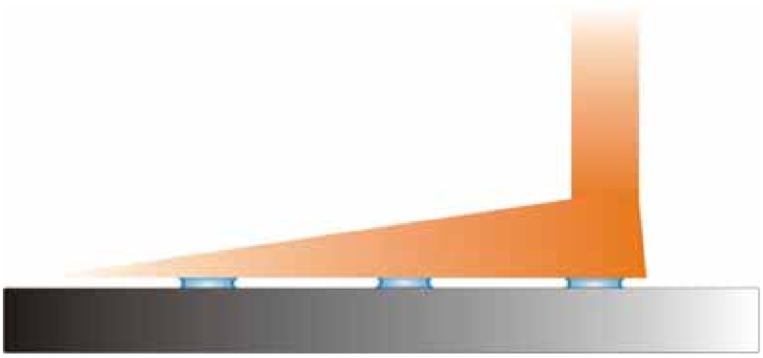

Figure 4.5 Sketch of the assumption that at a few nucleation sites nanobridges form between spatula and substrate. Since the nanobridge height corresponds to one monolayer of water the rest of the spatula is assumed to be in dry contact with the substrate

The following parameters were chosen: Since at least one monolayer of water molecules contributed to the nanobridge height, the separation distance D between spatula and substrate was estimated to be of the same order of magnitude as the size of one water molecule ($D \approx 0.32$ nm)[113]. Assuming nanobridges, the radius r_2 was arbitrarily set to be constant at 1 nm. The capillary force contribution due to one nanobridge between a spatula and the glass substrate amounts to $F_{nb}(\theta = 58°) \approx 0.53$ nN. The combination of macroscopic capillarity with the molecular model of nanobridges (eq. 4.3) fits the experimental data well for $\beta = 16$, as is shown in Figure 4.6 a) and b).

The motivation for this model is based on three facts. At first it is known from recent work that tiny amounts of water are more wetting than macroscopical amounts[114, 115]. An explanation for this is that water molecules appear preferentially on the most wettable spots of the surface, acting as nuclei for further condensation. Secondly as described in chapter 2.3.3 it is possible that subtle time-dependent surface changes due to humidity exposure lead to wettable regions on a hydrophobic surface[52-54]. This could be also true for the gecko spatula: the formerly non-wettable terminal element could be locally rendered hydrophilic leading to the formation of nucleation sites. In this context two comparisons seem reasonable to support the motivation: (a) in materials science it is known that in metallic melts also just a few atoms act as nucleation sites for the origin of a new phase; (b) in our universe small temperature fluctuations in the cosmological radiation also act as nucleation sites for the origin of new structures[116]. The third motivation results from the fact that thermodynamical calculations (classical theories) are surprisingly stable to small dimensions, which is also known in materials sciences (e.g. solid solution hardening).

The complex intermolecular interactions when completely submerged in a third medium such as water are beyond the scope of this model. Due to the large number of different forces involved and their highly complicated interactions only qualitative explanations can be given below.

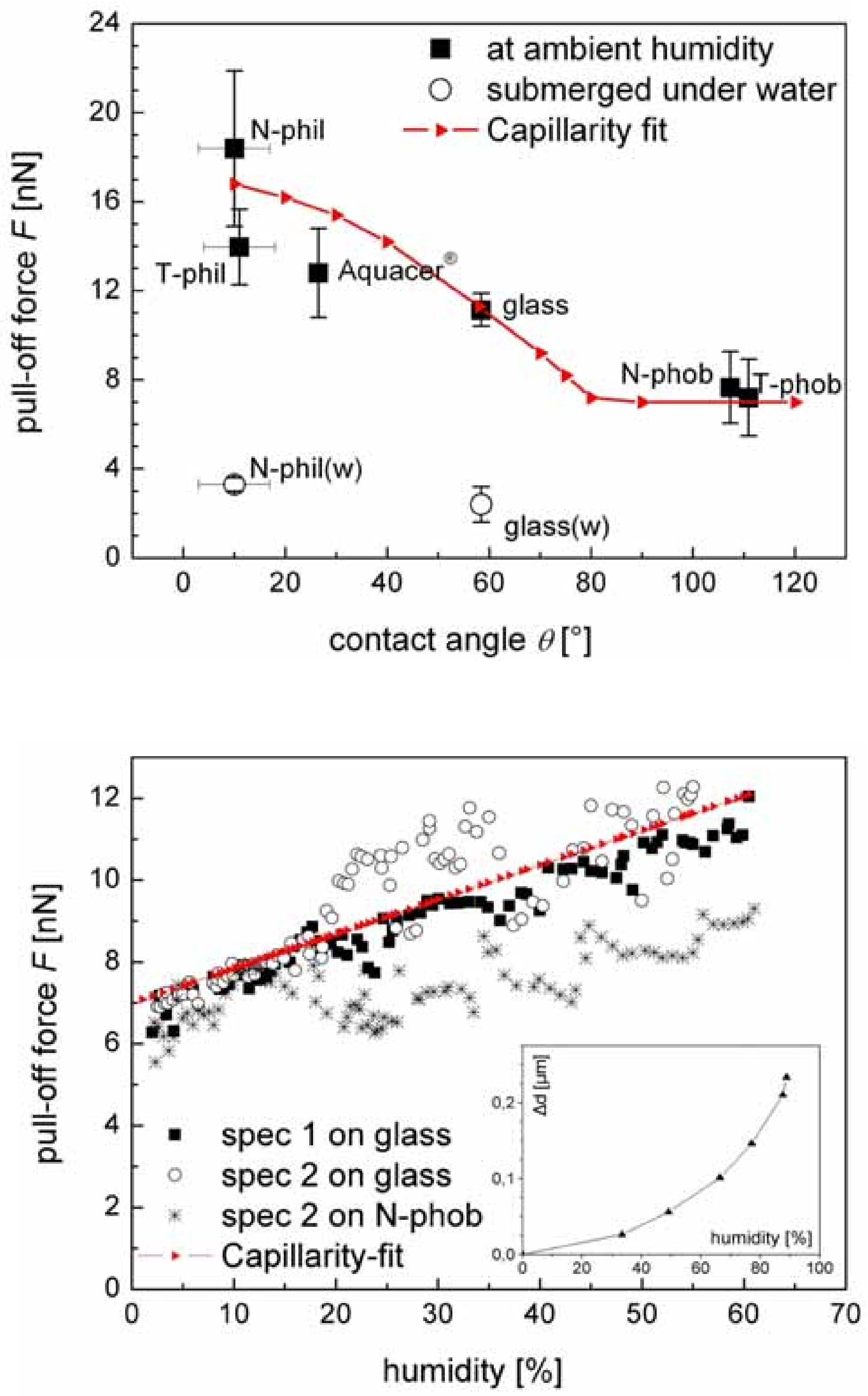

a)

b)

Figure 4.6 Fitting curves according to equation [4.3] which are showing good agreement of the "nanobridge model" with the experimental data of Figure 4.1 and Figure 4.2.

The following explanations hold also for the results found in chapter 3.3. As the experimental setup is completely submerged in water any contribution due to the presence of nanobridges or macroscopical capillary bridges can be excluded. Additionally the contributions of the vdW forces (F_{dry}) will be reduced because H becomes drastically smaller due to the high permittivity of water (~80). Moreover when immersed in a polar liquid such as water, surface charging of the spatula and of the sample surface may be induced by the fluid. This can occur either by ionization or dissociation of the surface species, or by adsorption of ions from solution. In such a case a diffuse electrical double layer forms. Due to the repulsive interaction between hydrated ions a strong long-ranged repulsive force (namely the hydration force) is observed. Thus, if present, this effect contributes additionally to the decrease in adhesion force.

4.4.2 Explanation by a change of the effective short-range substrate interaction due to adsorbed monolayers of water

The experimental data can also be interpreted as a consequence of a change in Hamaker constant due to adsorbed monolayers of water between spatula and substrate[117]. One assumption is that an areal fraction f of the spatula is in direct contact with the substrate. Additionally, a fraction f' of the spatula is in contact with the substrate through a monolayer of water. Their ratio $g(\theta) = f'/f$ is a geometrical factor depending on the water droplet contact angle of the surface similar to the $N(h)$-concept in the previous section (Figure 4.7). Assuming that the amount of liquid is in thermal equilibrium with the vapor phase, the relative water coverage ρ is given by Langmuir's adsorption isotherm[117, 118]:

$$\rho = \frac{h}{h + \exp(-E_a/k_B T)} \approx h \cdot \exp(\frac{E_a}{k_B T}) \approx 1.22h \qquad [4.4]$$

where h is the relative humidity and E_a is the adsorption energy which is typically much smaller than the thermal energy k_BT at room temperature.

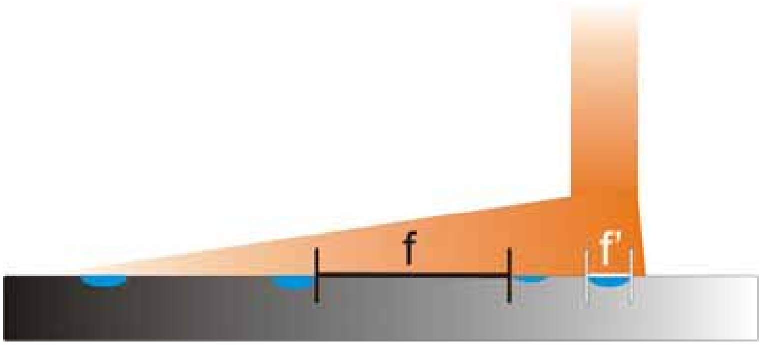

Figure 4.7 Sketch of the assumption that an areal fraction *f* of the spatula is in direct contact with the substrate. Additionally, a fraction *f'* of the spatula is in contact with the substrate through a monolayer of water.

Above, we have assumed for the hydrophilic substrates $E_a = (H_wH_s)^{1/2}/16\pi \approx 0.2\ k_BT$ (where $H_w = 3.7\cdot10^{-20}$ J for water[9], $H_s = 6.5\cdot10^{-20}$ J for the glass substrate). The effective Hamaker constant is expressed as

$$H_{eff} = H_{dry} f + \rho \cdot f' \cdot H_{wet} \qquad [4.5]$$

where H_{wet} and H_{dry} are the Hamaker constants with and without a monolayer of water. A tacit assumption inherent in equation [4.5] is that H_{dry} does not depend on humidity. The total adhesion force F_{CH} due to the change in H is now given by:

$$F_{CH}(h,\theta) = F_{dry}\left[1+\rho\cdot g(\theta)\cdot\frac{H_{wet}}{H_{dry}}\right] \approx F_{dry}\left[1+1.22h\cdot g(\theta)\cdot\sqrt{\frac{H_w}{H_s}}\right] \qquad [4.6]$$

where $g(\theta)$ is the fitting function. F_{dry} is the adhesion force of a spatula for vanishing humidity, which amounts to about 7 nN for the glass substrate (Figure 4.2). In equation [4.6] the combining rules given in reference[9] were used for defining H_{wet} and H_{dry}. By setting $g(\theta) = -0.0375\cdot\theta + 3.375$ (where θ is given in deg and $g(\theta = 58°) = 1.2$ in particular for the glass substrate) we obtain the linear lines for F_{CH} in Figure 4.8. The curves show good agreement with the experimental data. The lower increase for N-phob can be qualitatively explained by smaller adsorption energy, resulting in reduced water coverage ρ. The remarkable drop in adhesion in the presence of water is not predictable by this model but the qualitative explanations described in chapter 4.4.1 are still valid.

4.4.3 Comparison of the two models

Both theories are based on the assumption that the amount of adsorbed monolayers of water between spatula and substrate critically depends on air humidity and substrate hydrophilicity. The mathematical descriptions of this concept however were fundamentally different. In the first case the nanobridges were described by a standard capillarity equation. In contrast to this the second model used a purely molecular approach computing only a short-range substrate interaction. To answer which of the two assumed forces is stronger, or in other words, to clarify which model requires larger amounts of water to explain the observed phenomena we compare the two models in the following by focusing on ~56 % relative humidity (Figure 4.2).

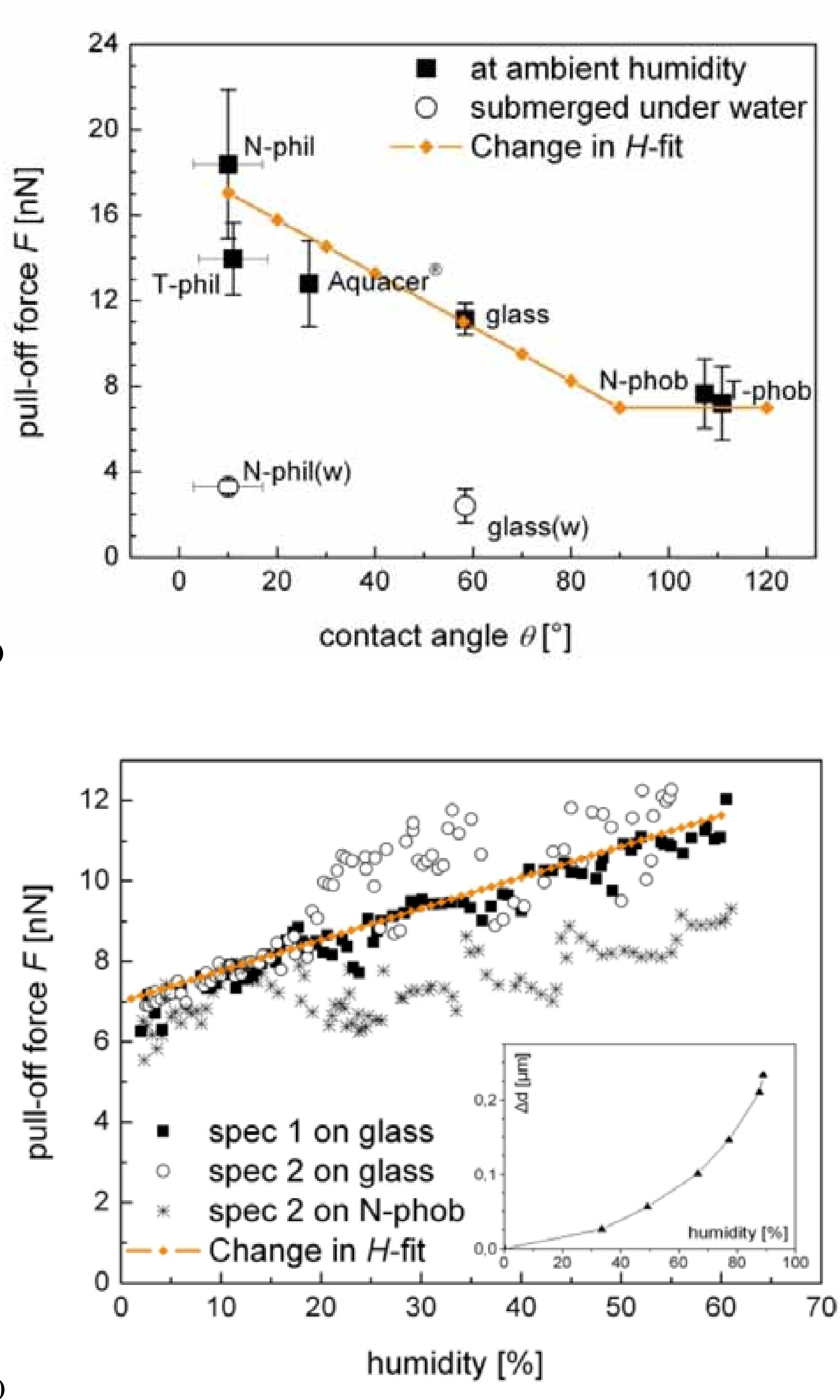

a)

b)

Figure 4.8 Fitting curves according to equation [4.6] which are showing good agreement of the “change in *H* model” with the experimental data of Figure 4.1 and Figure 4.2.

At that value the first model assumes the presence of nine circular nanobridges with a radius of 1 nm resulting in a water-covered area of ~10^{-17} m^2 corresponding to ~0.1 % of the whole spatular contact area. To approximate the terminal element, a circle of radius 100 nm was assumed, which is a typical spatula dimension. In the second model a water covered areal fraction $f' \approx 10^{-14}$ m^2 was needed to reach the corresponding adhesion force (details of the calculation are given in the appendix). This value is three orders of magnitude larger than for the nanobridge model. Thus the corresponding interaction was much weaker. In fact this value corresponds to water coverage of the spatula of ~45 % which means that almost half of the hydrophobic terminal element was assumed to be in contact with the glass cover slip through a complete monolayer of water. Keeping in mind recent work[114] which revealed that only tiniest nucleation spots support the condensation of water on a hydrophobic material like the gecko spatula, this value seems to be large especially if the argument is turned around. Assuming that half of the spatula is wettable at ~60 % relative humidity, it would be impossible to further exclude the presence of a classical capillary bridge between substrate and terminal element at very high relative humidities (> 90 %), which in turn would lead to the collapse of the second model. In fact we do not know the exact number of adsorbed monolayers of water, neither on the spatula nor on the substrates, since we only measured the increase in water film thickness on the N-phil wafer. The result of the ellipsometrical measurement led to the conservative estimate that spatula and substrate are in contact through only one monolayer of water. Table 4.1 presents a comparison of both models:

Model	Water coverage	Interaction strength
Nanobridge	~0.1 %	strong
Change in H	~45 %	weak

Table 4.1 Both models are compared regarding the percentage of the water covered area fraction comparatively to the total contact area of a typical spatula and the corresponding interaction strength.

Although the models are in good agreement with the experimental data, the following paragraph is dedicated to a critical analysis. Both theories need a fitting function ($N(h)$ and $g(\theta)$, respectively) and cannot explain the transition to 100 % relative humidity. In fact, the vdW contribution F_{dry} for the dry spatula, which amounts to about 7 nN for the glass substrate as well as for the T and N-phob wafers, is not constant as assumed for both models. Effectively F_{dry} could decrease with relative humidity as the Hamaker constant H_{dry} does which is one of the reasons why the reduced adhesion force of the submerged spatula could only be qualitatively explained in chapter 4.4.1. This potential shortcoming could be corrected by adapting the Hamaker constant for dry adhesion. Additionally both approaches do not account for the small increase in adhesion force for the N-phob substrate ($\theta > 90°$) in Figure 4.6 b) and Figure 4.8 b) respectively. Only the second model could qualitatively explain the trend by assuming smaller adsorption energy, resulting in a reduced water coverage ρ. Furthermore the nanobridge model assumes the validity of a curvature argument. Of course this tacit assumption would reasonably correspond to the experiment only if larger amounts of water i.e. classical capillary bridges were present. Thus, the description of the attractive interaction due to the presence of nanobridges by macroscopic capillarity is only justified by the good agreement of the model with the experimental data.

4.5 Summary

This chapter demonstrated that the presence of water remarkably influences gecko adhesion on the spatular level. Its relative contribution depended on air humidity and substrate hydrophilicity. The pull-off forces were proportional to the humidity inside an air tight container and increased with decreasing water droplet contact angle of the wafer. Due to the judicious choice and modification of the substrates the investigation presented here allowed to separate the effects of short-range forces from those of long-range interactions. Substrates exerted either identical short-range but different long-range forces or different short-range but similar long-range interactions. The measured adhesion properties could be explained, at least semi-quantitatively, by considering (a) capillary forces due to nanobridges or (b) a change of the effective short-range substrate interaction. However, both models could not explain the transition to 100 % relative humidity (the whole experimental setup completely submerged in water). The detachment force in the presence of water was six times smaller than for the same experiment at ambient humidity and was independent of the substrate water droplet contact angle. This remarkable drop in force was qualitatively explained by the disappearing of the nanobridges, by the presence of an electrical double layer, and by the remarkable reduction of the Hamaker constant H_{dry} due to the high permittivity of water. As a consequence the adhesion force of a whole gecko foot should also be reduced when completely immersed in water, which seems to be in agreement with observations of geckos running on extremely wet surfaces.

The implications of these findings have potentially high relevance in biology and in engineering: studies of bioadhesive mechanisms must account for the possible influence of humidity; and capillary effects should also be optimized in the biomimetic design of artificial attachment systems.

5 Influence of Surface Roughness on Gecko Adhesion

5.1 Introduction

Observations on different insects walking on surfaces with well defined varying surface roughness[119, 120] suggest that the substrate smoothness plays an important role in gecko adhesion. Keeping in mind that adhesion has two faces as explained in chapter 1, it is obvious that the strength of the intermolecular forces must strongly depend on the surface topography. In fact two competitive procedures have to be considered when studying adhesion of an elastic body to rough substrates: (a) the attractive adhesion energy and (b) the repulsive elastic energy due to the contact formation. The influence of roughness on the adhesion between two elastic bodies has been in the focus of scientists for several decades[12-14, 121, 122] and has also been investigated in biological systems[123]. Recently Peressadko *et al.*[124] reported experiments with rubber balls against hard rough substrates. They showed that the effective pull-off force can be accurately calculated from the surface roughness power spectra obtained from the measured surface height profile. However, to date it is still not clear what kind of substrate roughness is critical for the gecko attachment system, and how the adhesion force is related to the interplay of the spatula dimensions with the surface roughness.

5.2 Experimental

All experiments described in this chapter were performed at ambient temperature and humidity (25 °C and 45 % humidity). The experimental force measurement setup as well as the specimen preparation technique was the same as described in chapters 3 and 4 respectively. The substrates investigated were identical with those used in the work of Peressadko *et al.*[124] who provided full details of the surface preparation and analysis. In brief the surfaces were produced by vacuum evaporation of aluminum on a silicon wafer at different substrate temperatures. Polyvinylsiloxane replicas were prepared from the rough aluminum covered surfaces. Samples for the AFM experiment were prepared from the polyvinylsiloxane templates using epoxy resin. The nine different surfaces were denoted by numbers (from 1 to 9) according to increasing root-mean-square (RMS) roughness. Figure 5.1 shows the surface topography of three substrates as imaged by AFM in contact mode. For comparison the scan size (10 µm x 10 µm) and height range (dark: 0 nm and bright: 580 nm) were kept constant. As can be easily seen the surface roughness increases from the left to the right.

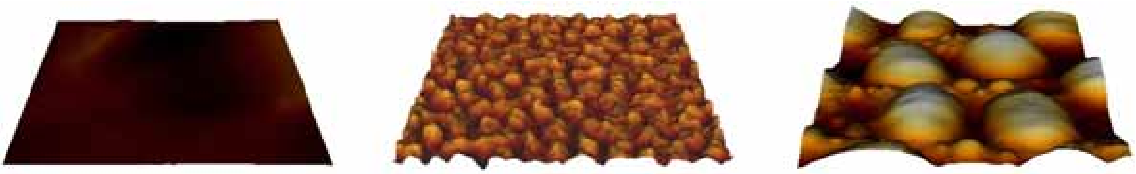

Figure 5.1 The 3D height profile (10 µm x 10 µm, z-range: 0 nm [dark] - 580 nm [bright]) of surfaces 1, 5, and 9 as measured by AFM in contact mode.

5.3 Results

Spatular adhesion forces for two different specimens at ambient conditions on nine different surfaces having RMS roughness values ranging from ~20 nm up to ~3 µm are presented in Figure 5.2. The pull-off forces show a distinctive minimum between 100 nm and 300 nm RMS roughness. Each data point is a mean value of ten measurements at one randomly chosen place on the corresponding surface. This procedure resulted in a total number of 150 measurements for the two different specimens. The cantilever represented by the black squares in Figure 5.2 broke down after testing surface number six (RMS roughness of ~200 nm). Therefore a second specimen (red open squares) glued to a new contact mode cantilever was measured on all nine surfaces.

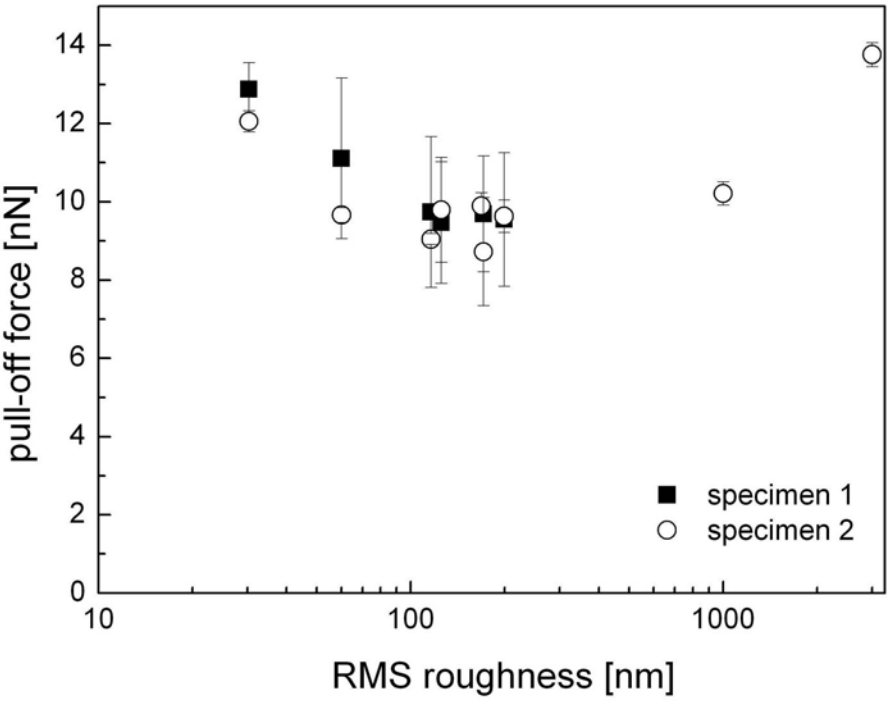

Figure 5.2 Pull-off forces of two different specimens (black and open data points) as a function of the epoxy resin RMS roughness (logarithmical scale). The error bars result from 10 measurements at one randomly chosen location on the corresponding substrate.

5.4 Discussion

The ability of geckos to adhere well to substrates with various degrees of unevenness is directly opposed to what is observable for a smooth bulk material where the pull-off force monotonically decreases with increasing surface roughness. However the results found for single spatulae can be qualitatively explained by simple considerations. In the following discussion the spatular contact area is approximated to be a circle of 200 nm diameter, which nearly corresponds to the real geometry of the natural terminal element. If RMS roughness was smaller than 200 nm, the spatula could adapt well to the very smooth surface and the hair was close enough to the surface for attractive molecular interactions (Figure 5.3 a). This became possible because the plate (~11 nm thick, compare chapter 3) was thin enough to bend and to follow the flat substrate topography. As the gecko exhibits a 'dry' adhesion system i.e. it functions without any secretion (in contrast to flies, beetles or other insects), no liquid substance could 'smoothen' the present topography besides ubiquitous monolayers of water which are present as a thin film on every terrestrial surface (chapter 4).

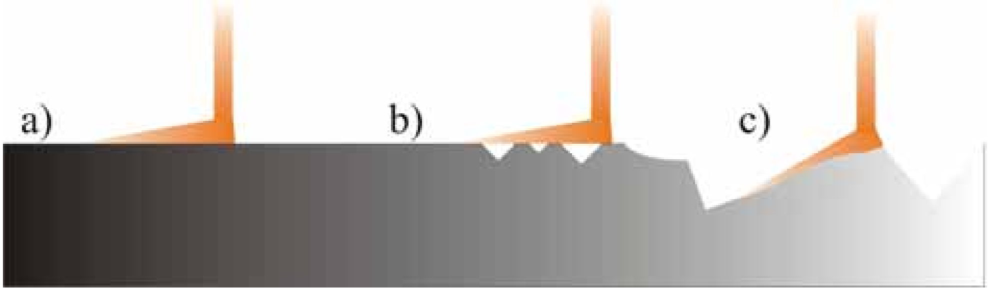

Figure 5.3 Schematical explanation of the experimental results for different RMS roughness. a) On smooth surfaces the spatula can adapt very well. b) On the critical roughness only a partial contact formation is achieved. c) On very rough substrates the spatula is able to contact perfectly the surface again.

However increased surface roughness can also enhance adhesion. For industrial bonding techniques it is known for example that the technical surfaces are sandblast in order to remove contamination and to increase the potential contact area for the glue. Similarly in echinoderms it was reported that adhesion of their tube feet was stronger on rough substrata than on smooth ones[125] due to a larger contact area.

In this study no secret or liquid filled the gaps and smoothed the surface when the RMS roughness was in the critical range of the lateral spatula dimension. Thus it is likely that an imprecise contact formation led to the reduced pull-off forces (Figure 5.3b). Hence a distinctive minimum of the adhesive force was found because the area of true contact was smaller on these substrates compared to the smoother surfaces. In fact, this has been predicted by Persson and Gorb[123] for the adhesion of lizards on sandpaper surfaces. From a theoretical point of view, they expected the same qualitative characteristics for the adhesive force as represented in Figure 5.2.

In cases where the RMS roughness was much bigger than 200 nm the spatula could perfectly adapt and adhere again to the substrates but this time on top of single roughness asperities, which were widely separated and thus appeared to be plane from the spatular point of view (Figure 5.3 c). *A priori* this effect could be astonishing since bulk material would never exhibit such a characteristic. AFM measurements revealed the extreme flatness of the terminal elements and as a consequence thereof a high adaptability of the spatula could be expected (chapter 3.3). However the critical roughness value for good adaptability seemed to correspond mainly to the lateral dimensions of the spatula. Knowing that the gecko adhesion is sensitive to surface topography, the high safety factor as calculated in chapter 3 can be understood much better. As the spatular adhesive force is remarkably reduced on certain substrates, it is of vital importance for geckos to have an over-redundant attachment system.

The experimental results for single spatulae are confirmed by macroscopical observations of living geckos[126]. The animals could perfectly adhere to either very smooth or rough surfaces but had great difficulty to stick to substrates with RMS roughness of ~300 nm. Peressadko and Gorb[120] measured friction forces of *Musca* *domestica* and *Gastrophysa viridula* on substrates with different surface roughness (particle size). The results are presented in Figure 5.4 and show also a minimum for substrates with 0.3 µm particle size. Even if the particle size does not correspond exactly to the RMS roughness these results suggest the existence of a critical surface roughness range for animal adhesion which is consistent with the results of this study.

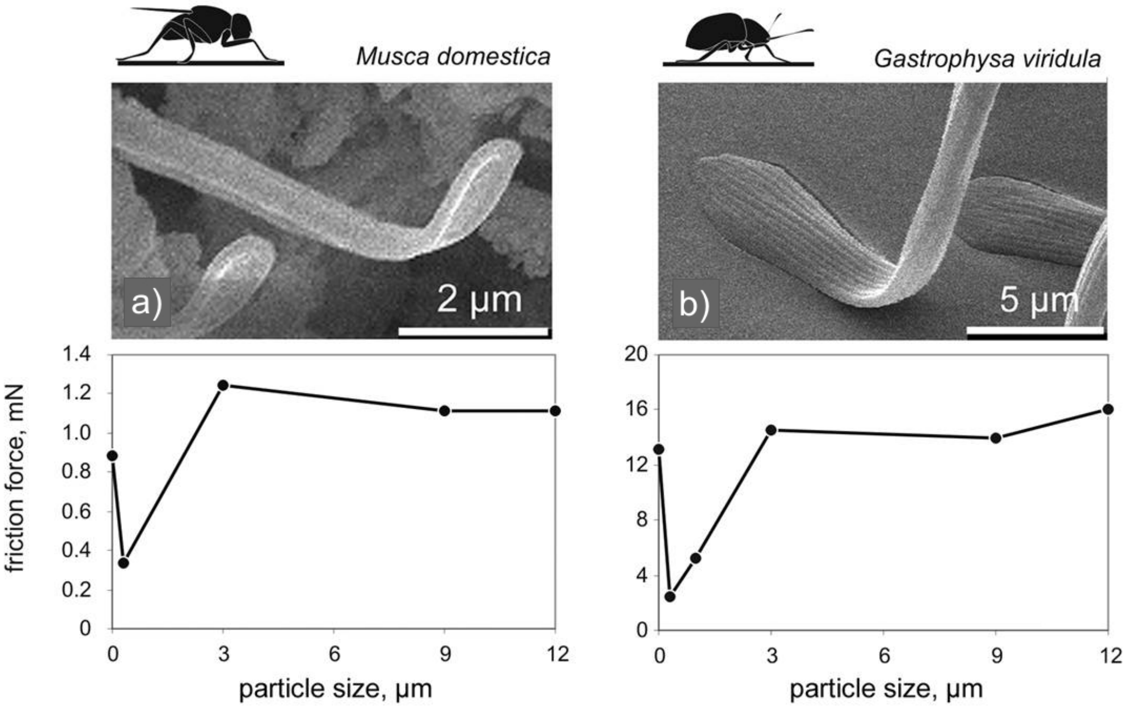

Figure 5.4 Friction forces of a) *Musca domestica* and b) *Gastrophysa viridula* on substrates with different surface roughness (particle size) as measured by Peressadko and Gorb[120] [Courtesy of S. Gorb].

5.5 Summary

This chapter described the influence of nine different levels of substrate roughness on the spatular adhesion force. In contrast to classical experiments, where the adhesion force monotonically decreases with increasing surface roughness, our measurements showed that the spatular adhesive force is remarkably reduced at a critical RMS roughness of about 150 nm similar to previous reports of flies and beetles[120]. The roughness values corresponding to the minimal adhesive forces were found to correlate with the lateral dimension of a single gecko spatula. Above the critical surface roughness the pull-off forces increased again with increasing RMS roughness. The experimental data could be qualitatively explained and were supported by observations on living geckos[126]. Comparable with our experiments on the spatular level, the animals had also great difficulties to adhere to surfaces having RMS roughness of 0.3 µm.

6 Mechanical Properties of a Single Gecko Seta

Abstract - Measurements of the mechanical properties of a single gecko seta are presented. The hairs were mechanically tested in three ways: (a) *in situ* tensile tests where the specimens were prepared by means of a focused ion beam microscope and were loaded by a piezo force transducer combined with a micromanipulator, (b) three-point bending experiments using atomic force microscopy for detection of the setal bending stiffness, and (c) nanoindentation tests of single setae. Young's modulus was obtained (a) from the slope of the stress-strain curves, (b) from the slope of the deflection loops measured by atomic force microscopy, and (c) by analyzing classically[127] the nanoindentation unloading curves. The results were twofold: probably due to the different moisture contents and due to the anisotropy of the biological composite material (longitudinal aligned keratinous fibers embedded in a softer matrix), the tensile stiffness, when tested under ultra high vacuum parallel to the direction of the fibers, was found to be ~4 times higher than for both the bending stiffness and the nanoindentation tests perpendicular to the fibers at ambient conditions, where Young's modulus was found to be in the range of 1.5 GPa.

6.1 Introduction

So far the whole work dealt mainly with adhesion related experiments. To provide a more general view of the whole attachment system it is necessary to learn more about the mechanical properties of a single seta since this gecko hair provides the spatular support. In chapter 3 a method was presented to measure the adhesion forces of a single spatula[95, 96] but the mechanical properties, and in particular Young's modulus, of a single seta have not been reported to date. This knowledge is a key factor in understanding the natural adhesion mechanism and represents an important input parameter for the adhesion design maps[90], which can guide the biomimetic design of dry adhesives. Nanoscale bending tests using atomic force microscopy were performed already successfully on different classes of materials e.g. single crystal silicon, metals and polymers[128-131]. Here the first measurements of keratinous gecko setae will be presented.

6.2 Experimental

The hairs were tested in tension following the method of Orso *et al.*[132, 133]. After specimen preparation in a focused ion beam microscope tensile forces were applied inside the UHV chamber through the micro manipulator MM3A (Kleindiek Nanotechnik GmbH, Reutlingen, Germany) which supported an AFM tip combined with a piezo force transducer (Nascatec GmbH, Kassel, Germany). Additionally three-point bending tests were carried out using AFM. Complementary nanoindentation tests of five different gecko setae were performed using a commercially available nanoindentation system (Nanoindenter XP, MTS, Eden Prairie, USA). In these tests the hairs were glued down on a glass cover slip before testing to guarantee a fix position during indentation using a Berkovich tip. Full details of the tensile test using a piezoresistive cantilever beam mounted on the Micro Manipulator MM3A are given in references[132, 133]. In brief a single gecko seta was broken in deep frozen conditions from a non-moulting gecko foot and fixed between the cantilever beam and a metal block by means of the FIB tungsten deposition facility (Figure 6.1 a).

Subsequently an *in situ* tensile test was performed in which the applied forces were measured and the displacement was controlled by simultaneous imaging the specimen. The cross sectional area was measured after seta fracture. The longitudinal Young's modulus E_l was determined from the slope of the measured stress-strain curve.

The bending stiffness E_b of the gecko setae was measured with the atomic force microscope operating with a 100 µm scanner. The experiment required controlled variation of air humidity. Therefore the entire AFM was placed in an air tight container. Inside this box the humidity level was adjusted by varying the flow rate of dry nitrogen and was continuously monitored by a commercially available hygrometer (testo 177-H1, Testo AG, Lenzkirch, Germany). Standard non-contact mode cantilevers (NST-NCHF, Nascatec GmbH, Kassel, Germany) with high spring constants *c* were used after a careful spring constant calibration[134] by measuring its exact beam geometry using high resolution scanning electron microscopy (SEM: LEO 1530 VP, Carl Zeiss SMT Ltd., Cambridge, U.K.). Typically values of ~70 N/m were obtained for a Young's modulus of 168 GPa as declared by the cantilever manufacturer. To provide the desired experimental configuration a ~3 µm deep trench was cut into a Si-wafer (SilChem Handelsgesellschaft GmbH, Freiberg, Germany) by means of the FIB (Figure 6.1 b).

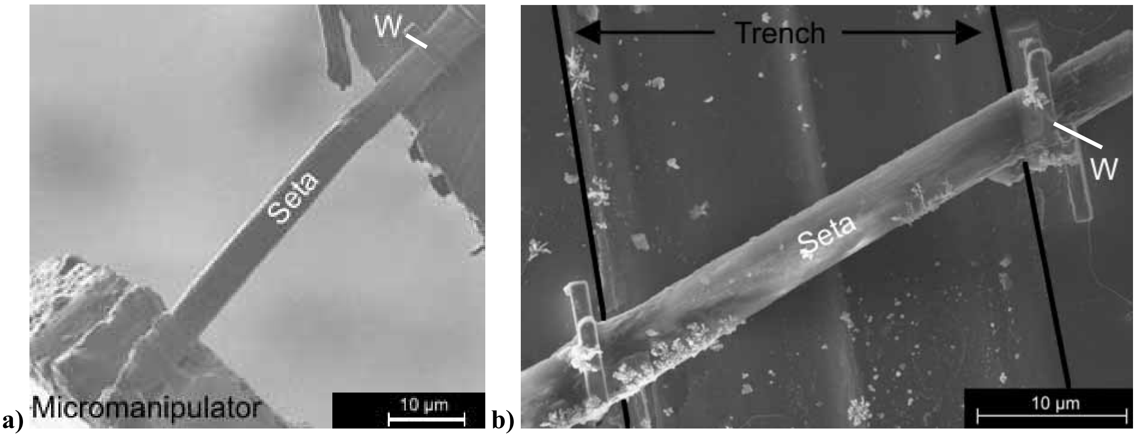

Figure 6.1 A single seta is fixed by FIB deposited tungsten stripes a) between a metal block and the cantilever beam and b) bridging the gap of a ~3 µm deep trench.

Additionally a single seta was sheared off a non-moulting deep frozen gecko foot (*Gekko gecko*) with the aid of a needle tip. Using a binocular microscope the isolated seta was then positioned above the trench and brought into the FIB microscope. Subsequently the tungsten deposition facility was used to fix the seta at the sharp corners of the trench to prevent any lift-off during the bending test (Figure 6.1 b). Next the specimen was mounted in the AFM stage. Here at first, the calibrated cantilever with known beam stiffness c was deflected against the rigid Si-wafer surface to determine its deflection sensitivity, S. In the second step we imaged the specimen in intermittent-contact mode to measure the geometrical positions. Herewith we were able to locate exactly the midpoint along the free-standing length and the cantilever tip was taken there. For that purpose the highly precise AFM positioning facility working with a hardware linearization in all three axes also for closed loop measurements was used. The third step consisted of deflecting the cantilever exactly at this midpoint against the seta and measuring their combined deflection sensitivity[135], S_c, which is linearly related to their combined stiffness, c_c. Thus the experimental setup corresponded to the mechanical model of two springs (cantilever and seta) connected in series:

$$\frac{1}{c_c} = \frac{1}{c} + \frac{1}{c_S} \qquad [6.1]$$

where c_S is the unknown setal bending stiffness, c is the known cantilever stiffness and c_c is the measured combined stiffness. To calculate the elastic modulus in this three-point bending study we used the clamped-beam model, which is valid for our experimental setup. The reduced bending elastic modulus E_b is then given by the following relationship:

$$E_b = c_S \frac{L^3}{192I} \qquad [6.2]$$

where L is the length between the two clamping tungsten stripes, the factor 192 results from the clamped-beam model and $I = (\pi r^4)/4$ is the setal moment of inertia. The setal length $L \approx 40$ µm and radius $r \approx 1.7$ µm were analyzed afterwards by means of SEM and FIB. For the determination of r we cut the specimen in half by means of the milling facility of the FIB microscope. The exact cross sectional area was measured and approximated by πr^2. Typical values of the measurements that we used to calculate the setal bending stiffness were $S \approx 21$ V/µm, $S_c \approx 16$ V/µm.

To perform nanoindentation tests on a single gecko seta, first the hair was glued (superglue, Loctite Deutschland GmbH, München, Germany) on one side to a glass cover slip (Menzel Glasbearbeitungswerk GmbH & Co. KG, Braunschweig, Germany). In this way any movement during the scanning procedure, which took place before indentation, was avoided. By means of the NanoVision™ extension a three dimensional map of the sample geometry was obtained. Subsequently the seta was traversed under the indenter tip. Similar to AFM contact mode the hair was scanned by means of the indenter tip. The scan notably increased the indentation placement accuracy (2 nm) compared to the use of optical microscopy (accuracy 0.5 µm). Hardness and indentation modulus were determined using a dynamic depth-sensing indentation mode (CSM). Only one indent was made per seta because only little glue-free space was available for the indenter tip at the free end of the hair. Thus the scatter range was mainly due to the natural differences of the five setae.

For transmission electron microscopy (TEM), gecko lamellae were peeled off the fresh specimens, fixed for 12 h at 4 °C in 2.5 % glutaraldehyde (in 0.01 M phosphate buffer at pH 7.3) and post-fixed for 1 h in 1 % osmium tetroxide in phosphate buffer at 2 °C. After washing, the preparations were stained for 1 h at 4 °C in 0.1 % aqueous uranyl-acetate solution, washed, dehydrated, and embedded in a low-viscosity resin[136]. Ultra-thin sections were picked up on copper grid slots coated with formvar film, contrasted with uranyl acetate and lead citrate, and observed in TEM Philips CM10[67]. Semi-thin sections stained with Toluidine Blue were also made.

6.3 Results

6.3.1 *In situ* tensile test and nanoindentation

In situ tensile tests with three different setae (cross-sectional areas were 11.8 μm^2, 12.8 μm^2 and 12.2 μm^2 respectively; initial clamping length ~50 µm) were performed in ~50 steps. The force increments remained almost identical during the test. After specimen preparation roughly 15 minutes were needed to perform a complete tensile test until fracture. As shown in Figure 6.2 a) all setae could support stresses larger than 60 MPa and were strained to values larger than 1.5 %. The setal deformation behavior was roughly linear-elastic up to 0.5 %. In fact, the fracture stress was found to vary between ~63 and ~114 MPa. In a classical stress-strain diagram Young's modulus corresponds to the slope of the curves in the elastic regime as marked by the dotted ellipse in Figure 6.2 a). Here the longitudinal modulus E_l was found to be 6.8 ± 1.7 GPa for a single seta under uniaxial stress. Beyond this elastic regime the data scattered remarkably for the different specimens, which is not surprising for biological materials.

Additionally the setal indentation modulus was determined in five experiments as shown in Figure 6.2 b). Up to 100 nm penetration depth a plateau became visible with mean values at ~1.2 GPa. The constant increase in modulus at larger penetration depths (> 100 nm) is very likely due to the influence of the hard glass cover slip that was used as a substrate. Pushing the indenter tip deeper into the sample therefore resulted in a measurement of the combined stiffness of the seta and the hard glass substrate. This confirms that the plateau value of 1.2 GPa reflects only the setal materials properties.

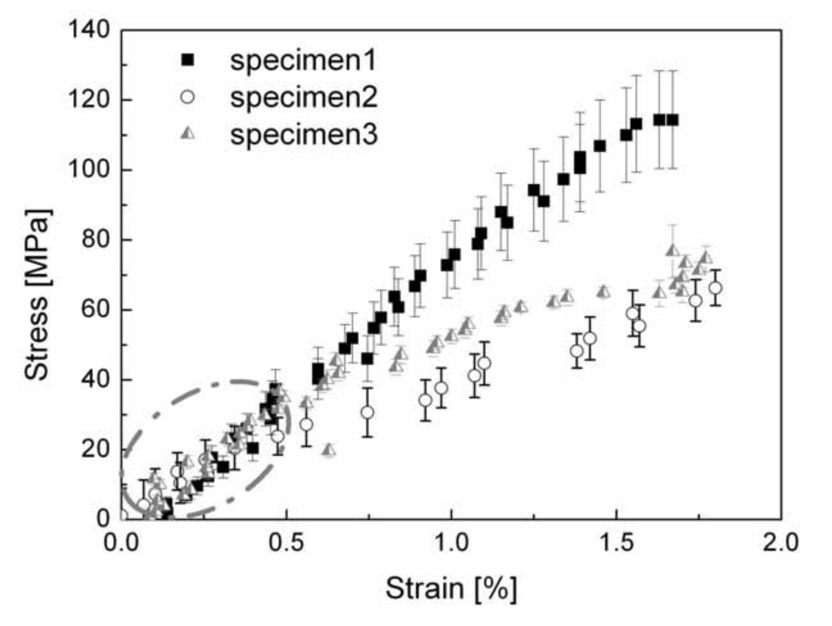

a)

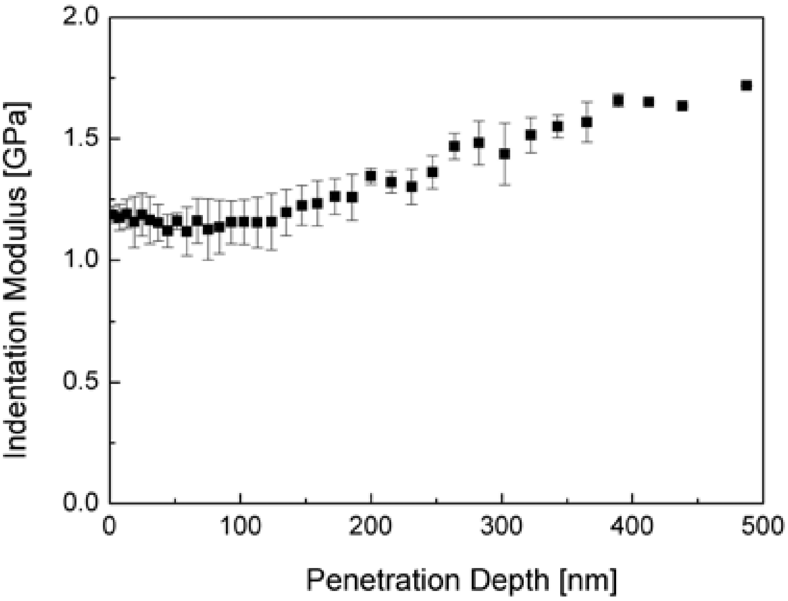

b)

Figure 6.2 Results of the *in situ* tensile test and of the nanoindentation: a) Stress-strain curves of three different tensile-tested gecko setae: Young's modulus corresponds to the slope of the curves as marked in the elastic regime and was found to be 6.8 ± 1.7 GPa for a single seta under uniaxial stress. b) Setal indentation modulus showing a plateau up to 100 nm tip indentation depth and a linear increase due to influence of the hard glass cover slip that was used as a substrate. The indentation modulus is found to be ~1.2 GPa.

6.3.2 AFM three-point bending

The bending stiffness was determined from the deflection loops as shown in Figure 6.3 a). Both the deflection stiffness of both springs connected in series and the pure cantilever stiffness when pushed against the rigid Si wafer surface were measured as a function of air humidity. The coincidence and linearity of the approach and retraction curves proves that the setal deformation behavior is linear and elastic in the applied force regime (Figure 6.3 a). In total ~1000 single measurements on two different setae were performed. Combined with the geometrical data of the setae (length and radius) and the cantilever stiffness the reduced Young's modulus was calculated according to equation [6.2] and is displayed as a function of air humidity in Figure 6.3 b). Specimen 1 (square data points) was tested on three different days as indicated by the indices. A mean value of ~1.7 ± 0.6 GPa was found independent of air humidity.

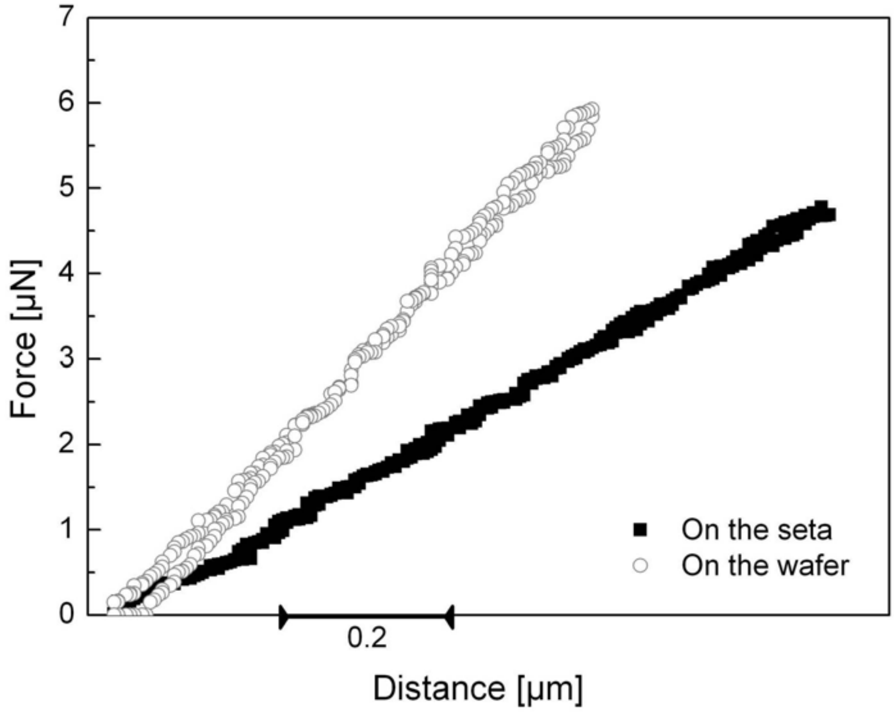

a)

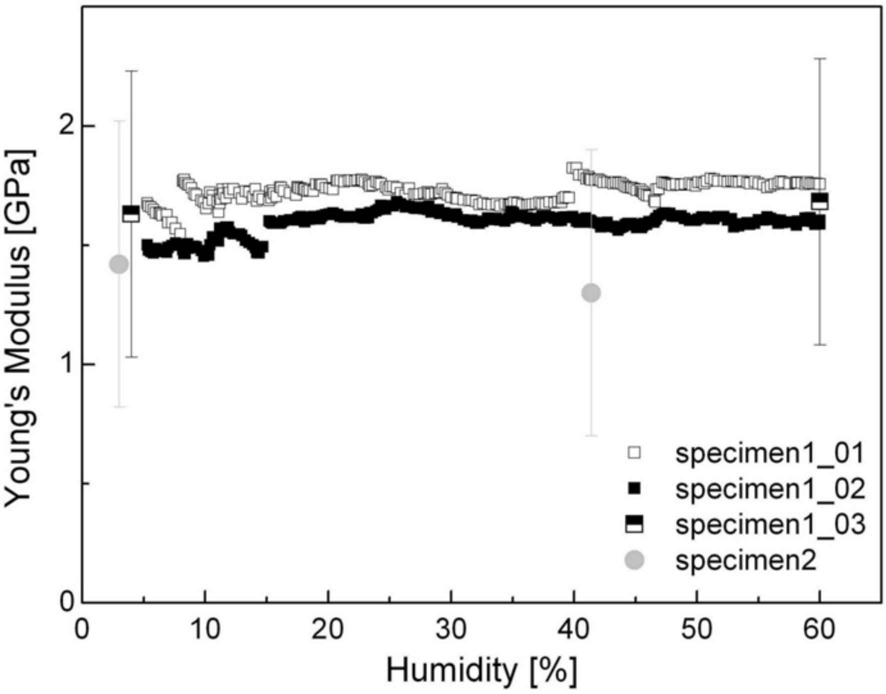

b)

Figure 6.3 Three-point bending with the AFM: a) Typical force *vs.* distance loops when the cantilever tip was pushed against the seta or against the rigid Si-wafer surface: Young's modulus corresponds to the slope of the black and was found to be ~1.7 ± 0.6 GPa for a single seta. b) Bending Young's modulus as a function of air humidity. The law of error propagation was used for equations [6.1]-[6.2] to calculate the error bars. In total ~1000 single measurements for two different specimens were performed. Specimen 1 was tested on three different days indicated by the indices.

Additionally the cross section of a single seta was imaged in a TEM (Figure 6.4). Dark-contrasted fibers were found embedded in a brighter-contrasted matrix. The fibers show roughly the same contrast as the rigid outer skin since both materials similarly diffract electrons due to their similar properties. The mean volume fraction of the two phases was determined by analyzing an ultra thin cross section as visualized in the transmission electron micrograph. For that purpose we used commercially available image analysis software (SigmaScan Pro, Image Analysis 5.0, SYSTAT Software Inc., Chicago, USA). The volume fraction f_1 of the dark fibers was found to be 68.8 ± 4 %, and the brighter matrix volume fraction f_2 amounted to 31.2 ± 4 %.

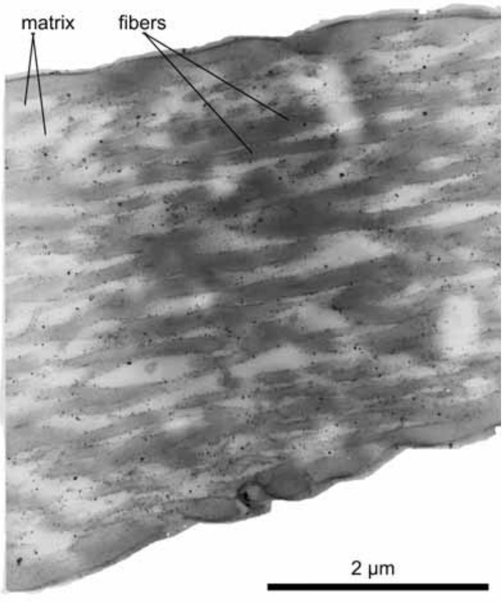

Figure 6.4 Longitudinal ultra thin cross section of a single seta exhibiting electron dense keratinous fibers embedded in a brighter matrix, transmission electron micrograph [Courtesy of S. Gorb].

6.4 Discussion

In this study we have presented three methods to determine the mechanical properties of a single gecko seta. The *in situ* tensile tests revealed a roughly linear behavior up to 0.5 % strain. No pull-out effect of the fibers was observed and the fractured surfaces were always perpendicular to the loading direction, which characterizes a relatively brittle material. A Young's modulus of ~6.8 GPa was measured in the tensile tests which is almost six times higher than the value found in the nanoindentation tests (~1.2 GPa). The three-point bending study revealed a bending stiffness of the hair of ~1.7 GPa, which is close to the indentation value. The easiest and fastest method to determine the setal stiffness properties was the nanoindentation study due to the easier experimental procedure. Both the tensile and the bending test techniques had to make use of a time consuming specimen preparation by means of the FIB microscope followed by a non-automated measurement technique.

The gecko seta is a composite material consisting of keratin fibers, which are longitudinally arranged in a matrix (Figure 6.4). Due to the resulting anisotropy and inhomogeneity of the seta its stiffness moduli were different for different loading directions. The anisotropy in stiffness can be quantified as E_b/E_l. Comparing the bending with the tensile stiffness this ratio is equal 0.176 meaning that there is a reduction in stiffness of about 82.4 % if the loading conditions are changed from longitudinal to transversal. Two possible explanations for this large anisotropy are given in the following:

(a) For a fiber composite it is known that the materials behavior depends on the fiber form, packing, and spacing between fibers. Due to the alignment of the keratinous fibers, the seta was able to sustain a bigger stress when loaded in axial direction (*in situ* tensile test) while testing in three-point bending resulted in a smaller bending resistance. This could be explained by a low interfacial bond strength which would lead to shear deformations and thus to an underestimate of the bending compared to the longitudinal stiffness. However the explanation would not hold for the nanoindentation tests, which independently confirmed the range of the measured bending modulus.

(b) The results could also be explained by the influence of the different atmospheric conditions. It is known from a previous work[137] that the stiffness of insect cuticle is five times higher for a dry specimen than for a wet one. Therefore the difference in stiffness might be explained by a difference in the moisture content of the specimen. The highest stiffness was found for the *in situ* tensile tests under UHV conditions. Almost one day was needed to complete the specimen preparation and the test. A much smaller stiffness was found in the three-point bending test where only the specimen preparation was made under UHV conditions (duration < 2 hours). The smallest stiffness was measured in the nanoindentation tests which all took place under ambient conditions as the specimen preparation did. However the three-point bending tests showed that Young's modulus was independent of air humidity (from 2 % up to 60 %). But the gecko seta was shorter exposed to UHV conditions in the bending tests which possibly made a difference compared to the tensile tests.

It is found in literature that mainly the matrix might be taking up water and the fibers are not changing their moisture content[1]. Thus only one third of the volume could be changing and, if present, it was not possible to identify these small effects with our experimental setup. Additionally, before testing, the hairs had been in the vacuum chamber of the FIB microscope and it is well known that once a biological material is dehydrated it furthermore can not absorb the water as well as before. However this independency supports the results presented in chapter 4. One could have argued that the increase in adhesion force with increasing relative humidity results from the enhanced flexibility and adaptability of the spatula and is not due to capillarity contributions. With the results presented here it becomes clear that the measured effect was real and not due to a change in setal stiffness.

Additionally it is instructive to compare the mechanical properties of keratinous gecko setae to other natural materials. The tensile strength *vs.* Young's Modulus is displayed in Figure 6.5 for different biomaterials and additionally the results of earlier data[133] where the stiffness of a single beetle seta (*Gastrophysa viridula*) was measured are included. For Young's moduli in the range of 1.2 GPa to 6.8 GPa only spider silk and some insect cuticle specimens are found to have a higher tensile strength than keratinous gecko seta. The straight line of slope 1 represents a constant elastic strain and describes how large a deformation is possible without failure. Materials on the line have the same performance as the beetle seta. Materials above it in the white area (e.g. the gecko seta) allow a larger deformation before fracture than those below the line (grey area). In this sense it is true that wood, carbon fibers or even the frequently investigated carbon nano-tubes exhibit a worse behavior than the gecko seta.

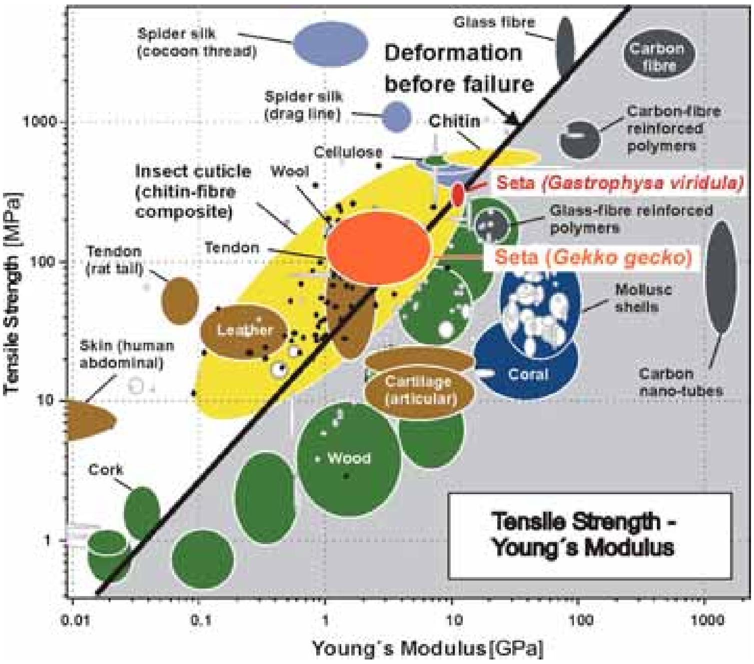

Figure 6.5 The tensile strength *vs.* Young's modulus is displayed for different materials. Figure was created using the nature materials selector[138] and was adapted from reference[133]. The straight line of slope 1 represents a constant elastic strain and describes how large a deformation is possible without failure. Materials on the line have the same performance as the beetle seta. Materials above it in the white area (e.g. the gecko seta) allow a larger deformation before fracture than those below the line (grey area).

It is also instructive to compare the results to contact mechanical predictions using the adhesion design maps of Spolenak, Gorb and Arzt[90]. Full details of the concept are given in reference[90]. In summary they modeled the limits of contacts imposed by fiber strength, fiber condensation, compliance, and ideal contact strength. Approximating the tip of the spatula by a sphere, assuming the work of adhesion $\gamma = 0.05$ J/m^2 (eq. [3.2]), an area fraction of fibers $f = 50$ %, a length of surface interaction $d = 0.2$ nm, and an effective Young's Modulus $E^* = 1$ MPa, we obtain the adhesion map as presented in Figure 6.6. The criteria for fiber fracture (blue line) and ideal contact strength (red line) are indicated. The black lines are contours of equal apparent contact strength.

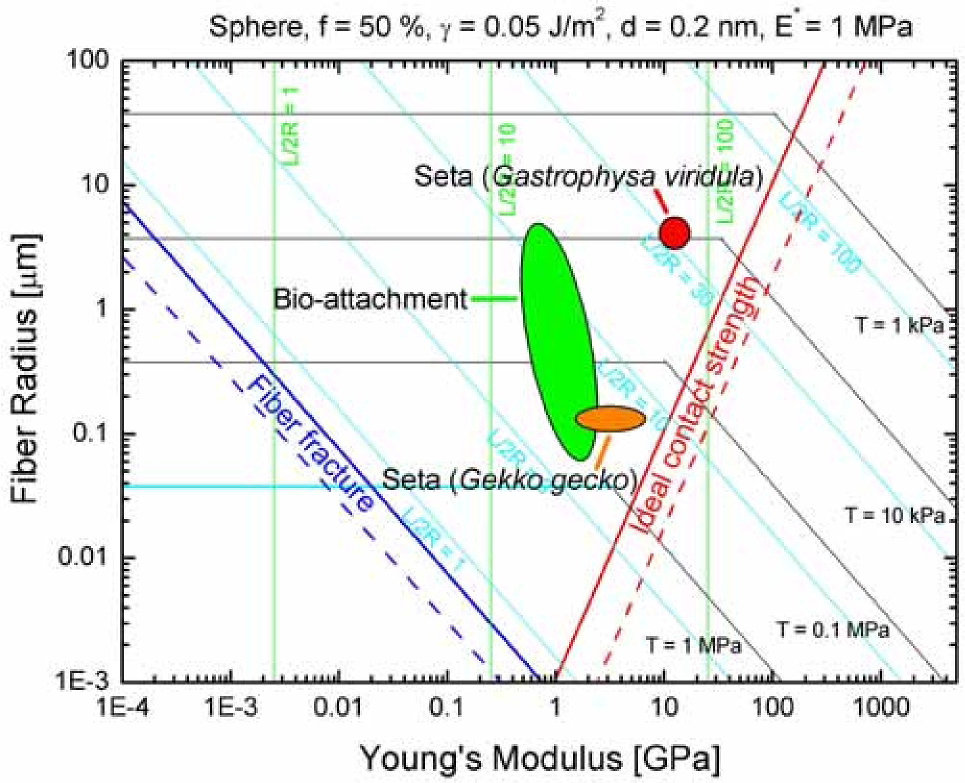

Figure 6.6 Adhesion design map[90] for spherical tip shape. The following parameters are assumed: $\gamma = 0.05$ J/m², $f = 50$ %, $d = 0.2$ nm and $E^* = 1$ MPa. The criteria for fiber fracture (blue line) and ideal contact strength (red line) are indicated. The black lines are contours of equal apparent contact strength.

Our experimental data (orange region) is close to an earlier estimate[90] for biological contact systems (green region). Additionally Vincent and Bonser *et al.*[139-141] showed that the elastic modulus of feather β-keratin was found to be in the range of 1 to 10 GPa; which is also of the same order of magnitude as in our experiments.

However for human hairs Goldsmith and Baden[142] found a decrease in Young's modulus from 11.7 GPa down to 8.8 GPa (same order of magnitude as in our experiments) when they increased the air humidity from 6 % to 53 % at a constant temperature of 23 °C. We could not find the same trend in our bending experiments but our data deals with keratinous material of geckos which of course is different from human hairs (beta *vs*. alpha keratin). The disagreement might also be explained by the effect mentioned above, that once a biological material was dehydrated the moisture content cannot be remarkably increased anymore. Since the human hair of their study had never been under low pressure conditions, the cavities probably remained intact leading to the humidity dependent stiffness they observed.

6.5 Summary

We presented the first stiffness measurements of a single gecko seta, which were performed in three different ways: (a) *in situ* tensile tests where the specimens were prepared by means of a focused ion beam microscope and were loaded by a piezo force transducer combined with a micromanipulator, (b) three-point bending experiments using atomic force microscopy for detection of the setal bending stiffness as a function of the relative humidity, and (c) nanoindentation tests of single setae. The tensile stiffness, when tested under ultra high vacuum parallel to the direction of the fibers, was found to be ~4 times higher than for both the bending stiffness and the nanoindentation tests perpendicular to the fibers at ambient conditions, where Young's modulus was found to be in the range of 1.5 GPa. The high anisotropy was explained by hypothesizing both different moisture contents of the seta and possible shear deformations during the bending tests.

7 Summary and Outlook

Attachment mechanisms of animals that can cling to walls and walk on ceilings have drawn a significant amount of scientific and public attention. This is due, on the one hand, to the fascination of natural nanoscale objects and, on the other hand, to the potential technological advances that biomimicry of such attachment structures offers. Applications for dry adhesive systems range from climbing robots and industrial pick-and-place applications to a substitute for sticky tape that can be used repeatedly. In this context, is instructive to investigate the gecko, which is one of the heaviest and best clinging animals. It developed intricate hierarchical hairy structures consisting of toes, lamellae, setae, and spatulae.

At first this work gives the reader a theoretical background of the techniques used and the underlying physical principles. Subsequently experiments using atomic force microscopy are reported in which for the first time force-displacement curves for individual spatulae were recorded. The experiments yielded adhesion forces on glass at ambient conditions, which were reproducibly found to be in the 10 nN range. For this purpose an advanced combination of specimen preparation and force measurement had to be used. The know-how to glue inorganic particles to AFM cantilevers was transferred to biological materials by attaching a single seta to an accurately calibrated cantilever. The number of spatulae at the end of the single seta was subsequently reduced using the milling facility of a focused ion beam microscope. The few single spatulae remaining on the seta could be differentiated in the adhesion force measurements. The pull-off force was measured as a function of various parameters (air humidity, surface hydrophilicity and surface topography). The spatular adhesive force was remarkably influenced by the presence of water: it was possible to show that the pull-off forces were proportional to the varied humidity inside an air tight container. Through judicious choice and modification of the substrates it was found that the force increased with decreasing water droplet contact angle of the used wafer. The data obtained were modeled theoretically to explain the observed adhesion phenomena. Two theories were presented which acted on a similar assumption namely that the amount of adsorbed water strongly depends on air humidity and substrate hydrophilicity. However the corresponding mathematical descriptions were fundamentally different. In the first case a standard capillarity formula was combined with a nanobridge image whereas in the second case a purely molecular approach computing only short-range interactions was chosen.

The pull-off forces were also sensitive to the surface topography. In cases where the RMS roughness was in the critical range of the lateral spatula size, imprecise contact formation led to a distinct minimum of the pull-off forces compared to either smoother or rougher surfaces. This effect was all the more astonishing since AFM measurements revealed the extreme flatness of these final contact elements. However the critical RMS roughness range corresponded to the lateral dimensions of the spatula. To provide a more general view of the whole gecko attachment system it was indispensable to gain knowledge of the mechanical properties of a single seta. The isolated hairs were mechanically tested by means of three methods: (a) *in situ* tensile tests using a micromanipulator inside a focused ion beam microscope, (b) three-point bending tests using atomic force microscopy and (c) nanoindentation. Under tension Young's modulus was found to be ~4 times higher than under bending load or for the nanoindentation tests where the stiffness was found to be in the range of 1.5 GPa.

The results presented in this work shed new light on the nanomechanisms of gecko's attachment and will help in the rational design of artificial bio inspired attachment systems, which can be used repeatedly without any loss of functionality.

In future work it would be worth investigating the interplay of air humidity and surface roughness simultaneously. It would be interesting to find out if the monolayers of water are able to smooth the surface, which would lead to a less distinctive minimum in adhesion force than shown in chapter 5. Additionally it should make a big difference if the angle between seta and substrate deviates from 90 degree. Due to the alignment of the spatulae it should be possible to find an optimum angle under which the adhesion forces are maximal. Additionally it could be interesting to compare hairs which had been deeply frozen (like in this work) to freshly prepared setae. In the same sense it would be also worth studying the influence of the moisture content (as discussed in chapter 6) on the setal stiffness and adhesive force. And last but not least a comparison to single spatula forces of other lizards and/or to the single setula force of a spider would also help to put the adhesive force values found for *Gekko gecko* in a broader perspective.

8 Appendix

8.1 Details of the Java script

```
# $Id: s-A0016-1.py,v 1.1 2004/03/02 11:22:13 Detlef Knebel Exp $
#script written for A0016, Gerrit Huber
#for details see script-project "s-A0016-1"

import os, math, time

from java.lang import Double
from java.lang import Integer
from java.lang import Boolean
from java.lang import String
from java.util import ArrayList
from java.util import HashSet
from java.io import File
from com.jpk.util import Data2DFile
from com.jpk.util import Misc
from com.jpk.util import Script
from com.jpk.util import WorkerThread
from com.jpk.spmlib import ApproachedMode
from com.jpk.spmlib import CalibrationSlot
from com.jpk.spmlib import Channel
from com.jpk.spmlib import ChannelRetrace
from com.jpk.spmlib import ForceScan
```

```
from com.jpk.spmlib import ForceScanningEndOption
from com.jpk.spmlib import Grid
from com.jpk.spmlib import ForceFile
from com.jpk.spmlib import PauseTimingSettings
from com.jpk.spmlib import Position
from com.jpk.spmlib import RealTimeSettings
from com.jpk.spmlib import RealTimeScan
from com.jpk.spmlib import RealTimeScanSaveThread
from com.jpk.spmlib import RetractedPiezoMode
from com.jpk.spmlib import SimpleForceSettings
from com.jpk.spmlib import SinglePositionPattern
from com.jpk.spmlib import ClosedLoopForceSettings
from com.jpk.spmlib import SPM
from com.jpk.spmlib import SPMScript
from com.jpk.guilib import LineScanData2D

class Gecko1(SPMScript):
  def __init__(self):
    self.parameters = ArrayList()
    self.parameters.add(Script.TitledValue('length', Double(1e-6)))
    self.parameters.add(Script.TitledValue('pixel', Integer(512)))
    self.parameters.add(Script.TitledValue('filename_root', 'gecko'))
    self.comment="
    self.info = ArrayList()
    self.info.add(Script.TitledValue('comment', self.comment))



  def mode(self):
    return self.getModeProxy()

  def wait(self, text="press Continue"):
    self.info[0].setValue(text)
    self.getParametersFromUser(self.info)

  def run(self):
    output  = self.getWriter()
    self.getParametersFromUser(self.parameters)
    self.length = self.parameters[0].value
```

```
self.pixel = self.parameters[1].value
self.filename_root = self.parameters[2].value
output.println("Start Gecko1")
output.println('length = '+`self.length`)

# Define the Moving-line
# First Point
self.wait("Force-spectroscopy-mode")
self.wait("Select a starting point")
startPosition = self.getModeProxy().getForcePosition()
# Second Point
self.wait('Select another point')
endPosition = self.getModeProxy().getForcePosition()

# Compute and set the scan grid to be used for line scanning:
iLength = self.getModeProxy().getImageGrid().getILength()
xc=(startPosition.x+endPosition.x)/2
yc=(startPosition.y+endPosition.y)/2
xlength=endPosition.x-startPosition.x
ylength=endPosition.y-startPosition.y
ulength=(xlength**2+ylength**2)**0.5
angle=math.atan2(ylength,xlength)
output.println(xc)
output.println(yc)
output.println(ulength)
output.println(angle)
grid = Grid.createGrid(xc, yc, ulength, 1e-9, angle, 0, iLength, 1,)
self.getModeProxy().setImageGrid(grid)
self.getModeProxy().setRetrace(0)
self.getModeProxy().setForceRetrace(1)

# Starting the Action
# Approach
self.piezoApproach()
# Moving
lineScan = self.collectLineScans(1)
# Retract (perpendicular to the plane)
#settings = SimpleForceSettings(1024, 10e-6, 7e-6)
```

```
        startZ = self.getModeProxy().getCurrentValue(Channel.get("strainGaugeHeight"))
        settings = ClosedLoopForceSettings(self.pixel, startZ+self.length, startZ, 0.005, 150)
        self.getModeProxy().setForceSettings(settings)

        #self.wait('Ready for Force-Scan')
        forceScan = self.collectForceScans(1, ForceScanningEndOption.STAY_AT_POSITION)
        self.wait("Ready for Saving")
        self.writeForceScans(forceScan[0])
        self.wait("Finished")
    def writeLineScan(self, lineScan):
        """Save the vertical deflection channel of the linescan to a file.
        The filename is generated from self.filename_root, count, and whether the file is trace or retrace.

        if lineScan.isRetrace():
            direction = 'retrace'
        else:
            direction = 'trace'
        filenameroot = ('%s-%03d-line-%s-' % (self.filename_root, count, direction))
        for channelName in ['vDeflection','height','strainGaugeHeight']:
            channel = Channel.get(channelName)
            data = LineScanData2D.create(lineScan, channel,
                lineScan.getChannel(channel).getCalibrationSet().getDefaultCalibrationSlot(),0)
            Data2DFile(filenameroot+channelName+'.out').write(data)

    def writeForceScans(self, retraceScan):
        """Save the vDeflection, the height and the strainGaugeHeight
        into a force distance file. The filename is generated from self.filename_root, (fast|slow)
        and (trace|retrace)
        """
        filename = ('%s-force.out' %(self.filename_root))
        channelRetraces = HashSet()
        for channelName in ['vDeflection','height','strainGaugeHeight']:
            channel = Channel.get(channelName)
            channelRetraces.add(ChannelRetrace(channel, 1))
        ForceFile().write(
            File(filename), retraceScan, channelRetraces
            )

startScript(Gecko1())
```

8.2 Details of the calculations in chapter 4.4.3

We have two unknown parameters and two equations. The area of one spatula is approximated by a circle with a radius of 100 nm, which is a typical dimension for the terminal element. Equation [8.1] acts on the assumption that the whole spatula is in contact. The areal fraction *f* of the spatula shall be in direct contact with the substrate. The fraction *f'* of the spatula is in contact with the substrate through a monolayer of water. In total the sum of both fractions has to be equal to the whole spatular contact area. The factors 1.2 and 1.22 in equation [8.2] are part of the model itself- the humidity was set to be 0.56:

$$f' + f = \pi \cdot 10^{-14}\,\mathrm{m}^2 \quad [8.1]$$

$$f' = 1.2 f \cdot 1.22 \cdot 0.56 \quad [8.2]$$

Combining equations [8.2] and [8.1] results in the solutions $f \approx 1.7 \cdot 10^{-14}$ m^2 and $f' \approx 1.4 \cdot 10^{-14}$ m^2.

8.3 Original Data

The complete original data of this work can be found on a CD, which is available on request at the Max Planck Institute for Metals Research, Department Arzt. The data organization will be following the here presented index.

9 References

1. Vincent, J. F. V. Biomechanics: Materials: A Practical Approach (eds. Rickwood, D. & Hames, B. D.) (Oxford University Press, New York, 1992).

2. Aizenberg, J. et al. Skeleton of *Euplectella* sp.: Structural hierarchy from the nanoscale to the macroscale. Science 309, 275-278 (2005).

3. Aristoteles. *De Historia Animalium* (350 B.C.). trans. 1918 by D'Arcy Wentworth Thompson (http://classics.mit.edu/Aristotle/history_anim.html).

4. Hiller, U. Untersuchungen zum Feinbau und zur Funktion der Haftborsten von Reptilien. Z. Morphol. Tiere 62, 307-362 (1968).

5. Ruibal, R. & Ernst, V. The structure of the digital setae of lizards. J. Morphol. 117, 271-279 (1965).

6. Autumn, K. & Peattie, A. M. Mechanisms of adhesion in geckos. Int. & Comp. Biol. 42, 1081-1090 (2002).

7. Irschick, D. J. et al. A comparative analysis of clinging ability among pad-bearing lizards. Biol. J. Linn. Soc. 59, 21-35 (1996).

8. Autumn, K. et al. Adhesive force of a single gecko foot-hair. Nature 405, 681-685 (2000).

9. Israelachvili, J. N. Intermolecular & Surface Forces (Academic Press Limited, London, 1992).

10. Gordon, J. E. Structures: Or, Why Things Don't Fall Down (Da Capo Press, New York, 1978).

11. Kendall, K. Molecular Adhesion and Its Applications: The Sticky Universe (Kluwer Academic/ Plenum Publishers, New York, 2001).

12. Greenwood, J. A. Constriction resistance and the real area of contact. Brit.J. Appl. Phys. 17, 1621-1632 (1966).

13. Fuller, K. N. G. & Tabor, D. The effect of surface roughness on the adhesion of elastic solids. Proc. Roy. Soc. London A 345, 327-342 (1975).

14. Persson, B. N. J. Adhesion between elastic bodies with randomly rough surfaces. Phys. Rev. Lett. 89, 245502/1-4 (2002).

15. Hansen, W. R. & Autumn, K. Evidence for self-cleaning in gecko setae. Proc. Natl Acad. Sci. USA 102, 385-389 (2005).

16. Autumn, K. et al. Evidence for van der Waals adhesion in gecko setae. Proc. Natl Acad. Sci. USA 99, 12252-12256 (2002).

17. Russel, A. P. A contribution to the functional morphology of the foot of the tokay, *Gekko gecko* (Reptilia, Gekkonidae). J. Zool. Lond. 176, 437-476 (1975).

18. Binnig, G. & Rohrer, H. Scanning tunnelling microscopy. Helvetica Phys. Acta 55, 726-735 (1982).

19. Binnig, G., Quate, C. F. & Gerber, C. Atomic force microscope. Phys. Rev. Lett. 56, 930-933 (1986).

20. Burnham, N. A., Domíguez, D. D., Mowery, R. L. & Colton, R. J. Probing the surface forces of monolayer films with an atomic-force microscope. Phys. Rev. Lett. 64, 1931-1934 (1990).

21. Marti, O., Drake, B. & Hansma, P. K. Atomic force microscopy of liquid-covered surfaces: atomic resolution images. Appl. Phys. Lett. 51, 484-486 (1987).

22. Drake, B. et al. Imaging crystals, polymers and processes in water with the atomic force microscope. Science 243, 1586-1589 (1989).

23. Meyer, G. & Amer, N. M. Novel optical approach to atomic force microscopy. Appl. Phys. Lett. 53, 1045-1047 (1988).

24. Barrena, E. et al. Self-organization of phthalocyanines on Al_2O_3 $(11\underline{2}0)$ in aligned and ordered films. J. Mater. Res. 19, 2061-2067 (2004).

25. Kirk, M. D., Albrecht, T. R. & Quate, C. F. Low-temperature atomic force microscopy. Rev. Sci. Instrum. 59, 833-835 (1988).

26. Basire, C. & Ivanov, D. A. Evolution of the lamellar structure during crystallization of a semicrystallineamorphous polymer blend: Time-resolved hotstage SPM study. Phys. Rev. Lett. 85, 5587-5590 (2000).

27. Burnham, N. A. & Colton, R. J. Measuring nanomechanical properties using an AFM. J. Vac. Sci. Technol. A 7, 2906-2913 (1989).

28. Butt, H.-J. et al. Imaging cells with the atomic force microscope. J. Struct. Biol. 105, 54-61 (1990).

29. Méndez-Vilas, A., Gallardo, A. M., Pérez-Giraldo, C., González-Martín, M. L. & Nuevo, M. J. Surface morphological characterization of yeast cells by scanning force microscopy. Surf. Interface Anal. 31, 1027-1030 (2001).

30. Weisenhorn, A. L., Khorsandi, M., Kasas, S., Gotzos, V. & Butt, H.-J. Deformation and height anomaly of soft surfaces studied with an AFM. Nanotechnology 4, 106-113 (1993).

31. Radmacher, M., Tillmann, R. W., Fritz, M. & Gaub, H. E. From molecules to cells: imaging soft samples with the atomic force microscope. Science 257, 1900-1905 (1992).

32. Langer, M. G. et al. A scanning force microscope for simultaneous force and patch-clamp measurements on living cell tissues. Rev. Sci. Instr. 68, 2583-2590 (1997).

33. Kesel, A. B., Martin, A. & Seidl, T. Getting a grip on spider attachment: an AFM approach to microstructure adhesion in arthropods. Smart Mater. Struct. 13, 512-518 (2004).

34. Langer, M. G. et al. Mechanical stimulation of individual stereocilia of living cochlear hair cells by atomic force microscopy. Ultramicroscopy 82, 269-278 (2000).

35. Hansma, H. G. & Hoh, J. H. Biomolecular imaging with the atomic force microscope. Annu. Rev. Biophys. Biomol. Struct. 23, 115-139 (1994).

36. Ludwig, M. et al. AFM, a tool for single-molecule experiments. Appl. Phys. A 68, 173-176 (1999).

37. Butt, H.-J. et al. Scan speed limit in atomic force microscopy. J. Microscopy 169, 75-84 (1993).

38. Cappella, B. & Dietler, G. Force-distance curves by atomic force microscopy Surf. Sci. Rep. 34, 1-104 (1999).

39. Burnham, N. A., Colton, R. J. & Pollock, H. M. Interpretation of force curves in force microscopy. Nanotechnology 4, 64-80 (1993).

40. Martin, Y., Williams, C. C. & Wickramasinghe, H. K. Atomic force microscope–force mapping and profiling on a sub 100-Å scale. J. Appl. Phys. 61, 4723-4729 (1987).

41. Giessibl, F. J. Atomic resolution of the silicon (111)-(7×7) surface by atomic force microscopy. Science 267, 68-71 (1995).

42. Zhong, Q., Inniss, D., Kjoller, K. & Elings, V. B. Fractured polymer/silica fiber surface studied by tapping mode atomic force microscopy Surf. Sci. Lett. 290, L688-L692 (1993).

43. Giessibl, F. J., Herz, M. & Mannhart, J. Friction traced to the single atom. Proc. Natl Acad. Sci. USA 99, 12006-12010 (2002).

44. García, R. & Pérez, R. Dynamic atomic force microscopy methods. Surf. Sci. Rep. 47, 197-301 (2002).

45. Spizig, P. M. Dynamische Rasterkraftmikroskopie (Ph.D. Thesis, Universität Ulm, 2002).

46. Radmacher, M., Cleveland, J. P., Fritz, M., Hansma, H. G. & Hansma, P. K. Mapping interaction forces with the atomic force microscope. Biophys. J. 66, 2159-2165 (1994).

47. Burnham, N. A. & Colton, R. J. in Scanning tunneling microscopy and spectroscopy (ed. Bonnell, D. A.) 191-250 (VCH, New York, 1993).

48. Hartmann, U. Van der Waals interactions between sharp probes and flat sample surfaces. Phys. Rev. B 43, 2404-2407 (1991).

49. Hamaker, H. C. The London-van der Waals attraction between spherical particles. Physica 4, 1058-1072 (1937).

50. Derjaguin, B. V., Muller, V. M. & Toporov Yu, P. Effect of contact deformations on the adhesion of particles. J. Colloid Interface Sci. 53, 314-326 (1975).

51. Tian, X. & Bhushan, B. The micro-meniscus effect of a thin liquid film on the static friction of rough surface contact. J. Phys. D 29, 163-178 (1996).

52. Chen, Y. L. E., Gee, M. L., Helm, C. A., Israelachvili, J. N. & McGuiggan, P. M. Effects of humidity on the structure and adhesion of amphiphilic monolayers on mica. J. Phys. Chem. 93, 1051-1059 (1989).

53. Chen, Y. L. E., Helm, C. A. & Israelachvili, J. N. Molecular mechanisms associated with adhesion and contact angle hysteresis of monolayer surfaces. J. Phys. Chem. 95, 10736-10747 (1991).

54. Leckband, D. et al. Measurements of conformational changes during adhesion of lipid and protein (polylysine and S-layer) surfaces. Biotechnol. Bioeng. 42, 167-177 (1993).

55. Stifter, T., Weilandt, E., Hild, S. & Marti, O. Influence of the topography on adhesion measured by SFM. Appl. Phys. A 66, S597-S605 (1998).

56. Luan, B. & Robbins, M. O. The breakdown of continuum models for mechanical contacts. Nature 435, 929-932 (2005).

57. Maugis, D. The JKR-DMT transition using a dugdale model. J. Colloid Interface Sci. 150, 243-269 (1992).

58. Maugis, D. Contact, adhesion and rupture of elastic solids (Springer, Heidelberg, 1999).

59. Hertz, H. Über die Berührung fester elastischer Körper. J. für die reine und angewandte Math. 92, 156-171 (1882).

60. Johnson, K. L., Kendall, K. & Roberts, A. D. Surface energy and the contact of elastic solids. Proc. R. Soc. London A 324, 301-313 (1971).

61. Carpick, R. W., Ogletree, D. F. & Salmeron, M. A general equation for fitting contact area and friction vs load measurements. J. Coll. Interf. Sci. 211, 395-400 (1999).

62. Enachescu, M. et al. Atomic force microscopy study of an ideally hard contact: the diamond(111)/tungsten carbide interface. Phys. Rev. Lett. 81, 1877-1880 (1998).

63. Rosenberg, H. I., Russell, A. P. & Cavey, M. J. Development of the subdigital adhesive pads of *Ptyodactylus guttatus* (Reptilia: Gekkonidae). J. Morphol. 211, 243-258 (1992).

64. Stork, N. E. A comparison of the adhesive setae on the feet of lizards and anthropods. J. Nat. Hist. 17, 829-835 (1983).

65. Homann, H. Haften Spinnen an einer Wasserhaut? Die Naturwissenschaften 44, 318-319 (1957).

66. Bauchhenss, E. The pulvilli of *Calliphora erythrocephala* (Diptera: Brachycera) as adhesive organs. Zoomorphologie 93, 99-124 (1979).

67. Gorb, S. N. The design of the fly adhesive pad: distal tenent setae are adapted to the delivery of an adhesive secretion. Proc. R. Soc. London B 265, 747-752 (1998).

68. Gorb, S., Gorb, E. & Kastner, V. Scale effects on the attachment pads and friction forces in syrphid flies. J. Exp. Biol. 204, 1421-1431 (2001).

69. Langer, M. G., Ruppersberg, J. P. & Gorb, S. N. Adhesion forces measured at the level of a terminal plate of the fly's seta. Proc. R. Soc. London B 271, 2209-2215 (2004).

70. Arzt, E., Gorb, S. & Spolenak, R. From micro to nano contacts in biological attachment devices. Proc. Natl Acad. Sci. USA 100, 10603-10606 (2003).

71. Sun, W., Neuzil, P., Kustandi, T. S., Oh, S. & Samper, V. D. The nature of the gecko lizard adhesive force. Biophys. J. 89, L14-17 (2005).

72. Scherge, M. & Gorb, S. N. Biological Micro- and Nanotribology: Nature's Solutions (Springer-Verlag, New York, 2001).

73. Gorb, S. N., Jiao, Y. & Scherge, M. Ultrastructural architecture and mechanical properties of attachment pads in *Tettigonia viridissima* (Orthoptera Tettigoniidae). J. Comp. Physiol. A 186, 821-831 (2000).

74. Gao, H., Wang, X., Yao, H., Gorb, S. N. & Arzt, E. Mechanics of hierarchical adhesion structures of geckos. Mech. Mater. 37, 275-285 (2005).

75. Owens, D. K. & Wendt, R. C. Estimation of the surface free energy of polymers. J. Appl. Polym. Sci. 13, 1741-1747 (1969).

76. Hutter, J. L. & Bechhoefer, J. Calibration of atomic-force microscope tips. Rev. Sci. Instrum. 64, 1868-1873 (1993).

77. Huntington, S. & Nespolo, S. Precision attachment of (Silica) spheres to AFM cantilever tips. Microsc. Today 9, 32-33 (2001).

78. Jena, B. P. & Hörber, J. K. H. Atomic force microscopy in cell biology (Methods in cell biology) 94-95 (Academic Press London, 2002).

79. Pfaff, H. Adhesion of bioinspired contact elements (Ph.D. Thesis, Universität Stuttgart, 2005).

80. Reyntjens, S. & Puers, R. A review of focused ion beam applications in microsystem technology. J. Micromech. Microeng., 287-300 (2001).

81. Walters, D. A. et al. Short cantilevers for atomic force microscopy. Rev. Sci. Instrum. 67, 3583-3590 (1996).

82. Sader, J. E., Larson, I., Mulvaney, P. & White, L. R. Method for the calibration of atomic force microscope cantilevers. Rev. Sci. Instrum. 66, 3789-3798 (1995).

83. Sader, J. E. Parallel beam approximation for V-shaped atomic force microscope cantilevers. Rev. Sci. Instrum. 66, 4583-4587 (1995).

84. Cleveland, J. P., Manne, S., Bocek, D. & Hansma, P. K. A nondestructive method for determining the spring constant of cantilevers for scanning force microscopy. Rev. Sci. Instrum. 64, 403-405 (1993).

85. Burnham, N. A. et al. Comparison of calibration methods for atomic-force microscopy cantilevers. Nanotechnology 14, 1-6 (2003).

86. Butt, H. J. & Jaschke, M. Calculation of thermal noise in atomic force microscopy. Nanotechnology 6, 1-7 (1995).

87. Kendall, K. Thin-film peeling-the elastic term. J. Phys. D 8, 1449-1452 (1975).

88. Arzt, E., Enders, S. & Gorb, S. Towards a micromechanical understanding of biological surface devices. Z. Metallkunde 93, 345-51 (2002).

89. Gao, H. & Yao, H. Shape insensitive optimal adhesion of nanoscale fibrillar structures. Proc. Natl Acad. Sci. USA 101, 7851-7856 (2004).

90. Spolenak, R., Gorb, S. N. & Arzt, E. Adhesion design maps for bio-inspired attachment systems. Acta Biomater. 1, 5-13 (2005).

91. Geim, A. K. et al. Microfabricated adhesive mimicking gecko foot-hair. Nature Mater. 2, 461-463 (2003).

92. Peressadko, A. & Gorb, S. N. When less is more: experimental evidence for tenacity enhencement by division of contact area. J. Adhes. 80, 1-15 (2004).

93. Glassmaker, N. J., Jagota, A. & Hui, C.-Y. Adhesion enhancement in a biomimetic fibrillar interface. Acta Biomater. 1, 367-375 (2005).

94. Jin, M. et al. Superhydrophobic aligned polystyrene nanotube films with high adhesive force. Adv. Mater. 17, 1977-1981 (2005).

95. Huber, G. et al. Evidence for capillarity contributions to gecko adhesion from single spatula nanomechanical measurements. Proc. Natl Acad. Sci. USA 102, 16293-16296 (2005).

96. Huber, G., Gorb, S. N., Spolenak, R. & Arzt, E. Resolving the nanoscale adhesion of individual gecko spatulae by atomic force microscopy. Biol. Lett. 1, 2-4 (2005).

97. Stork, N. E. Experimental analysis of adhesion of *Chrysolina polita* (Chrysomelidae: Coleoptera) on a variety of surfaces. J. Exp. Biol. 88, 91-107 (1980).

98. Bhushan, B. & Sundararajan, S. Micro/nanoscale friction and wear mechanisms of thin films using atomic force and friction force microscopy. Acta Mater. 46, 3793-3804 (1998).

99. Freund, J., Halbritter, J. & Hörber, J. K. H. How dry are dried samples? Water adsorption measured by STM. Microsc. Res. Tech. 44, 327-338 (1999).

100. Beaglehole, D. & Christenson, H. K. Vapor adsorption on mica and silicon: entropy effects, layering, and surface forces. J. Phys. Chem. 96, 3395-3403 (1992).

101. Sugawara, Y. et al. Effects of humidity and tip radius on the adhesive force measured with atomic force microscopy. Wear 168, 13-16 (1993).

102. Thundat, T. et al. Characterization of atomic force microscope tips by adhesion force measurements. Appl. Phys. Lett. 63, 2150-2152 (1993).

103. Orr, F. M., Scriven, L. E. & Rivas, A. P. Pendular rings between solids: meniscus properties and capillary force. J. Fluid Mech. 67, 723-742 (1975).

104. Stifter, T., Marti, O. & Bhushan, B. Theoretical investigation of the distance dependence of capillary and van der Waals forces in scanning force microscopy. Phys. Rev. B 62, 13667-13673 (2000).

105. Bhushan, B. Handbook of Micro/Nanotribology. CRC Press LLC, 259-261 (1999).

106. Measured by H. Mantz (Universität des Saarlandes, Saarbrücken). (2004).

107. Seemann, R., Herminghaus, S. & Jacobs, K. Dewetting patterns and molecular forces: a reconciliation. Phys. Rev. Lett. 86, 5534-5537 (2001).

108. Seemann, R., Herminghaus, S. & Jacobs, K. Gaining control of pattern formation of dewetting liquid films. J. Phys. Cond. Matter. 13, 4925-4938 (2001).

109. Jang, J., Schatz, G. C. & Ratner, M. A. Capillary force in atomic force microscopy. J. Chem. Phys. 120, 1157-1160 (2004).

110. Xiao, X. & Qian, L. Investigation of humidity-dependent capillary force. Langmuir 16, 8153-8158 (2000).

111. He, M. et al. Critical phenomena of water bridges in nanoasperity contacts. J. Chem. Phys. 114, 1355-1360 (2001).

112. Gennes, P.-G. d., Brochard-Wyart, F. & Quéré, D. Capillarity and Wetting Phenomena : Drops, Bubbles, Pearls, Waves, 8-9 (Springer, New-York, 2003).

113. Kusalik, P. G. & Svishchev, I. M. The spatial structure in liquid water. Science 265, 1219-1221 (1994).

114. Quéré, D. Surface wetting: model droplets. Nature Mater. 3, 79-80 (2004).

115. Checco, A., Guenoun, P. & Daillant, J. Nonlinear dependence of the contact angle of nanodroplets on contact line curvature. Phys. Rev. Lett. 91, 186101/1-4 (2003).

116. Magueijo, J. Faster than the speed of light: The story of a scientific speculation Perseus Books Group Cambridge, MA., USA, 202-204 (2003).

117. Mecke, K. Personal Communications. (2005).

118. Langmuir, I. Constitution and fundamental properties of solids and liquids. J. Am. Chem. Soc. 38, 2221-2295 (1916).

119. Dai, Z., Gorb, S. N. & Schwarz, U. Roughness-dependent friction force of the tarsal claw system in the beetle *Pachnoda marginata* (Coleoptera, Scarabaeidae). J. Exp. Biol. 205, 2479-2488 (2002).

120. Peressadko, A. G. & Gorb, S. N. in Bionik 2004 (eds. Boblan, I. & Bannasch, R.) 237-242 (Hannover, 2004).

121. Tabor, D. Surface forces and surface interactions. J. Colloid Interface Sci. 58, 2-13 (1977).

122. Persson, B. N. J. & Tosatti, E. The effect of surface roughness on the adhesion of elastic solids. Journal of Chemical Physics 115, 5597-5610 (2001).

123. Persson, B. N. J. & Gorb, S. The effect of surface roughness on the adhesion of elastic plates with application to biological systems. J. Chem. Phys. 119, 11437-11444 (2003).

124. Peressadko, A. G., Hosoda, N. & Persson, B. N. J. Influence of surface roughness on adhesion between elastic bodies. Phys. Rev. Lett. 95, 124301/1-4 (2005).

125. Santos, R., Gorb, S. N., Jamar, V. & Flammang, P. Adhesion of echinoderm tube feet to rough surfaces. J. Exp. Biol. 208, 2555-2567 (2005).

126. Gorb, S. N. Unpublished results and personal communication. (2005).

127. Oliver, W. C. & Pharr, G. M. An improved technique for determining hardness and elastic modulus using load and displacement sensing indentation experiments. J. Mater. Res. 7, 1564-1583 (1992).

128. Wu, B., Heidelberg, A. & Boland, J. J. Mechanical properties of ultrahigh-strength gold nanowires. Nature Mater. 4, 525–529 (2005).

129. Namazu, T. & Isono, Y. Quasi-static bending test of nano-scale SiO_2 wire at intermediate temperatures using AFM-based technique. Sens. Actuators A 104, 78-85 (2003).

130. Liu, H. & Bhushan, B. Bending and fatigue study on a nanoscale hinge by an atomic force microscope. Nanotechnology 15, 1246-1251 (2004).

131. Cuenot, S., Demoustier-Champagne, S. & Nysten, B. Elastic modulus of polypyrrole nanotubes. Phys. Rev. Lett. 85, 1690-1693 (2000).

132. Orso, S. Structure and mechanical investigations of biological materials using a focussed ion beam microscope (Ph.D. Thesis, Universität Stuttgart, 2005).

133. Orso, S., Wegst, U. G. K., Eberl, C. & Arzt, E. Micrometer scale tensile testing of biological attachment devices. Adv. Mater. submitted (2005).

134. Gibson, C. T., Watson, G. S. & Myhra, S. Determination of the spring constants of probes for force microscopy/spectroscopy. Nanotechnology 7, 259-262 (1996).

135. Varenberg, M., Etsion, I. & Halperin, G. Nanoscale fretting wear study by scanning probe microscopy. Tribol. Lett. 18, 493-498 (2005).

136. Spurr, A. R. A low-viscosity epoxy resin embedding medium for electron microscopy. J. Ultrastructure Res. 26, 31-43 (1969).

137. Barbakadze, N. Micro/nanomechanical measurements on insect and plant cuticles (Ph.D. Thesis, Universität Stuttgart, 2005).

138. Wegst, U. G. K. Natural Materials Selector, created using the CES Constructor Software. Granta Design Ltd. Rustat House, 62 Clifton Road, Cambridge CB1 7EG, U.K. (2004).

139. Vincent, J. F. V. Structural Biomaterials (Princeton University Press, 1990).

140. Bonser, R. & Purslow, P. The Young's modulus of feather keratin. J. Exp. Biol. 198, 1029-1033 (1995).

141. Bonser, R. H. C., Saker, L. & Jeronimidis, G. Toughness anisotropy in feather keratin. J. Mater. Sci. 39, 2895-2896 (2004).

142. Goldsmith, L. A. & Baden, H. P. The Mechanical Properties of Hair. I. The Dynamic Sonic Modulus. J. Invest. Derm. 55, 256-259 (1970).

10 Deutsche Kurzfassung der Dissertation

10.1 Motivation und Literaturüberblick

Kostenintensive Verbindungstechniken wie Kleben oder Schweißen haben den Nachteil, dass sich einmal auf diese Weise verbundene Bauteile bei Reparaturen oder einem späteren Recycling nicht mehr ohne Materialverlust voneinander lösen lassen. Die in dieser Hinsicht vorteilhaften Klettverschlüsse benötigen jedoch einen Haftpartner und verfilzen mit der Zeit. Schon Aristoteles war im 4. Jahrhundert v. Chr.[3] fasziniert von den Kletterkünsten der Geckos (Abb. 1.1) und auch heute noch lohnt es sich, natürliche Lösungen anzuschauen, um die Mechanismen zu ergründen, welche die Evolution verschiedenen Insekten anhand (bzw. Fuß) gegeben hat[70]. Neben glatten, gut adaptiven Kontaktelementen findet man in der Natur häufig auch das Konzept hierarchischer, haariger Strukturen[72, 73] (Abb. 3.1). Der typische Geckofuß-Aufbau besteht aus Lamellen (400-600 µm lang), Setae (~6 µm breit – das entspricht ungefähr einem zehntel des Durchmessers eines menschlichen Haares - und ~100 µm lang) und Spatulae (~200 nm breit und lang, Abb. 3.2). Letztere winzige Härchen sind es, die es dem Gecko erlauben, sowohl auf atomar glatten als auch auf natürlichen, unebenen Oberflächen erstaunlich gut zu haften. Die hierarchische Struktur ermöglicht es dem Tier, eine genügend große Anzahl Spatulae in so engen Kontakt mit dem Untergrund zu bringen, dass attraktive intermolekulare Kräfte wirken. Gleichzeitig sind diese Haare zusätzlich extrem hydrophob (Kapitel 4) und sogar selbstreinigend[15], so dass sie ihr

Haftvermögen - selbst nach einer hohen Anzahl von Bewegungsabläufen des Tieres - nicht verlieren.

Obwohl die Grundlagen der Adhäsion verschiedener Tiere[33, 66-68, 73] - insbesondere auch von Geckos [4-8, 16, 17] - bereits seit langer Zeit Gegenstand intensiver Forschung waren (Kapitel 2.5), konnte erst mit Hilfe der in dieser Arbeit präsentierten Präparations- und Charakterisierungsmethoden die niedrigste Stufe der Hierarchie - die der Kontakt bildenden Spatulae – experimentell untersucht werden. Darüber hinaus wurden erstmals die mechanischen Eigenschaften einzelner Geckosetae quantifiziert. Die Experimente wurden in erster Linie mit Hilfe eines Rasterkraftmikroskops (eng. AFM) durchgeführt. Das AFM wurde 1986 von Binnig und Rohrer vorgestellt[19] und ermöglichte bis heute eine große Vielzahl und Vielfalt an Abbildungen und Experimenten, welche mit anderen Charakterisierungsmethoden wesentlich schwieriger oder gar unmöglich gewesen wären[28-36]. So lassen sich AFM Messungen auch an nicht leitenden Proben unter verschiedenen Gasatmosphären[20], in Flüssigkeiten[21, 22] und Ultrahochvakuum[23, 24], aber auch bei sehr niedrigen[25] oder hohen[26] Temperaturen durchführen. Das Lichtzeigerdetektionsprinzip (Abb. 2.1 und 2.2) des AFM beruht darauf, eine extrem scharfe Spitze am freien Ende eines freitragenden Balkens (Cantilevers) in die Nähe der Probenoberfläche zu bringen, um diese dann mit Hilfe eines piezoelektrischen Stellglieds abzurastern und die dabei auftretenden lateralen und vertikalen Verbiegungen mit Hilfe eines Laserstrahls zu registrieren. Dieser wird auf die reflektierende Rückseite eines Cantilevers positioniert und von dort auf einen positionsempfindlichen Photodetektor reflektiert. Hiermit kann die am Cantilever der Federkonstante c lokal gemessene Kraft (typischerweise im piko- oder nano-Newton Bereich) zwischen AFM-Spitze und der untersuchten Oberfläche (Kapitel 2.3) zur Abbildung der Topographie oder zur Bestimmung adhäsiver bzw. mechanischer Eigenschaften detektiert werden. Die limitierte Scangeschwindigkeit aller Abbildungsmodi (hauptsächlich konstanter Kraftmodus bzw. konstanter Kraftgradient: Kapitel 2.2) ist jedoch ein deutlicher Nachteil[37] im Vergleich zu anderen Mikroskopieverfahren. So braucht man ca. 5 Minuten, um mit Hilfe des AFMs eine quadratische Fläche abzurastern und viele nanoskalige Anwendungen (z. B. *in situ* Experimente) würden erheblich von schnelleren Abbildungsmöglichkeiten profitieren.

Während für die Klärung der Frage, welche Haftkräfte wirken, eine Analyse der intermolekularen Kräfte notwendig ist, erleichtern die Konzepte der Kontaktmechanik[50, 57, 59, 60] (Kapitel 2.4) oftmals die Überprüfung experimenteller Daten. Hier werden sowohl die AFM-Spitze als auch die Probenoberfläche wieder als makroskopische Körper betrachtet, deren physikalische Eigenschaften durch leicht messbare Größen wie E-Modul oder Oberflächenenergie beschrieben werden.

10.2 Experimentelles

Zur Messung der Adhäsionskraft einer Spatula wurden einzelne Geckosetae zunächst vom Fuß eines *Gekko geckos* mit Hilfe einer Nadelspitze abgelöst (Kapitel 3.2). Unter dem Binokularmikroskop wurde das so separierte Haar mittels eines Klebstofftropfens an der Cantileverspitze fixiert und senkrecht ausgerichtet. Der Tropfen besaß in etwa die Größe der für den Transfer verwendeten Spitze einer menschlichen Wimper (Abb. 3.3). Nach exakter Positionierung wurde der Klebstoff durch Bestrahlung mit ultraviolettem Licht (ca. 10 min bei einer Wellenlänge von 366 nm) ausgehärtet. Hiernach wurde die so vorbereitete Probe mit Hilfe des fokussierten Ionenstrahlmikroskops[80] (eng. FIB) weiterbearbeitet. Bei bestmöglicher Vermeidung von Probenschädigungen mittels eines niedrigen Strahlstroms von lediglich 11 pA wurde ausgehend von der Anklebung entlang der Seta an jeder Haarverzweigung ein Ast abgeschnitten und so sukzessive die Spatulae Anzahl von ursprünglich mehreren hundert auf weniger als fünf reduziert. Zusätzlich konnte in der Einzelbildabfolge gleichzeitig verifiziert werden, dass das Haar außer an seiner Wurzel nirgendwo durch Klebstoff bedeckt und verändert wurde. Schließlich wurde die so gewonnene Probe in das AFM transferiert, um die Adhäsionskraftmessungen auf den jeweiligen Substraten durchzuführen. Die in dieser Arbeit verwendeten Oberflächen wurden zunächst in einer „Piranha“-Lösung (Schwefelsäure und Wasserstoffperoxid im Verhältnis 1:1) generalgereinigt, um sie anschließend 30 Minuten in heißem Millipore™ Wasser auszukochen. Die finale Reinigungsprozedur mit Hilfe von Ultraschallwellen war eine Abfolge von verschiedenen Lösungsmittelbädern. Die Substrate wurden durch Toluol, Aceton und Ethanol unter jeweiligem Trockenblasen im reinen Stickstoffstrom gesäubert. Jede der auf diese Weise behandelten Proben wurde über die Methode des ruhenden Tropfens[75] und mittels AFM-Abbildungen im Hinblick auf Oberflächenenergie und Rauhigkeit charakterisiert. Oberflächen mit verschiedenem Hydrophilitätsgrad bei vergleichbaren Rauhigkeiten konnten erfolgreich hergestellt werden, indem zum einen Wafer unterschiedlicher Oxidschichtdicke (~2 nm und ~190 nm: Kapitel 4.2.1) wie eben beschrieben gereinigt und dadurch sehr hydrophil wurden. Zum anderen zeigten diese Si-Wafer nach Monolagenbedeckung mit Octadecyltrichlorsilan (OTS) deutlich hydrophobe Eigenschaften (Wasserkontaktwinkel > 100°).

Die in Kapitel 5 benutzen Substrate variabler Rauhigkeit bei sonst gleicher Oberflächenchemie stammten aus einer Arbeit von Peressadko und Hosoda[124]. Die zum Einsatz gebrachten Cantilever wurden entweder mit Hilfe der Methode des thermischen Rauschens[76, 86] oder mittels ihrer exakt ausgemessenen Geometriedaten[134] kalibriert. Die Arbeit von Autumn[8] *et al.* zeigte, dass eine gewisse Vorkraft (hier 90 nN) gefolgt von einer lateralen Scherbewegung (7 µm) notwendig war, um reproduzierbare Adhäsionskräfte messen zu können. Dies liegt darin begründet, dass der natürliche Bewegungsablauf des Tieres bestmöglich auch in unserem Experiment nachgeahmt werden musste (Abb. 3.5). Auf diese Weise konnten Versuche auf Substraten unterschiedlicher Oberflächenchemie bzw. variabler Rauhigkeiten (Kapitel 5) durchgeführt werden. Bei allen Experimenten wurden darüber hinaus jeweils lokal, nahe der untersuchten Oberfläche, instantan Temperatur und Luftfeuchtigkeit gemessen. Indem das komplette AFM in einen gasdichten Container gebracht wurde, konnte durch Steuerung der zugeführten Stickstoffmenge die Luftfeuchtigkeit im Inneren kontrolliert werden.

Letzteres galt auch für die Steifigkeitsuntersuchungen des 3 Punkt-Biegeversuchs. Hier wurde eine über einem Graben liegende, fixierte Seta zyklisch gebogen, während die Humidität im Inneren des Containers kontrolliert variiert wurde. Die Krafteinleitung erfolgte dabei exakt in der Mitte der freien Haarlänge mittels der AFM-Spitze eines extrem steifen Cantilevers. Durch Wolframabscheidung im FIB wurde die Fixierung der Seta jeweils an den Rändern des zuvor durch Ga-Ionen ausgefrästen Grabens realisiert. Da die Cantileversteifigkeit bekannt war, konnte aus der gemessenen Gesamtsteifigkeit des Systems die Setasteifigkeit errechnet werden. Dazu musste der Cantilever zunächst gegen eine harte Oberfläche (in diesem Fall gegen den oxidierten Si-Wafer) gepresst werden, um die rein mechanische Antwort des Balkens zu erhalten. Erst danach konnte auf die einzelne Seta gedrückt und somit deren Biegesteifigkeit unter Berücksichtigung der geometrischen Gegebenheiten erhalten werden.

Zusätzlich wurde der E-Modul einzelner Gecko Setae durch *in situ* Zugversuche[133] mittels eines in ein FIB eingebauten Mikromanipulators bestimmt. Auch klassische Nanoindentierungsversuche[127] trugen zusätzlich zur Klärung der Frage der Kompositsteifigkeit bei (Kapitel 6).

10.3 Ergebnisse und Diskussion

In der vorliegenden Arbeit wurde erstmals die Adhäsionskraft einer einzelnen Gecko Spatula mit ~10 nN auf einem Objektträger aus Kalknatronglas bei Umgebungsbedingungen determiniert (Kapitel 3.3). Hierbei konnte in den jeweiligen Kraft-Abstandskurven zwischen verschiedenen Ablösemodi differenziert werden (Abb. 3.6). In ca. 39 % der Fälle wurde das Ablösen einer einzelnen Spatula beobachtet. Mit ~54 % wurde am häufigsten eine Ablösekraft von 20 nN gemessen was einem gleichzeitigen Haftverlust der Haare entspricht. Wesentlich seltener (5 % der Fälle) wurde durch die Scherbewegung vermutlich eine elastische Vorspannung auf eines der Haare gebracht, was zu einem seriellen, z. T. verfrühten Ablösen der Spatulae führte. In den restlichen Fällen hafteten wahrscheinlich drei Spatulae gleichzeitig, was die beobachteten Kraftwerte von ~30 nN erklären würde. Da eine Adhäsionskraft von 40 nN nicht gemessen wurde, ist anzunehmen, dass niemals alle vier Spatulae gleichzeitig in Kontakt waren. Auch der Gecko nutzt für seine Haftung vermutlich immer nur einen Bruchteil der ihm zur Verfügung stehenden ca. 1 Milliarde Spatulae. Diese Anzahl multipliziert mit dem gemessenen Wert von 10 nN ergibt ein hypothetisches Gewicht von 1 kg als obere Grenze dessen, was ein typischerweise 100 g schwerer Gecko tragen könnte. Der experimentell gewonnene Kraftwert kann mit Hilfe kontaktmechanischer Theorien[60, 87] überprüft werden. Die dabei gefundenen Werte von ~20 bzw. 50 mJ/m^2 sind exakt in dem Adhäsionsarbeitsintervall von 10 bis

100 mJ/m^2, welches man im Normalfall für intermolekulare Kraftwechselwirkungen erwartet. Sobald der gleiche experimentelle Ablauf unter Millipore™ Wasser wiederholt wurde, reduzierte sich die Adhäsionskraft einer einzelnen Spatula deutlich auf einen Wert von ~2,5 nN. Dies war einer der Gründe, weshalb die Qualität und Quantität der für die Geckohaftung verantwortlichen Adhäsionskräfte näher untersucht werden musste, da bis dato lediglich reine van der Waals Wechselwirkungen zwischen trockenen Oberflächen verantwortlich gemacht wurden[16]. Daher wurden Versuche auf speziell präparierten Waferoberflächen durchgeführt, bei denen man -im Gegensatz zu früheren Untersuchungen[16]- zwischen dem Einfluss kurzreichweitiger Kräfte und dem langreichweitiger Wechselwirkungen differenzieren konnte (Kapitel 4.2.1). Die Ergebnisse zeigten, dass sich die Adhäsionskräfte zwar sensitiv für das Ab- oder Vorhandensein der Silanschichten zeigten, jedoch spielte der eher langreichweitige Einfluss der Oxidschichtdicke keine Rolle. Mit anderen Worten: je hydrophiler das Substrat, desto größer die Adhäsionskräfte (Abb. 4.1). Die Messungen auf den silanisierten, hydrophoben Wafern ergaben Werte von ~7 nN während auf den hydrophilen Oxidschichten mindestens doppelt so große Kräfte gemessen wurden. Bei den Haftungsversuchen auf dem hydrophilen Wafer unter Wasser wurden wie zuvor auf dem Deckglas –also unabhängig vom Hydrophilitätsgrad- wesentlich niedrigere Adhäsionskräfte von knapp 3 nN gemessen. Dieser Effekt konnte qualitativ durch das Verschwinden von Kapillareffekten bzw. die Reduktion der Hamaker Konstanten einerseits und dem Vorhandensein sich gegenseitig abstoßender Ladungsschichten andererseits erklärt werden.

Darüber hinaus deuteten davon unabhängige Messungen auf dem bereits früher verwendeten Deckglas bei variierender Luftfeuchtigkeit (Abb. 4.2) auf einen nicht zu vernachlässigenden Kapillarkraftanteil hin. So stiegen auf dem Kalknatronglas die Adhäsionskräfte mehr oder weniger linear von ~7 nN in trockener Stickstoffatmosphäre auf Werte von ~12 nN bei 60 % Luftfeuchtigkeit an. Gleichzeitig zeigten ellipsometrische Messungen[106], dass die bereits vorhandene Wasserbedeckung auf einem hydrophilen Wafer (N-phil - Kapitel 4.3) bei identischem Humiditätsanstieg fast um eine weitere Monolage H_2O anwuchsen. Fasst man beide Ergebnisse zusammen, so wird klar, dass Monolagen von Wasser, wie sie zwischen einer Geckospatula und jedwedem Substrat vorhanden sein können, einen nicht vernachlässigbaren Einfluss auf die Adhäsionskräfte haben. Für diese Schlussfolgerung waren beide Experimente notwendig, da die geänderte Oberflächenchemie für sich allein genommen nicht zwischen dem Humiditätseinfluss und den van der Waals Effekten unterscheiden ließ. Die experimentell gewonnenen Daten konnten mit Hilfe zweier unterschiedlicher theoretischer Konzepte erklärt werden. Beiden Erklärungen lag eine ähnliche Annahme zugrunde: die Wassermenge zwischen Spatula und Substrat war zum einen direkt abhängig von der Luftfeuchtigkeit und zum anderen vom Hydrophilitätsgrad des Substrates. Die erste Theorie verknüpfte das Bild eines bereits existierenden Nanokapillaritätsmodells[51, 98, 111] mit einer Kontinuums-Kapillaritätsformel[112] (Kapitel 4.5.1). Dieses Vorgehen wurde durch die Tatsache motiviert, dass Kontinuumsmodelle erstaunlich weit bis in fast atomare Skalenbereiche gelten (z. B. Mischkristallhärtung). Darüber hinaus zeigte eine kürzlich veröffentlichte Arbeit[114], dass selbst auf extrem hydrophoben Oberflächen sehr kleine, bevorzugte Kondensationskeime vorhanden sind und vielmehr noch, manche zuvor hydrophobe Oberflächen unter dem Einfluss von Luftfeuchtigkeit sogar von hydrophoben zu hydrophilen Eigenschaften wechseln können[52-54], um so lokal die Adsorption winzigster Wassertröpfchen zu begünstigen. Zusammengenommen würden diese Phänomene die Existenz von Nanobrücken untermauern. Das zweite Konzept erklärte im Gegensatz dazu die experimentell gewonnenen Daten rein auf molekularer Ebene mittels Veränderungen der kurzreichweitigen Wechselwirkungen aufgrund von adsorbierten Wassermonolagen (Kapitel 4.5.2). Hier wurde angenommen, dass ein Flächenanteil der Spatula „trocken“ über klassische van der Waals Anziehung haftete und ein anderer Flächenanteil, welcher von der Humidität innerhalb des Containers und dem Hydrophilitätsgrad des Substrats abhing, zusätzlich zur Adhäsion beitrug (Abb. 4.5). Beide Modelle versagen allerdings für den Übergang zu 100 % Luftfeuchtigkeit. Hierfür konnte lediglich die oben beschriebene qualitative Erklärung gegeben werden. Andererseits stimmt der auf submikroskopischer Skala gemessene Effekt mit makroskopischen Beobachtungen am lebenden Tier überein. So besprühen Zoologen Geckos vollständig mit Wasser, wenn sie das Tier leicht von einer Oberfläche lösen möchten.

Der Einfluss der Substratrauhigkeit auf die Geckoadhäsion konnte sowohl auf submikroskopischer Skala (Abb. 5.2) als auch am lebenden Tier[126] übereinstimmend festgestellt werden. Die Adhäsionskraft als Funktion der Rauhigkeit von Substraten (Abb. 5.1), welche alle aus demselben Epoxyd Harz hergestellt wurden, zeigte ein distinktes Minimum (~9 nN). Die mit dem Minimum korrespondierenden Rauhigkeitswerte deckten sich in etwa mit der typischen lateralen Größe einer Geckospatula. Es zeigte sich, dass, obgleich Haar an seinem plattenförmigen Ende nur noch 11 nm dünn ist, die Oberflächentopographie dennoch eine große Rolle spielt und die flexible Spatula nicht auf allen Untergründen gleich gut haftet. Sowohl auf den glatteren als auch auf den rauheren Oberflächen hafteten die Spatulae mit bis zu 14 nN deutlich besser im Vergleich zum Minimalwert. Die lässt sich anhand simpler Überlegungen erklären. Den beiden extrem glatten Oberflächen konnte die 200 nm lange und breite Spatula so gut angenähert werden, dass ihre gesamte Kontaktfläche für intermolekulare Wechselwirkungen zur Verfügung stand. Aus der Sicht einer Spatula hingegen, erschien die extrem rauhe Oberfläche wiederum „glatt“ zu sein, boten ihr die - im Vergleich zu ihren Dimensionen - groben Unebenheiten doch genügend Platz, so dass erneut die gesamte Kontaktfläche für attraktive Wechselwirkungen zur Verfügung stand (Abb.5.3).

Die Ergebnisse der mechanischen Tests an einzelnen Setae waren, wie für einen biologischen Kompositwerkstoff zu erwarten, sowohl abhängig von dem Feuchtigkeitsgehalt der Proben, sowie auch von der Belastungsart und Richtung. Dies zeigten die Untersuchungen, welche sich dreier unterschiedlicher Messmethoden bedienten. Zum einen wurden die longitudinalen Steifigkeitseigenschaften durch *in situ* Zugversuche in der Vakuumkammer eines FIB bestimmt. Hierbei zeigte sich ein bei allen drei Proben vergleichbarer elastischer Verformungsbereich bis zu einer Dehnung von ca. 0,5 %. Im weiteren Verlauf war der Kurvenverlauf für die verschiedenen Proben allerdings nicht mehr kongruent, was *per se* allerdings für ausgetrocknete, biologische Materialien auch nicht zu erwarten war.

Zum anderen wurden einzelne Haare bei Raumtemperatur und Feuchtigkeit in Dreipunktbiegeversuchen und mittels Nanoindentierung transversal getestet. Hierbei lieferten die beiden völlig unterschiedlichen Messmethoden erstaunlich gut übereinstimmende E-Modul Werte von ~1,7 GPa (AFM) bzw. ~1,2 GPa (Nanoindentierung). Im Biegeversuch zeigte sich auch nahezu kein Einfluss der Luftfeuchtigkeit auf das Steifigkeitsverhalten. So waren die E-Modul Werte über ein Intervall von 2 % bis 60 % nahezu konstant. Dies könnte mehrere Gründe haben. Zum einen ist es bekannt, dass die Matrix hauptsächlich für die Wasseraufnahme verantwortlich ist, zum anderen ist außerdem bekannt, dass sobald diese Matrix einmal vollständig dehydriert war (wie im vorliegenden Fall durch die Probenpräparation in der Vakuumkammer des FIB) eine spätere Wasseraufnahme nur noch erschwert möglich bzw. gänzlich unmöglich erscheint[1]. Insgesamt decken sich die für eine Gecko Seta erstmals gemessenen Werte jedoch sehr gut mit vergleichbaren Daten anderer keratinhaltiger biologischer Materialien. Die Steifigkeitsmessungen stimmten gut mit den Werten überein, welche in den so genannten „Adhesion Design Maps“[90] für Gecko Setae vorhergesagt wurden. Darüberhinaus fanden Goldsmith und Baden einen E-Modul von ca. 10 GPa für menschliches Haar[142] und Vincent *et al.* legten den Steifigkeitsbereich für β-Keratin in Vogelfedern zu 1-10 GPa fest[140, 141]. Diese grobe Definition zeigt, dass die hier präsentierten Methoden trotz der für biologische Proben typischen Schwierigkeiten in der Lage waren, mit Hilfe ihrer größeren Messgenauigkeit präzisere Aussagen zu liefern.

In ihrer Gesamtheit liefert diese Arbeit zum einen wertvolle Beiträge zu aktuellen Adhäsionsfragestellungen im Allgemeinen und zum anderen wirft sie neues Licht auf die Geckoadhäsion im Speziellen. Dieses Wissen dient potentiell der erfolgreichen Entwicklung künstlicher Haftsysteme, welche iterativ eingesetzt werden könnten, ohne ihre Funktionalität einzubüßen.

List of Figures and Tables

List of Figures:

List of Tables: